Australian National University

Early Trabecular Compensation in Femoral Bone of the Diabetic NOD·B10 *foz/foz* Mouse

A thesis submitted for the degree of

Master of Philosophy

At the Australian National University

By Madeleine S.M. Fleming

December, 2021

Declaration

I, Madeleine Fleming, hereby declare that this thesis is my original contribution to fulfilling the requirements of the Master of Philosophy at ANU. The project was undertaken during my candidacy. I am the sole author and have attributed the source of ideas, references, and quotations of others by citation.

This project was a collaboration sharing the animal model of the Nolan group, ANU Medical School. Mice were raised by Dr Viviane Delghingaro-Augusto per ethics protocol (A2017/25). My project utilised this model to focus on bone tissue adaptations.

The work of this thesis has not been previously submitted to a university or other institution for examination.

_____

Madeleine S.M. Fleming

December, 2021.

Word count: 31,652 excluding tables, figures and bibliography

Acknowledgements

First and foremost I would like to thank Associate Professor Rachel Li. As primary supervisor, Rachel has mentored me through this project and fostered an inquisitive mind while my scientific process was refined. Thank you for your kindness and constructive advice, I have learned so much with your guidance and have enjoyed both professional and personal growth under you.

My gratitude is also extended to Dr Viviane Delghingaro-Augusto, co-supervisor for your generous collaboration sharing your precious *foz/foz* mice. Thank you for developing my research interest in diabetes and providing valuable discussion and insight to the project.

My appreciation to Dr Justyna Miszkiewicz, co-supervisor for helping me discover my fascination with bone tissue as a marker of health and disease. Thank you for encouraging me to pursue research, and for contributing your skeletal biology expertise to the project.

In addition to this trifecta, I would like to thank Professor Paul Smith AM, co-supervisor for your clinical insight and orthopaedic excellence. Thank you for both your infectious passion for research and encouragement along the way. I am proud of this contribution to your field.

Beyond my supervisory panel, I wish to thank Dr Donghai Zhang and Mr Jin Dai for your assistance learning the laboratory techniques, I have enjoyed working with you both. Thank you to Ms Bethany Partridge, a visitor to our lab group who was happy to assist in image processing. Thank you to Ms Cathy Gillespie, of the Imaging and Cytometry Facility at ANU for teaching me to use the micro-CT scanner.

My thanks are extended to the wider TORU group, the ANUMS and JCSMR colleagues and peers for providing a wonderful working environment. I have enjoyed many presentations, projects and discussions with you all and wish everyone the best with their research endeavours.

I am most grateful to my parents and brother for supporting me. I am also forever indebted to a wonderful community of friends. Your support is appreciated. Thank you of course to the Woden Valley Swim club, to the swimmers, parents, and colleagues who supported my employment at the club all the while undertaking my Masters. My final thanks to Steve Young, Steve Meredith and Neil Kennedy as you have all enabled me to learn and flourish.

Abstract

Bone mineral density (BMD) does not adequately predict bone fracture risk in contemporary type 2 diabetic patients. The rising prevalence of younger onset diabetes and obesity together reveal an endemic fragility for diabetic patients with equal or higher BMD than non-diabetics. Other factors contribute to this paradoxical fracture risk jeopardising skeletal acquisition and lifetime bone remodelling capacity.

NOD·B10 mice are susceptible to obesity and diabetes unlike the BALB/c strain which are only obese under identical genetic (*foz/foz*) stress. These strains enable investigation of diabetes-specific features distinct from obesity in the co-morbid NOD·B10 group. High fat (HF) feeding accelerates disease acquisition, enabling investigation of trabecular bone parameters and gene expression changes of the femur with earlier diabetes onset. We hypothesised that younger diabetic mouse bone would corroborate the BMD paradox, but expected structural and biochemical changes in trabecular bone from enhanced metabolic adaptation in this growth-emphasis project.

Female wild type and *foz/foz* littermates were raised and fed a standard or HF diet from 4 to 13 weeks of age on either BALB/c (*n=29*) or NOD·B10 (*n=30*) background. Fed-state body weight, insulin and blood glucose concentrations were obtained at end point. Serum was collected at sacrifice and hind limbs were dissected. Right femurs were preserved for micro-CT scanning and BMD measurement. Left femurs were processed for osteogenic gene expression profile by PCR array. ELISA was performed on serum samples to determine peripheral concentrations of a selected protein implicated by the PCR array.

At 13 weeks of age, HF-fed NOD·B10 *foz/foz* mice were diabetic and obese, whereas corresponding BALB/c mice were merely obese. Healthy mice and diet or genetic stress groups achieved desired phenotype spectra for comparison. HF-*foz/foz* NOD·B10 mice revealed equivalent BMD to non-diabetic groups as expected.

Diabetic NOD·B10 mice reflected thinner trabeculae than HF-WT mice, and a tendency (albeit statistically insignificant) for more trabeculae implicating expanded surface area within the distal femur. Mice of a given strain were otherwise microstructurally alike, with consistent cortical indices, bone volume fraction and BMD. Unexpectedly inter-strain comparisons were not possible by the stark contrast in trabecular features between NOD·B10 and BALB/c mice, irrespective of treatment conditions.

Despite largely maintained femoral microstructure amongst NOD·B10 littermates, HF-*foz/foz* mice revealed a quiescent osteogenic profile with under-expression of *Runx2, Igf1r, Fgfr2* and *Phex* insinuating early osteoblast inhibition and subsequent mineralisation loss. Chow-*foz/foz* mice revealed relative over-expression of *Fgf1, Anxa5* growth factor and mineralisation genes suggesting metabolic stimulation with establishing pre-diabetes. This distinction prompted analysis of FGF1 protein expression in serum. Difficulties in the result determination proved inconclusive, however putatively suggested raised FGF1 levels in diabetic serum.

Taken together, these findings support the clinical notion of trabecular bone appraisal with BMD measurement. Earlier diabetes onset provokes a younger and altered mode of skeletal dysregulation to conventional aging studies. This project characterises the femoral bone microstructure of the female NOD·B10 *foz/foz* model for the first time, demonstrating inherent differences to the BALB/c strain which are vital to future study design and interpretation.

Thesis-Related Publications, Awards and Presentations as First Author

Fleming M., Lin G.D., Li R.W. (2021) Omics Technologies and Development of Anti-diabetic Therapies from Prospective Natural Products. In: Mandal S.C., Chakraborty R., Sen S. (eds) Evidence Based Validation of Traditional Medicines. Springer, Singapore.

Fleming M., Delghingaro-Augusto V., Smith P.N., Li R.W. (2020) Bone mineral density and biochemistry of obese type 2 diabetic mice. ANUMS HDR Symposium, ANU, Australia.

Fleming M., Delghingaro-Augusto V., Smith P.N., Li R.W. (2019) Trabecular bone microstructure of the NOD·B10 foz/foz: a mutant mouse model complexed by diet. ANUMS HDR Symposium, ANU, Australia. 2nd Prize, Oral presentation.

Fleming M., Delghingaro-Augusto V., Smith P.N., Li R.W. (2019) Altered bone microstructure of the NOD·B10 foz/foz: an obese, diabetic mouse model. AOA ACT Annual Scientific Branch Meeting, TCH, Australia. Best Student Paper, Oral Presentation.

Table of Contents

Table of Figures

Table of Tables

Abbreviations

°C	degrees Celsius
26S	26 sub-unit
3D	three dimensional
4PL	4 parameter logistic
A260/A280	absorbance ratio 260/280 nm
AC-3	adenyl cyclase 3
Acvr1	activing receptor type 1
ADA	American Diabetes Association
ADAM	assignment of a disintegrin and metalloproteinase domain
AGE	advanced glycation end product(s)
Ahsg	alpha-2-HS-glycoprotein
AIHW	Australian Institute of Health and Wellbeing
Akt	protein kinase B
Alms1	Alström 1
ALP (alpl)	alkaline phosphatase
ANOVA	analysis of variance
ANU	Australian National University
AP-1	activator protein 1
APC	adenomatous polyposis coli

APF	Animal Phenomics Facility
ATF4	activating transcription factor 4
ATP	adenosine triphosphate
Atp6v0d2	d2 isoform of vacuolar (H+) ATPase (v-ATPase) V0 domain
B10	C57/BL10
B6 (vitamin)	pyridoxine
BAPN	β-aminopropionitrile
BCL	B cell lymphoma
BGLAP	bone gamma-carboxyglutamate protein
Bgn	biglycan
BIR	Biomedical Imaging Resource
BLC	bone lining cell(s)
BMD	bone mineral density
BMI	body mass index
BMP	bone morphogenic protein
BMU	bone multicellular unit
BRC	bone remodelling canopy
BSP	bone sialoprotein
C/EBP	CCAAT/enhancer binding protein
$Ca_5(PO_4)^3(OH)$	hydroxyapatite
cAMP	cyclic adenosine monophosphate

CD36 (Cd36)	cluster of differentiation 36 (antigen)
CDC	Centre for Disease Control and Prevention
Cdh11	cadherin 11
Chrd	chordin
CI	confidence interval
CKIα	casein kinase I-alpha
CLCN7	chloride-bicarbonate passive transport channel
cm	centimetre
CML	N^{ε}carboxymethyl lysine
Col	collagen
c-Src	proto-oncogene tyrosine-protein kinase
C_T	threshold cycle
CTSK	cathepsin K
CTX	C-terminal telopeptide of type 1 collagen
Cu (II)	Copper $^{2+}$ ion
DA	degree of anisotropy
DAP12	DNA X-activating protein of 12 kDa
DC-STAMP	dendritic cell specific transmembrane protein
ddH2O	double distilled water
DDR2	discoidin receptor 2
DEPC	diethyl pyrocarbonate

DEXA (DXA)	dual energy x-ray absorptiometry
dH2O	distilled water
DICOM	digital imaging and communications in medicine
DIO	diet induced obesity
DISH	diffuse idiopathic skeletal hyperostosis
Dkk	dickkopf
dl	decilitre
Dlx5	distal-less homeobox 5
DM	diabetes mellitus
DMP	dentin matrix protein
ELISA	enzyme linked immunosorbance assay
ERK	extra-cellular signal related kinase
ETS	E26 transformation-specific
FACS	flow assisted cell sorting
FasL	Fas ligand
FcRγ	fragment crystallisable receptor gamma
FGF	fibroblast growth factor
Flt1	FMS-like tyrosine kinase 1
Fn1	fibronectin 1
FRAX	fracture risk assessment score
Gdf	growth differentiation factor

GIP	glucose-dependent insulinotropic peptide
Gli	GLI-Kruppel family member
GLP-1	glucagon-like peptide 1
GLUT-4	glucose transporter type 4
GM-CSF	granulocyte-macrophage colony-stimulating factor
GSK3-β	glycogen synthase kinase 3β
Gusb	glucuronidase, beta
HA	hydroxyapatite
HbA1C	glycated haemoglobin
HDAC	histone deacetylase enzymes
Hes	hairy enhancer of split
Hey	HES-related repressor proteins
HF	high fat
HFD	high fat diet
Hh	hedgehog
HIF	hypoxia inducible factor
HO	heterotopic ossification
HRP	horseradish peroxidase
HSC	haematopoietic stem cell(s)
Icam	intracellular adhesion molecule
IGF	insulin-like growth factor

IHH	indian hedgehog
IKB	inhibitory kappa b
IKK	IKB kinase
IL	interleukin
IRF-8	interferon regulatory factor 8
ITAM	immunoreceptor tyrosine-based activation motif
Itga	integrin alpha
Itgb	integrin beta
JNK	c-Jun N-terminal kinase
kcal	kilocalorie
Kvp	peak voltage
L	litre
LCN	lacuno canalicular network
LEF-1	lymphocyte enhancer binding factor
LOX	lysyl oxidase
LOXL	lysyl oxidase like
LRP	low-density lipoprotein receptor-related protein
LTQ	lysine tyrosylquinone
MAC	McMaster Arthroplasty Collaborative
MC3T3	*Mus musculus* calvarial cell line
M-CSF	Macrophage-colony stimulating factor

MEK	mitogen activated protein kinase kinase
mg	milligrams
Micro-CT	micro-computed tomography
mins	minutes
MITF	microphthalmia-associated transcription factor
MJ	megajoules
MLO-Y4	murine long bone osteocyte-Y4 cell line
mm	millimetre
mM	millimolar
mmol	millimol
MMP	matrix metalloproteinase
mRNA	messenger RNA
ms	millisecond
MSC	mesenchymal stromal cell(s)
NFATc1	nuclear factor activator of T cells 1
NFKB	nuclear factor kappa b
ng	nanograms
NICD	notch intracellular domain
NIDDK	National Institute of Diabetes and Digestive and Kidney Diseases
NIK	nuclear factor kappa b kinase
nm	nanometre

NO	nitric oxide
NOD	non obese diabetic
Nog	noggin
OD	optical density
ODF	osteoclast differentiation factor
Op. V	open pore volume
OPG	osteoprotegerin
OSCAR	osteoclast-associated immunoglobulin-like receptor
OSE2	osteoblast-specific element 2
P1NP	procollagen type 1 N propeptide
PCP	planar cell polarity
PDGFA	platelet derived growth factor subunit A
PFA	paraformaldehyde
pg	picograms
PGE2	prostaglandin
PGI2	prostacyclin
PHEX	phosphate regulating gene with homologies to endopeptidases on the X-chromosome
PI3K	phosphatidylinositol 3-kinases
PJI	post-operative joint infection
PLC-γ	phospholipase C-gamma

PLP	pyridoxal 5’-phosphate
Po.Tot V	total pore volume
PPAR-γ	peroxisome proliferator activator receptor-gamma
Ptc1	patched 1
PTH	parathyroid hormone
PTHrp	parathyroid hormone related protein
RANKL	receptor activator of nuclear factor kappa b ligand
-RGD	arginine-glycine-aspartate
ROI	region of interest
Ror2	receptor tyrosine kinase like orphan receptor 2
ROS	reactive oxygen species
rpm	revolutions per minute
RT	room temperature
RT-qPCR	real time quantitative polymerase chain reaction
RUNX2	runt-related transcription factor 2
SCID	severe combined immunodeficiency disorder
SD	standard deviation
SDS	simple digital systems
sec	seconds
Serpinh1	Serine peptidase inhibitor, clade H, member 1
SMAD	small mothers against decapentaplegic

SMI	structure model index
Smo	smoothened
SOFA	stromal osteoclast forming activity
SOST	sclerostin
Sox9	SRY-homeobox 9
Sp7 (Osx)	osterix
STZ	Streptozotocin
T1DM	type 1 diabetes mellitus
T2DM	type 2 diabetes mellitus
TBS	trabecular bone score
TCF	T cell factors
TGF	transforming growth factor
THA	total hip arthroplasty
TKA	total knee arthroplasty
TMB	3,3′,5,5′-Tetramethylbenzidine
TMD	tissue mineral density
TNF	tumour necrosis factor
TRAcP	tartare resistant acid phosphatase
TRAF	transcription receptor-associated factor
TREM	triggering receptors expressed on myeloid cells
Twist1	twist homolog 1

Vcam1	vascular cell adhesion molecule 1
Vdr	vitamin D receptor
Vegf	vascular endothelial growth factor
w/w	weight per weight
WHO	World Health Organisation
Wnt	wingless-int-1
WT	wild type
x g	relative centrifugal force
αvβ3	alpha-v beta-3 integrin
µA	microampere
µm	micrometre

1 Cellular Composition of Bone

Inorganic bone mineral is predominantly ionic calcium and phosphate with secondary stores of trace and other elements. The crystalline reservoir is deposited by osteoblasts successive to organic osteoid secretion. Undesired bone is removed by osteoclasts in a process of degradation and endocytosis, or resorption. Bone modelling is achieved by independent recruitment of osteoblasts or osteoclasts, whilst bone remodelling is a physiological coupling of these opposing processes, orchestrated by osteocytes.

A mature sub-set of differentiated osteoblasts, the osteocytes comprise the dominant cell type of adult bone which integrate mechanical, biochemical, and other stimuli to co-ordinate a balanced response. Turn over occurs with the bone lining cell via an anatomic bone multicellular unit (BMU). Resorption and formation responses are subject to a myriad of signals integrated by osteocytes. Derangement of balanced response of osteoblasts, osteoclasts, osteocytes and accessory cells leads to bone pathologies, with substantial ramifications for systemic health and disrupted homeostasis.

1.1 Bone Tissue Overview

The connective tissue is distinguished by its hard, compressive resistance conferring strength [1]. Hydroxyapatite mineral and collagen fibres comprise bone, which is anatomically classified into five groups based on dimensions and subsequent properties: long, short, flat, irregular and sesamoid [2]. Bone forms in differing distributions to permit the porosity and lightness of the vertebrate skeleton. The dense, lamellar cortical compartment is ubiquitous to all bone types comprising approximately 80% of the total adult skeleton [3]. Long bones and the vertebrae also include a spongy, cancellous trabecular compartment enabling bone marrow residence and haematopoiesis contributing the remaining portion of bone tissue [1].

Bone is a dynamic tissue undergoing continual staggered renovation from embryonic development until death. This system is complex to support the integral functions of the skeleton: movement, ion homeostasis, organ protection and lymphoid niche provision [4]. Rudiment cartilage is converted to bone by modelling. Existing bone is repaired by remodelling.

The bone mineral density (BMD) is an indicator of hydroxyapatite content present in a composite bone and tissue sample. Clinically, the T-score is used to reflect BMD standard deviation comparative to a young, healthy person mean: values between +1 and -1 are

typical; from -1.1 to -2.4 indicates osteopenia, or a lower BMD; and -2.5 and below signifies osteoporosis [5]. A low BMD therefore indicates lower mineralisation of the tissue, and increased fragility by the loss of hardness. Meanwhile, a high BMD value, proposed to be above T-score of +3.2 indicates excessive mineralisation, known as osteopetrosis [6]. Thus a fine balance in bone turnover is critical to retain structural and biochemical functions [4]. Disease can alter this homeostasis. It is imperative to understand how bone cell types are impacted by disease, and how this affects bone function leading to systemic and local modifications for therapeutic exploration.

1.1.1 Osteoclasts

The motile, resorbing cell type capable of degrading mineralised matrix facilitating bone remodelling discovered by Kölliker (1873) [7]. Osteoclasts originate from myeloid progenitors of the self-renewing haematopoietic stem cell (HSC) niche, differentiated from dendritic and monocyte cell fates by cytokine exposure [8]. The precursor resident in bone marrow responds to macrophage-colony stimulating factor (M-CSF, or CSF-1), promoting proliferation and sensitisation to receptor activator of nuclear factor kappa b (NF-KB) ligand (RANKL, or TRANCE) directing commitment to the osteoclast lineage [9]. Binding induces NF-KB, nuclear factor activator of T cells 1 (NFATc1) and calcium-sensing stabilisation pathways for osteoclastic differentiation [10].

Pre-osteoclasts travel to the site of resorption from local marrow or vasculature, and differentiate into osteoclasts under NFATc1-mediated dendritic cell specific transmembrane protein (DC-STAMP) exposure, initiating precursor fusion to become multi-nucleated, giant cells at the desired bone surface [11]. Differentiation pathways discussed below induce osteoclast-specific gene expression enabling distinction from monocytes. Osteoclasts create a resorption pit facilitating access to collagen fibrils, surviving for two weeks in humans, and days in mice, before apoptotic death and efferocytotic removal [12, 13].

1.1.1.1 Macrophage-Colony Stimulating Factor

Osteoclasts derive from myeloid lineage of the HSC responding to local M-CSF within the bone marrow stroma [14]. The colony stimulating factor 1 receptor (C-FMS, CSF1R) induces phosphorylation of several tyrosine residues, initiating a complex with proto-oncogene tyrosine-protein kinase (c-Src) [15]. Tyrosine residue phosphorylation events promote pre-osteoclast survival.

Osteoclasts are distinguished from macrophages by E26 transformation-specific (ETS) family transcription factor PU.1 and microphthalmia-associated transcription factor (MITF) complex co-activation [16]. PU.1 homozygous mutants cannot transcribe c-fms, failing to differentiate from myeloid progenitors [17]. MITF deficient (*mi/mi*) mice exhibit excessive bone deposition, known as osteopetrosis with failed osteoclastogenesis [18].

The mitf-E isoform shows constitutive osteoclastogenic gene expression regulation of *Clcn7, Ctsk, Oscar*, and *Tracp* genes, further enhanced with RANKL and NFATc1 induction [19]. The *op/op* mouse has low M-CSF in calvariae and reduced macrophage population in bone and marrow, implicating the importance of this axis for precursor and mature cell survival [20]. The CSF cascade is therefore crucial to enable RANK-sensitisation for further differentiation into osteoclasts [21].

1.1.1.2 Receptor of Activated Nuclear Factor Kappa B Ligand

RANKL (TRANCE/TNFRSF1111A) of the tumour necrosis superfamily is secreted by osteoblasts, osteocytes and hypertrophic chondrocytes [22-24]. Notably, osteoblasts and osteocytes mediate osteoclastogenesis by synthesising osteoprotegerin (OPG, encoded *Tnfrsf11b*), the decoy receptor for RANK competitively inhibiting RANKL to prevent excessive bone resorption and subsequent osteoporosis [25].

The findings of four independent labs in 1997 clarified OPG ligand was RANKL, previously identified as osteoclast differentiation factor (ODF) and stromal osteoclast forming activity (SOFA) [26-29]. Both $RANK^{-/-}$ or $RANKL^{-/-}$ mice have apparent osteopetrosis, failing to undergo osteoclast differentiation [30, 31]. Thus, the OPG ratio must be low, or the cumulative RANK expression saturative, facilitating RANK-RANKL binding dependent on M-CSF sensitisation.

RANKL binding to RANK at osteoclast precursor surface induces transcription receptor-associated factor (TRAF) 1,2,3,5, 6 interactions [32]. TRAF adapters regulate osteoclast activity, with TRAF 2, 5 and 6 activating NF-KB signalling and consequent osteoclastogenesis [33]. Darnay and colleagues demonstrated the motif-dependence of TRAF-mediated signalling, concluding TRAF-6 essential for NF-KB kinase (NIK) activation, and TRAF-2 for c-Jun N-terminal kinase (JNK) pathway [34]. Osteoclastogenesis proceeds via transactive NF-KB, c-JUN/JNK/AP-1, NFATc1 pathways.

1.1.1.3 Nuclear Factor-Kappa-Light-Chain-Enhancer of Activated B Cells

RANKL, TNF-α, and IL-1 among other inflammatory cues promotes rapid TRAF/TAK binding of the canonical NF-KB pathway. Precursors p100 (encoded *NFKB2*) and p105 (encoded *NFKB1*) are stabilised in the cytoplasm under inhibitory kappa B (IKB) protein regulation, in an assortment of dimers with Rel homology domain [35]. Nuclear NF-KB is exported to the cytoplasm under IKBα captivity [36].

TRAF6/TAK1 and TRAF2,5 co-stimulation initiate the IKB kinase (IKK) complex assembly: IKKα, IKKβ, and regulatory sub-unit IKKγ (or NEMO). IKKβ phosphorylates IKB-α and -β, polyubiquinated for 26S proteasomal degradation. IKBγ portion of constitutive p105 binds to Rel A, c-Rel and p50, degraded in the cytoplasm [37]. IKBα degradation releases previously sequestered p65 (RelA):p50 heterodimers, which can translocate to the nucleus and activate desired gene transcription.

IKB is essential to canonical signalling as $IKK\beta^{-/-}$ (HSC-specific deletion) mice could not form mature osteoclasts, and could not be rescued by pro-osteoclast signalling unlike IKKα null comparators [38]. Double knock-out $p50^{-/-}p52^{-/-}$ mice fail to thrive, with short bones, unerrupted teeth, insufficient bone marrow and severe osteopetrosis: demonstrating the importance of NF-KB pathways for terminal osteoclastogenesis enabling resorption [39, 40].

1.1.1.4 Nuclear Factor of Activated T Cells Cytoplasmic 1

The nuclear factor of activated T cells cytoplasmic 1 (NFATc1, encoded *NFAT2*) is regarded the master transcriptional regulator of osteoclastogenesis, with converging amplification [41]. Pre-existing NFATc2 responds to NF-KB and other RANKL stimulated transcription factors, inducing the initial NFATc1 activation loop [42]. NFATc1 directly induces β3 integrin to transactivate NFATc1 [43]. Calcineurin dephosphorylates NFATc1, which accumulates in the cytoplasm in response to transient calcium spikes [44]. Interferon regulatory factor 8 (IRF-8) is down-regulated by active RANKL, which raises NFATc1 expression by PU.1 switch, to promote osteoclastogenesis [45].

NFATc1 is imported to the nucleus, and docks to the Bcl-6 relinquished NFAT2 promoter region [46, 47]. The c-fos, of NF-KB origin and c-Jun of MAPK pathway form the activator protein 1 (AP-1) unit of the NFAT/AP-1 complex to initiate transcription of osteoclast-specific genes including cathepsin K (*Ctsk*), Tartare Resistant Acid Phosphatase (*Tracp*) and matrix metalloproteinase 9 (*Mmp9*) [41].

All of the c-Fos$^{-/-}$, TRAF6$^{-/-}$ and double knock out DAP12$^{-/-}$FcRγ$^{-/-}$ mice exhibit a spectrum of osteopetrosis with minimal NFATc1 induction [41, 48]. NFATc1$^{+/-}$c-fos$^{-/-}$ mice are not ostepetrotic compared to single knock out comparator c-fos$^{-/-}$ (whereas the NFATc1$^{-/-}$ null is embryonically lethal), rescued with ectopic NFATc2 to recommence NFATc1 expression [49]. The NFATc1 pathway is also dependent on intracellular calcium concentration, mediated by phospholipase C (PLCγ). PLCγ-mediated calcium flux provokes calmodulin-dependent kinase cascade, accentuating osteoclastogenic differentiation.

1.1.1.5 Tumour Necrosis Factor Receptor-Associated Factor Outputs

Three osteoclastogenic outputs derive from TRAF2/6 adapter stimulation to respective TNF-α and RANK: i) extracellular signal-regulated kinase (ERK); ii) p38 MAPK; iii) c-Jun N-terminal kinase (JNK). All three integral pathways influence transcription and expression of osteoclast-specific genes. In contrast to M-CSF/c-fms promotion of early survival by MAPK and Akt, RANK stimulation is prolonged and TRAF-dependent to advance terminal differentiation [50]. For example, p38α MAPK signalling promotes early expression of TRAcP via MITF phosphorylation, thereby progressing osteoclast functionality [51].

Inhibition of p38 MAPK prevented RANK-additive differentiation of osteoclasts and population depletion [50]. Therefore p38 activation of NF-KB and NFATc1 transcription factors bolsters similar activity to the ERK signal stream. M-CSF ERK survival signal is upregulated, strengthening c-fos expression and NFATc1 pathway. C-fos expression regulates JNK-mediated survival, as substrate phosphorylation and AP-1 complex formation with c-Jun prohibits cell death [25]. Together, these pathways converge to effect successful transcription of osteoclast genes, to support rapid functional destruction and removal of bone necessary to facilitate growth and recovery processes.

1.1.2 Osteoblasts

Osteoblasts derive from mesenchymal stromal cell (MSC) population of concomitant myoblasts, adipocytes and chondroblasts [52]. John Goodsir is credited with the first conceptual evidence of the modern osteoblast from examination of sponge skeletons with an achromatic compound microscope [53]. Partially committed osteoblastic progenitor cells are differentiated by responsiveness to runt-related transcription factor 2 (*Runx2* previously Cbfa1), distal-less homeobox 5 (*Dlx5)* and Osterix (*Sp7,* or *Osx*) expression as respective null mice do not form bone [54-56]. *Runx2* expression persists to bind to osteoblast-specific element 2 (OSE2), and regulates osteoblastic gene expression. *Runx2* is thus the master

transcription factor co-ordinated with ATF4 and *Sox9* expression to modulate bone formation pathways [57].

Osteoprogenitors respond to competitive *Runx2* signalling between promotional Wnt/β-catenin, BMP recruitment and opposing Notch and TGF-beta suppressive pathways. In support, *Runx2*$^{-/-}$ mice do not have osteoprogenitors, unlike *Sp7*$^{-/-}$ mice despite common bone insufficiency [58]. Later developmental signalling decreases *Runx2* expression to enable osteoblast maturity [59]. Competent osteoblasts are equipped with pronounced rough ER, mitochondria and Golgi apparatus for bone matrix protein synthesis. The cuboidal cells are basophilic, living for 3 months in humans or 10-14 days in mice before most die by apoptosis [60, 61]. Some osteoblasts differentiate into bone lining cells (BLC), and another sub-set become osteocytes, embedded in the mineralised matrix.

1.1.2.1 Notch

Skeletal Notch signalling maintains a checked MSC pool preventing progenitor cell commitment to osteoblastic fate [62]. MSCs expressing a Notch receptor (1, 2) bind Jagged (1, 2) and Delta-like ligand (1, 3, 4) families on adjacent cell membranes [63]. Metalloprotease disintegrin and metalloprotease domain (ADAM)10 mediated cleavage and successive γ-secretase cleavage (complexed by Presenillins 1 and 2) liberates the Notch Intracellular Domain (NICD) for nuclear import [64, 65]. NICD associates with CBF1, suppressor of hairless, lag-1 (CSL, or –RBP JK) transcription factor [66]. Consequent activation of hairy enhancer of split (Hes 1,5) and HES-related repressor proteins (Hey 1-3) suppresses *Runx2* activity thereby stemming osteoblastogenesis [67, 68]. Non-canonical signalling independent of Hes/Hey activation has been proffered to explain higher complexity in binary cell fate dictated by rapid NICD processing [69].

Notch regulation is highly stage specific. NICD over-expression under mature osteoblastic promoters *Col2a3* and osteocalcin bore lethal cell arrest: however the phenotype is viable under osteocyte DMP1 and osterix promoters achieving adult-onset osteopetrosis [70]. In agreement, late over-expression of NICD represses terminal differentiation promoting osteosarcoma from prolonged immature osteoblasts [71]. Ablation of all Notch receptors from osteoblast and MSC progenitors reinforces the developmental function of the pathway. young mice exhibit high bone mass by a depleted MSC niche; whilst aged mice have osteopenia, consequent of depletion and arrest over time [72]. Notch does not interfere with BMP or MAPK signalling pathways in osteoblasts or progenitors however antagonises differentiation pathways to retain progeny pool [73].

1.1.2.2 Wingless-Int-1

Wingless-Int-1 (Wnt) regulates cell development via the canonical (β-catenin), non-canonical planar cell polarity (-PCP), and non-canonical calcium (-Ca^{2+}) signalling pathways. Canonical Wnt signalling is crucial for *Runx2*-mediated osteoblastic differentiation overcoming repression [74]. Wnt ligands bind autologous or paralogous to Frizzled receptors, recruiting low-density lipoprotein receptor-related protein (LRP) 5 or 6 to preserve β-catenin [75]. Substrate accumulation permits nuclear entry to activate T cell factors (TCF-1,3,4) and lymphocyte enhancer binding factor (LEF-1) for *Runx2* co-operated transcription of osteoblastic genes [76, 77].

In absence of canonical Wnt ligands, Dishevelled co-receptor prompts complex assembly of glycogen synthase kinase 3β (GSK3-β) adenomatous polyposis coli (APC) and casein kinase I-alpha (CKIα) [78]. Unprotected β-catenin is tagged for 26S proteasome degradation and non-canonical procession ensues [79, 80]. Wnt/PCP signalling replaces LRP with Receptor tyrosine kinase like orphan receptor 2 (Ror2) co-receptor, facilitating Ryk cascade and JNK-mediated c-Jun recruitment promoting RANK synthesis [81]. The Wnt/Ca^{2+} pathway triggers IP3 transformation of MSC. Associated PLC-γ calcium spike up-regulates NFATc1 and NFKB pathways to trans-repress peroxisome proliferator activator receptor-gamma (PPAR-γ) and CCAAT/enhancer binding protein (C/EBP) preventing adipogenic fate [82].

Aberrant $LRP5^{-/-}$ mice have reduced bone deposition and trabecular volume causing osteoporosis pseudoglioma consistent with human mutation [83, 84]. LRP5 gain of function mutants achieve hyperostosis, osteosclerosis and osteopetrosis with excess osteoblastic function [85, 86]. Whilst $LRP6^{-/-}$ exhibit earlier bone loss than $LRP5^{-/-}$, both succumb to trabecular deficits as both co-receptors are essential to osteoanabolism [87]. Sclerostin and Dkk1 osteocytic proteins bind LRP5/6 extracellular domains, antagonising canonical Wnt signalling, contributing to osteoporosis [79, 88]. Wnt is an anabolic pathway of osteoblast differentiation and activity, with exquisite spatiotemporal regulation necessary to embryonic and post-natal skeletal growth and maintenance.

1.1.2.3 Bone Morphogenic Proteins

Bone morphogenic proteins (BMPs) are a sub-set of the transforming growth factor-beta (TGF-β) superfamily inherent for bone structure and maintenance. BMP receptors Type IA (ALK-3); Type IB (ALK-6); activin receptor (Acvr1, or ALK-2); and BMPII act synergistically to promote ligand-receptor phosphorylation cascades [89]. Receptor combinations trigger

small mothers against decapentaplegic (SMAD) 1/5/8 phosphorylation sequences, prompting heterotetramer formation with co-partner SMAD 4 facilitating nuclear translocation and Runx2-induced osteoblast gene expression [90, 91].

The SMAD-independent p38 MAPK/ERK pathway also promotes osteogenic expression positively regulating osteoblastic differentiation under BMP induction, pending receptor engagement sequence [92]. BMP 2, 4, 6, 7 and 9 are highly osteoinductive [93, 94]. Other BMPs synergistically boost osteogenic potential in ALP combination panels, with the exception of BMP3 a negative regulatory member [95]. $BMP3^{-/-}$ mice are embryonically unremarkable but older mice have higher bone mass and increased trabecular volume [96].

Conditional BMP 4, 6, or 7 knock outs retain normal skeletal architecture compensated by BMP2 [97, 98]. In contrast, BMP2 knock out is not adequately compensated sustaining inevitable fragility fractures [99, 100]. Similarly, unaffected single BMP2/4/7 conditional deletion in MSC progeny contrasts to double knock out BMP 2, 4 skeletal malformation: unlike BMP 2, 7 insufficiency [101]. Aside from BMP6, other osteogenic BMP null or SMAD null mutations are embryonically lethal underscoring the importance of competent BMP signalling to bone architecture [100].

1.1.2.4 Transforming Growth Factor-Beta

TGF-β 1, 2, 3 maintain the bone mass enacting coupling process of osteoblast and osteoclast differentiating populations [102]. Mechanism of binding tetramer of dual TβRI (ALK5) and TβRII to push phosphorylation cascade activating regulatory SMAD 2/3 to co-locate and translocate with SMAD 4 to the nucleus. This cascade recruits histone deacetylase enzymes (HDAC) to antagonise *Runx2* promotion [103, 104]. However, non-canonical SMAD-independent TGF-β pathway occurs via p38/MAPK/ERK [105].

TGF-β1 activation is necessary for osteoblast differentiation to osteocytes but also prevents mineral acquisition in cultures, contributing to the OPG/RANKL ratio influencing osteoclasts [106, 107]. Latent TGF-β is activated by osteoclast liberation from chaperone pro-segment, also promoting SMAD 2/3- mediated osteoclast differentiation via TRAF-6/TAB1/TAK1 signalling thereby coupling osteoprogenitors critical to attainment of bone mass and the continued remodelling process [108, 109]. Both TGF-β and BMP signalling are regulated by inhibitory SMAD 6 and 7, contributing to the feedback for upholding skeletal integrity.

1.1.2.5 Hedgehog

Indian hedgehog (Ihh) signalling is fundamental to long bone elongation (endochondral ossification) in mammals. Initial hedgehog (Hh) proteins are synthesised and exported to the endoplasmic reticulum [110]. Hedgehog receptor Patched 1 (Ptc1) excludes the transmembrane protein Smoothened (Smo) until Hedgehog ligand interaction [111]. Binding inhibits Ptc repression, localising Smo to trigger a migration cascade, enabling canonical Gli family zinc finger (Gli 1-3) protein associations and targeted gene transcription [112, 113]. Gli 3 is converted from repressor to activator form by Smo, favoured by Gli 2 aid, whilst Gli 1 remains an accessory transcription factor [114, 115].

In the embryonic and post-natal skeleton, Indian hedgehog is responsible for chondrocyte marginal expansion and osteoblastic deposition comprising endochondral ossification, as null mice lack mature osteoblasts at expansion of cartilage hypertrophy [116, 117]. Smo deletion confirmed osteoblast progenitor dependency on Ihh transduction for differentiation capacity to permit elongation of long bones [118].

Ihh activation of parathyroid hormone related protein (PTHrp) essential to chondrocyte responsiveness, and to osteoblastic faculties: increasing nodule formation, mineralisation and post-transcriptional regulation capacities [119-121]. Excessive Hh signalling in osteoprogenitors promotes heterotopic ossification and joint fusion disorders [122]. As osteoblasts mature, Ihh attenuates such that late over-expression causes osteopenia, and *vice versa*: Ihh inhibition protected elderly bone decline by retention of higher bone mass [123]. Thus, Ihh signalling is unequivocally required for osteoblastic growth, cell differentiation and subsequent function in post-natal remodelling for bone deposition and strength.

1.1.3 Bone Lining Cells

The bone lining cell (BLC) derives from osteoblastic lineage: generally considered a sub-set of mature, differentiated osteoblasts. Matured cells have down-sized osteoblastic organelles, coined ‘idle’ osteoblasts in 1981 [124]. Yet mechanism of differentiation, and thereby distinction from predecessor are irresolute. BLCs form a flat monolayer covering of bone surfaces, enforcing dormancy while communicating via gap junctions [125, 126].

Bone remodelling is initiated by BLC detachment, in humans transitioning to the sinus or bone remodelling canopy (BRC), to compartmentalise and couple resorption and formation [127]. The BRC structure has not been identified in mice and rodents, despite recognition

of the BLC quiescence and PTH response reported in 1976 [128, 129]. BLC populations are known to dwindle as bone ages, and are inactivated by glucocorticoid treatment [130, 131].

BLCs have been posed as a quiescent renewal population for adult osteoblast demand. In 1995 evidence of unchanged osteoblast number, yet marked increase in bone formation with PTH induction posited bone lining cell reversion to osteoblasts [132, 133]. Mechanical loading stimulus, FGF2 anabolism, and high dose gamma irradiation studies all showed increased bone formation despite consistent osteoblast numbers, with later exchange of BLC and osteoblast populations [134-136]. The reversion concept has been countered by the argument that BLC abundance (perhaps exceptionally in mice) is inadequate to drive osteoblast proliferation, as earlier studies could not account for pre-primed osteoprogenitors [60].

The remodelling contribution of BLCs is also of interest to bone research and remains to be well established. Administration of Sclerostin antibody has shown up-regulation of ECM and bone matrix protein expression patterns in BLCs [137, 138]. Furthermore, BLCs unlike osteoblasts were observed to participate in lacuna digestion with distinctive MMP13 secretion for clearing remodelling ground [139]. This observation was further supported when repeated in CTSK-deficient mice who did not perform osteoclastic resorption [139]. Compiling these outcomes, evidence suggests that the BLC has a biochemical role in physiological coupling in addition to spatial provision.

1.1.4 Osteocytes

The trans-differentiated osteoblast population, osteocytes live for 25 years in humans, comprising 90-95% of total bone cell abundance [140]. Entrapped in lacunae, osteocytes project stellate, cytoplasmic extensions into canaliculi channels [141]. Connexin 43 gap junctions are maintained to integrate communication with all components of the bone environment [142]. The resulting lacuno-canalicular network (LCN) serves a conduit for exchanging waste, nutrients, minerals, osteoprogenitors and upholding the oxygen-tension environment for local bone tissue.

Once encased, pro-osteoblast genes (*OCN, BSP-II, Col1A1* and *ALP*) are down-regulated; while dentin matrix protein 1 (*DMP1*), sclerostin (*SOST*) and fibroblast growth factor 23 (*FGF23*) expression is high, marking osteocyte differentiation [143-145]. It is unclear whether this process is terminal, as de-differentiation has been imposed *ex vivo* to regain

osteoblast competencies [146, 147]. Three dimensional excavation of the interior compartment creates the Haversian system, or osteon [148].

Surface projections of occupied Howship (1817) lacunae detect shear stress fluid flow [149, 150]. Mechanosensation is converted to a piezoelectric discharge by which the primary cilia of osteocytes associate with polycystins and rearrange the cytoskeleton [151]. Osteocytes release prostaglandin (PGE2), prostacylcin (PGI2) and nitric oxide (NO) to coordinate subordinate osteoblasts and osteoclasts [152-154]. Osteocytes also influence bone cell differentiation. MSC progeny exposed to mechanically primed osteocyte media upregulated osteoblastic gene expression without affecting existing osteoblasts [151].

Calcein labelling revealed the calcium flux from osteocytes to induce early osteoblast differentiation [155]. In absence of DMP1, excess FGF23 causes rickets and bone softening known as osteomalacia [156]. Incomplete ablation of osteocytes (by diphtheria toxin) led to intact osteoblasts, however apparent deregulation with fragility fracture, loss of trabecular connectivity and proliferative bone marrow adiposity [157]. This loss of osteocyte modulation accelerated skeletal aging. In balance, sclerostin limits osteoblast activity to control bone deposition [145].

Osteocyte death is visible by DNA fragmentation, amongst microcrack damage and osteoclastic activity [158]. Due to matrix imprisonment, osteoclasts are remotely attracted to initiate lacunar turn over [159-161]. Lacunae must be vacated and pared back to enable bone remodelling in the young skeleton, or pathologically with bone over growth disorders [162].

1.2 Osteogenesis *alas* Ossification

During embryogenesis MSC of each embryonic lineage congregate at pre-determined sites and densely template the morphology of individual bone structures. Some progenitors differentiate into chondrocytes forming the anlagen cartilage scaffold for later endochondral ossification. Some MSC differentiate directly to osteoblasts for intramembranous ossification of the calvariae, viscerocranium and partial sections of the clavicles [163, 164]. Both osteogenic processes require angiogenesis to succeed. The paraxial mesoderm cell line forms the axial skeleton, whilst the appendicular skeleton forms from the lateral plate mesoderm; with the skull, face and dentin derived from neural crest and prechordal mesoderm cell lines [165].

The direct conversion of mesenchyme sheets to osteoblastic cells comprises the initial bone development in utero and continues with cranial suture fusions in 3rd and 7th decade of life [166]. MSC coalesce, differentiating to angiogenic or osteogenic cell types, forming the primary ossification centre of the embryo [167]. The connective tissue membrane is directly replaced by osteoid, creating a seam to differentiate internal bone from the periosteum. The woven trabecular bone interspersed with vasculature is encased by the dense cortical bone, expanding periosteal diameter with appositional growth.

1.2.1 Bone Modelling

Frost (1960) first proposed bone modelling as the refinement of bone structure to achieve correct shape and size during embryonic and skeletal ontogeny [149]. Bone sculpting continues throughout life via discrete recruitment of osteoclasts or osteoblasts in the case of fracture or damage even in elderly people [168]. Humans and rats showed concurrent slight, smooth cement lines lacking pores, indicative of resorption-independent bone formation [169, 170]. CTSK-mutants lacking osteoclasts validate bone formation independent of resorption [171]. Excision of the femur and subsequent tibial modelling consolidate Wolff's law (1892) of physiological adaptation [172, 173]. Periosteal modelling is a slighter process than remodelling enabling refinement of individual bone morphology in humans [3].

1.2.2 Bone Remodelling

A life-long cycle of staggered bone turnover is undertaken to replace structural flaws and liberate stored calcium. Remodelling events increase bone mass to 3rd decade whilst cells are plentiful and mechanical loading stimulates peak accrual. Past this time, remodelling contributes a gradual loss of bone as periosteal expansion continues in excess of bone replacement. Bone mass is retained in the cortical microarchitecture, as trabeculae are substituted by thinning cortical bone. The threshold to initiate a remodelling event is thought to 'drift' over time, creating an imbalanced repair mechanism with aging [174].

Osteon remodelling is staggered: younger tissue is supple, with lower mineral and cross-linkage. Older bone is reinforced to load, with less plasticity to recover deformations leading to osteoporotic brittleness. As vertebrates age the bone matrix incurs increasing loss of bone volume. If deposition is not adequate to fill osteons, the enlarged Haversian canal erodes, leading to higher porosity or microporosis [175]. Whereas excessive osteon mineralisation yields micropetrosis, and an over-filled trabecular network.

Unlike most mammals, mice lack true Haversian and supporting Volkmann's canals, through a simpler construct of primary osteons [176]. Mice typically achieve peak bone mass at 3 months of age [177]. During peak mass accrual trabecular turnover predominates by order of 10-fold higher surface area than cortical metabolism [178].

Remodelling is the procession of the basic multi-cellular unit (BMU): a cutting cone of osteoclasts flanked by closing cone of osteoblasts supported by vasculature and innervation. 4 phases of events must occur consecutively for a successful remodelling cycle: *initiation, resorption, reversal* and *formation*. A cortical BMU proceeds in three dimensions, whereas a trabecular BMU is limited to the bone surface [1]. Remodelling is encapsulated by BLC coverage and presided by osteocytes coupling osteoblast and osteoclast responses. More BMUs intuit more bone turn over, however continual remodelling can compromise structural integrity [179, 180].

1.2.2.1 Initiation

Osteocyte detection of damage above the tolerable threshold induces local bone lining cells to detach from the quiescent zone. The bone surface is exposed, with MMP13 secretion signalling pre-osteoclast recruitment to the designated BMU [181, 182]. Osteoclast precursors are delivered and selected under osteoblast-mediated RANKL and M-CSF expression [183]. NF-KB induced NFATc1 cascade promotes DC-STAMP and d2 isoform of vacuolar (H+) ATPase (v-ATPase) V0 domain (Atp6v0d2) expression facilitating fusion to multi-nucleated, giant cells [10, 184, 185].

Once terminally differentiated, osteoclasts undergo cytoskeletal rearrangement and polarisation oriented by four membrane domains [186]. The F-actin ring enlarges the plasma membrane, in response to local CD44 and αvβ3 integrin ordination, producing the podosome of ruffled border and the sealing zone domains, in contact with bone surface [187, 188]. The ruffled border of microvilli amplify the surface interactions within the sealing zone to strictly localise and concentrate degradation of the mineral interface.

1.2.2.2 Resorption

A resorption pit is formed with the degradation of hydroxyapatite crystal according to

$$Ca_3(PO_4)^2)^3\ Ca(OH)^2 + 8H^+ \leftrightarrow 10\ Ca_3 + 6HPO_4^{2-} + 2H_2O$$ [189].

Ion substitutions are inevitable leading to a non-stoichiometric crystal lattice generalised as hydroxyapatite [190]. The Atp6v0d2 co-ordinates with chloride-bicarbonate passive transport channel (CLCN7) to achieve electro neutrality [191, 192]. The carbonic anhydrase

II proton generator yields acid concentration for bone destruction, and optimisation of CTSK activity at the ruffled border [193].

Cleavage of Type I collagen into C- and N- terminus peptides provides a surrogate indicator of bone turnover [194]. Matrix metalloproteinases (MMP) predominantly MMP 9 are activated by CTSK, promoting an osteoclast survival cascade [195]. Terminal TRAcP expression further drives osteoclastic activity, generating reactive oxygen species (ROS) as a by-product of matrix degradation [196, 197]. Debris are endocytosed with liberation of calcium and side products into the bloodstream.

Raised calcium feedback limits further osteoclast activity by subsequent dissociation, fragmentation and apoptosis [198, 199]. Whilst incompletely resolved, osteoclast apoptosis appears a competitive reduction in proliferative signalling tandem to osteoblast domination of the RANKL axis. Osteoblast-promotional estrogen and OPG have been shown to increase Fas ligand (FasL) death receptors [200, 201]. Other mechanisms, such as TNF-related apoptosis-inducing ligand receptors (TRAIL) involvement remain to be clarified as redundant or significant in normal and pathological contexts [202].

1.2.2.3 Transition

The perceived intermission between resorption and formation is the transition phase, reversing the dominant cell type [203]. Previously, there was thought to be a discrete gap between osteoclast death and osteoblast activation, whereby an aborted cycle would impair bone deposition, advancing osteoporosis. There now appears an interrelated phase of mixed recruitment dictated by the fractional lifespan of osteoclasts compared to osteoblasts.

Lassen and colleagues propose an integrated ‘reversal-resorption’ process, observing a heterogeneous population of osteoblasts and osteoclasts exerting differential effects within a BMU [204]. The proximity of osteoclasts to newly formed osteoid surfaces indicates overlap in cell-type activations, and population density overriding osteoclastic survival [204]. Cell-cell contact between mature competing populations was observed *in vivo* by 2-photon microscopy: PTH administration showed osteoclasts deficient in TRAcP and CTSK; whereas non-anabolic vehicle lead to active constituent resorption [205]. Furthermore, the cross-talk and uptake of counterpart factors may obscure differential staining interpretations. Mature osteoclasts express pro-osteoblastic factors, also releasing osteoblast deposited cytokines with bone matrix degradation [206]. Thus the coupling process, by nature, remains difficult to delineate into particular cell aspects.

1.2.2.4 Formation

In humans, formation may occur weeks after resorption and total three months to complete [183]. Osteoblasts first synthesise and secrete collagen (largely Type I) and associated proteins onto void surfaces [207]. This competency is due to shared lineage with chondrocytes and potential to trans-differentiate to osteoblasts [208, 209]. Biomineralisation is the biphasic continuation: the apical membrane of osteoblasts oriented and responding to parallel matrix [148]. Osteoblasts secrete proteoglycan-digesting enzymes, taking up calcium via annexin-mediated ion channels into matrix vesicles [210]. Phosphate-based compounds are degraded by osteoblast-secreted alkaline phosphatase (ALP), liberating phosphate ions for uptake to matrix vesicles [211]. The pH gradient and extracellular fluid exchange are imperative to ion sequester, intermediate conversions and hydroxyapatite precipitation:

$$6HPO_4^{2-} + 2H_2O + 10Ca^{2+} \leftrightarrow Ca_{10}(PO_4)^6(OH)_2 + 8H^+$$ [212].

Within vesicles, calcium and phosphate unite, nucleated by the core complex to resolve insoluble hydroxyapatite crystal, which grows until piercing the membrane, imbibing crystals to the matrix [213]. Mineral addition to collagen matrix is limited by collagen abundance to impart osteoblastic growth factors, and acidic bone proteins creating an ionic gradient and conceptual ‘nucleation lattice’ complementing collagen orientation [214]. Mature osteoblasts comprise a single layer, with some extending cytoplasmic processes to the projections of osteocytes [215].

Matured osteoblasts have three cell outcomes: majority death by apoptosis; BLC differentiation; or osteocyte differentiation under incompletely understood alternative programming sequences [216]. Remodelling is successfully completed with return to quiescence, as a monolayer of BLC covering the newly remodelled surface. Each BMU is recruited independently, thus each event is staggered and discrete response to explicit damage within an osteocyte’s domain, such that bone aging is not uniform at the cellular level [1].

1.2.2.5 Osteoblast-Osteoclast Coupling factors

Osteoclast resorption liberates IGFs, TGF-β, BMPs, FGFs and PDGFA from the matrix, acting as coupling factors to unite transition phase exchange [215]. Similarly, mature osteoclasts express Wnt10b, BMP6 and sphingosine-1-phophate, ‘clastokines’ to recruit and promote osteoblasts, speculatively assisting with the transition in cell populations [217].

Whilst clastokine presence in *vitro* has shown promising formation in bone-mimetic scaffolds, their capacity to couple osteoblasts and osteoclasts is contentious [218, 219].

Direct contact was inferred from osteoclast migration amongst fixed osteoblasts in co-culture, however this may be mere diffusion [220]. In the context of bone remodelling occurring within a BMU, the physical interaction between osteoblasts and osteoclasts is unclear. Axon-guided protein ephrins and semaphorins are implicated across bone cell species, however findings are limited *in vivo*. Cross-interactions are further obscured by the unresolved reversal and/or BLC identities influencing respective cell activities and distributions. As the interplay and coordination of cell identities remains to be determined, definitive coupling cannot be ascribed to any one process or cell population. Therefore, all bone cell populations must be considered in health and disease states.

2 Diabetes and Bone Fragility

2.1 Diabetic Prevalence is Increasing

Diabetes mellitus (DM) is clinically defined by a glycated haemoglobin (HbA1c) level exceeding 6.5% or a fasting plasma glucose level of ≥126 mg/dL (7.0 mmol/L) according to the American Diabetes Association and World Health Organisation [221, 222]. DM remains modifiable rather than curable as a complex, systemic metabolic disease leading to progressive disability. The disease affects 425 million adults worldwide and the incidence is rising [223]. Whilst 1 in 10 American adults will have diabetes, low and middle income countries show the steepest increases leading to a global projection of 693 million cases by 2045 [223].

Diabetes mellitus is currently classified by two sub-types distinguished by means of insulin mismatch with dietary intake, diagnosed by elevated blood glucose levels. The overwhelming majority (90-95%) of diagnosed cases are type 2 diabetes mellitus (T2DM) as opposed to type 1 diabetes mellitus (T1DM) according to the National Institute of Diabetes, Digestive and Kidney Diseases [224]. T1DM is usually autoimmune, or an idiopathic loss of pancreatic beta cells preventing insulin production and secretion, whilst T2DM is the exhaustion of intact, competent beta cells borne of excessive dietary nutrition and subsequent insulin depletion [221].

2.2 Type 2 Diabetes Mellitus

T2DM was recognised in Australia as a national health priority in the inaugural 1997 report from the Australian Institute of Health and Wellbeing [225]. By 2017 53% of the Australian diabetes burden was attributed to obesity [226]. T2DM was typically of concern beyond middle age, at an estimated burden of 84% in adults aged 45-84 years old [223]. In addition to this expanding aging population at risk of the disease the Youth SEARCH study from the US reflects the increasing trend of childhood to adolescent onset disease (10-19 years of age) [224].

The pre-diabetic state is now a recognised, complex disorder foreshadowing the global diabetic potential. As an example, a reversible and long-standing pre-diabetic state of elevated HbA1c (5.8-6.4%) was reported in 84.1 million American cases in 2010 [224]. In tandem, rates of gestational diabetes have increased raising the likelihood of both foetal and post-natal disposition to T2DM [227, 228]. This intergenerational scope bodes new challenges for managing a chronic disease over a longer lifetime than previously encountered.

2.2.1 Structural Depreciation of Bone with Diabetes

In affluent countries, overall rates of total knee arthroplasty (TKA) and total hip arthroplasty (THA) are increasing to meet the demand of an expanding and longer lived aging population [229, 230]. Diabetic patients are a subset of elective total joint replacement cases, seeking surgical intervention after fracture or degradation of bone under low impact trauma. The increases in diabetes cases and surgical accessibility have powered detection of previously unknown compromises in bone integrity of T2DM.

2.2.1.1 Fracture Reappraisal

Historically fracture risk for T2DM was less apparent, due to constraints of the detection methods available and a different disease susceptibility to present time. Diabetic fracture risk appears to have changed with the scope of the disease that was less exaggerated in past populations. The 1980 Rochester population study reported increase in ankle and lower leg fractures amongst diabetic patients, however concluded no association between disease status and fracture risk [231]. Later retrospective analysis of this same population (1970-1994) by the previous authors found increased hip fracture beyond 10 years on the basis of age, prior fracture and osteoporosis [232].

Previous generations may have endured a slower onset disease. Less time lived with diabetes risks emphasis on other sources of bone degradation contributing to past fracture likelihood. A retrospective survey of T2DM patients in 5th to 7th decade reported hip and spine fracture incidence from 1997-2009: those with severe fractures by low BMD at the lumbar spine and hip exhibited greater mortality with more advance disease and medical intervention [233].

The transition in diabetes and co-morbid obesity was observed for the same Rochester population sampled from 1970-1989, as obesity incidence increased with longer duration of T2DM [234]. A recent longitudinal study of a Korean population aged 50 years and over found increased risk of hip fracture, irrespective of age past five years of diabetes [235]. Increasing likelihood of fracture with accelerated T2DM onset expands the profile of the classical aging disease, creating a growing orthopaedic demand.

2.2.1.2 Fracture Prevalence

Diabetic patients are more likely to fall due to hypoglycaemic episode, or sustain injuries due to sensory deficits and impaired mobility. Yet fall risk alone does not explain the observed incidence of diabetic fracture. Historically, the confinement of T2DM to the elderly

promoted the association between age, frailty and falling. Older patients were more likely to suffer falls, endured a longer time lived with T2DM and achieved senile osteoporosis thereby a diminished BMD and greater risk profile [236]. However, the realisation that diabetic patients typically have equal or higher BMD to non-diabetics, and yet higher risk of fracture is now an accepted paradox [237]. Changes to bone and bone mineral metabolism prior to age-related decline posit new dilemmas for younger onset and/or longer duration diabetes.

In conjunction with the expansion of T2DM, the rising prevalence of interrelated obesity has highlighted discrepancies in bone strength of diabetics. The protective effect of increased weight bearing does not mitigate diabetic fracture risk. Unlike non-diabetic obese patients, diabetes contributes to bone degradation such that bone strength and resilience are uniquely compromised in obesity-borne diabetes [238].

2.2.1.3 Fracture Aftermath

Upon fracture and orthopaedic intervention, diabetes cases reflect worse outcomes and increased risk of post-operative complications. Diabetic THA/TKA patients endured a longer length of hospital admission and impeded healing compared to non-diabetics [239]. Immunosuppression and metabolic dysfunction increase risk of peri- or post-operative joint infection (PJI) compounding disease management and successful recuperation [240]. Taken together, these factors contribute to the increased risk of revision surgery, and a potentiated loss of individual productivity whilst incurring costs to health services [241].

Patients taking anti-diabetic medications indicative of advanced disease have a greater likelihood of contralateral osteoarthritis or arthroplasty, leading to revision surgery and concurrent complications [242]. This issue highlights the necessity of understanding bone adaptations to diabetes which impact the orthopaedic, individual and global costs of joint replacement. Diabetic patients endure innate quality changes to bone microarchitecture and metabolism, coupled with fall risk jeopardising bone resilience to low-impact fracture. It is well established that many anti-diabetic medications impede bone health, also endangering users to hypoglycaemic fall with improper administration [243].

The prevalence of undiagnosed diabetes has soared. A retrospective study of HbA1c readings amongst elective THA cases revealed 31% of patients as pre-diabetic and 2.6% of patients unknowingly diabetic [244]. The concern of greater arthroplasty and unmanaged disease amongst the rise in overarching T2DM is important to consider in patient management and surgical outcomes.

2.2.2 Diabetes and Bone Mineral Density

Bone mineral density (BMD) is a measure of the mineralised hydroxyapatite content of bone tissue. BMD T-score 2.5 standard deviation below average hallmarks the osteoporosis typical of T1DM, or osteopenia at 1.5 standard deviations below [245]. Juvenile T1DM patients failed to achieve peak bone mass as a consequence of complete insulinopenia during skeletal growth [246]. Confirmation of this finding championed DEXA (or 'DXA' dual energy x-ray absorptiometry) for the measurement of BMD and correlative bone strength exhibited in T1DM and other bone disorders. Osteoporotic score by BMD prevailed erroneously as the sole indicator of bone fragility in population screening.

Krakauer and colleagues published the first evidence of a discrepancy in diabetic DEXA as T1DM patients had osteoporosis, whereas T2DM BMD T-score was equal or enhanced at the spine and femoral neck [247]. Unlike T1DM, reduced osteoblast formation rate and attenuated bone loss were demonstrated in T2DM patients, yet this pivotal evidence lacked power with inadequate follow-up 12 years later [247]. A retrospective cross-sectional study of adults 55 years or older from the Rotterdam population also found T2DM patients to have higher lumbar spine and proximal femoral BMD independent of obesity, age or osteoarthritis status [248]. Female T2DM patients of the study self-reported lower incidence of fragility fracture than non-diabetic women, whereas men showed similar incidence regardless of diabetes [248].

Over time, bone mineral densitometry and age alone were not adequate predictors of osteoporotic fracture in all cases except white postmenopausal women: drawing out the limitation of the technology in diversified cohorts [249]. More recently, patients from the Rotterdam study pre-THA showed those with T2DM achieved higher BMD than non-diabetics and a 47-62% increased risk of fracture [250]. This seemingly diabetic adaptation has grown traction in studies, however the mechanisms pertaining to a higher residual BMD are unresolved [238]. BMD has persisted as an important variable for bone evaluation, however lacks totality in correctly assigning fracture risk in complex disorders such as T2DM.

2.2.3 Obesity and Bone Mineral Density

Obesity has been regarded a safeguard against osteoporotic fracture, as a higher mineral content is afforded of a larger body and corresponding bone size. A retrospective Norwegian population study from 1974-1990 supported this 'mechanostat' theory as BMI was inversely correlated with hip fracture risk [251]. In agreement, gastric bypass

intervention for morbidly obese patients revealed 6- and 12-month bone architecture and strength deficits with significant weight reduction [252]. In contrast, ankle and upper leg fragility fractures were not protected by menopausal fat gains, albeit confounded by loss of estrogens and increasing age [253].

An observational study of obese and morbidly obese patients reported protective BMD with increased body mass, however did not adjust for death premature to age-related bone loss [254]. Longer lived patients achieved lower BMI and lower BMD with age-based sarcopenia leading to senile osteoporosis and frailty. Conversely, overweight and obese people experienced excessive wear on bone and joint surfaces leading to bone deficits and osteoporosis [255]. Bone is unarguably responsive to BMI exacerbated by physical obesity, but the heterogeneity of BMD outcomes require further context to truly resolve the questionably protective mechanisms at play.

Childhood obesity is associated with a larger bone size, however lower mineral content at weight-bearing sites [256]. A larger bone volume could improve the dissipation of increased mass over a greater area, especially with enlarged entheseal attachments of ligament to bone. However, bone strength and length increases in square proportion, unlike volume in cube proportion, leading to an imbalanced optimum in bone size to strength ratio. In mice an upper limit for BMD increases with exceeding BMI values was demonstrated [257].

In recognition of the more recent obese diabetic prevalence, a cross-sectional study adjusted BMD on the basis of BMI in people aged 30 or older, reporting a higher diabetic BMD at the femur neck, without improved strength outcomes [258]. By the third decade, skeletal function and underlying strength are determined by peak mass acquisition [259]. The seemingly protective effect of obesity remains to be ascertained, especially when compounded with the competing influences of T2DM during skeletal maturation.

2.3 Detecting Bone Fragility

2.3.1 Dual Energy X-Ray Absorptiometry

The DEXA method has received criticism for its true determination of bone fragility based on BMD outcome reporting [260]. Comparison of the proximal femur of pre-, peri- and post-menopausal women concluded low predictive strength and architecture from DEXA, nor representative cortical porosity as a function of age [261]. BMD was agreeable to cancellous bone volume fraction, perhaps justifying repositioning as one facet of bone properties. According to DEXA measurements, females had higher preliminary BMD which

fell below the male plateau by the 6th decade [262]. Conjecturally, females outlive males and require additional calcium and mineral reservoirs to sustain pregnancy and lactation contributing to this sex-specific dichotomy.

2.3.2 Trabecular Bone Access

Trabecular mobilisation is adaptive in both health and disease, thereby difficult to obtain from preserved specimens. Controversy to the BMD paradox originated from reliance on cadaveric bone as a proxy control despite lifetime remodelling [263, 264]. Indeed, ancient samples preserve the trabecular morphology and bone disease captured at time of death [265]. Improvements to imaging techniques and the increase in joint replacement procedures have expanded accessibility to native bone permitting exploration of other parameters than BMD alone.

Trabecular dynamics are exhibited biologically during pregnancy trimesters. Transformation of the compartment to accommodate additional weight bearing, hormonal and metabolic demands on the skeleton imposed by childbearing and lactation were apparent [266]. This demonstrable impermanence can be ambiguous necessitating the life stage, age, and other contextual parameters to accurately depict bone activity in health and disease processes.

A study of premenopausal diabetic women corroborated the importance of trabecular capture, finding high bone volume fraction under the initial osteoanabolism of early T2DM [267]. Trabecular loss and separation increased on the basis of HbA1c level and disease chronicity, supporting a trabecular-based inclusion in diabetes and bone assessment [267]. Trabecular microstructural analysis is especially imperative to address the increasing diabetic population without age-related bone loss. BMD is a timestamp of bone turn over, whilst dynamic indices of trabecular features add evolving content to contextual bone adaptations.

2.3.3 Clinical Tools for Predictive Fracture Risk

2.3.3.1 Fracture Risk Assessment Score

The fracture risk assessment score FRAX® is a predictive risk algorithm launched in 2008 by the WHO in response to the global burden of osteoporosis. Risk factors and BMD are inputted by clinicians to estimate a patient's fracture susceptibility and death risk over ten years, endemically calibrated to each country [268]. The tool received substantial criticism for its simplified ability, likened to using BMD T-score alone to infer fragility. Problematically

in practice, T2DM patients received an underestimate by FRAX® computation on the basis of an equal if not higher BMD input than non-diabetic patients [269]. Whilst femoral neck BMD served a better measure of true hip densitometry, fracture risk was not properly depicted by these inputs.

HbA1c has been used to adjust FRAX outcomes to stratify diabetic fracture risk in patients aged 50 years or older [270]. However gradations of glycaemic control require medications which also reduce bone qualities directly and indirectly, contraindicating HbA1c calibration of BMD. A 0.5 T-score subtraction for BMD, selection of the rheumatoid arthritis clinical risk factor in lieu of diabetic metabolism, and inclusion of lumbar trabecular bone score have been trialled to refine FRAX outcomes with limited improvement [271]. Ultimately, diabetic-specific inputs are necessary to accurately depict the risks of diabetic fracture by primary health clinicians and specialists. Mechanistically these factors and derived inputs are yet to be resolved.

2.3.3.2 Trabecular Bone Score

The trabecular bone score (TBS) is an alternative clinical prediction tool of DEXA-acquired texture analysis, independent of BMD. Lumbar TBS analysis of male subjects and non-osteoporotic women has shown promising representation of fracture likelihood [272, 273]. A 2009-2010 prospective study of Asian people with T2DM detected men at significant fracture risk, masked by BMD; whilst diabetic women under 65 also showed hidden fragility by TBS [274]. The Manitoba Canadian BMD registry also found superior fracture risk detection of middle to elderly adults, in contrast to BMD findings by using TBS [275].

TBS must be cautioned as site-specific: femoral and lumbar bone responses are distinct and one cannot be used to infer the other. However, the sensitivity of lumbar TBS has shown true prediction of osteoporotic, osteopenic and healthy femoral BMD in non-diabetic postmenopausal women [276]. Whilst promising, these findings support the specificity of BMD in this single cohort, already sensitive to the original BMD prognosis. As only one sub-group of a global population, clinicians are looking to expand TBS and verify its utility in practice. Appendicular TBS is currently under prospective investigation for orthopaedic applications [277]. Preliminary findings have not included direct assessments of TBS on femoral microtexture of diabetics.

The complexity of T2DM, its heterogeneity and synergistic co-morbidities have limited mechanistic causation for the increased fracture risk, despite the higher BMD. Whilst linked with osteoporosis, the span of diabetes duration, progress and contextual variations

present vast gaps in a systemic disease which affects the bone tissue. BMD is one indicator of bone status, long overused as a universal measure ineffectively. Incorporating bone microstructure, biochemical evidence and other attributes of bone quality are critical to interpret true bone strength and fragility. Other lines of evidence are necessary to resolve the now-apparent bone fracture dilemma for diabetics from which therapeutic and preventative measures can be drawn.

2.4 Biochemical Downturn of Bone with Diabetes

2.4.1 Advanced Glycation End Products

The excess of metabolites with T2DM provides abundant substrates for increased formation of advanced glycation end products (AGEs). Formed by the Maillard reaction (1912), AGEs are a non-enzymatic condensation of amino groups by reducing sugars, which undergo Amadori rearrangements to form irreversible aggregates [278]. Endogenous AGEs occur with aging as lipids, nucleic acids and proteins are all susceptible to glycation. The clinical HbA1c index is an AGE, demonstrating the disposition to accumulate harmful aggregates indicative of diabetes [279].

Type 1 collagen is especially susceptible to non-enzymatic corruption leading to altered physical and biochemical bone properties [280]. The subversion of enduring collagen cross-linkage yields a stabilised, poorly oriented and proteolytic resistant tissue comprising the major component of bone. Other integrin binding (-RGD motif) bone proteins are also susceptible to AGE modification leading to diminishing bone strength and increasing fragility [281]. Glycotoxic AGEs disturb bone cell functions perturbing turn over. The increased potential damage and inadequate repair processes can contribute to local stress of T2DM fracture risk [282].

2.4.1.1 Aging and Advanced Glycation End Products

The elevated lipid, protein, and glycaemic loads of T2DM can accelerate AGE catalysis and collagen modifications with disease progress. An increase in pentosidine fluorescence reported AGE accumulation alongside increasing cortical porosity and bone weakness with aging [283, 284]. These bone decrements may have contributed to the lag in fragility detection preceding longstanding disease and osteopenia. Frank diabetic rats had lower enzymatic cross-links and impaired bone strength, exhibiting higher fracture likelihood despite healthy BMD [285, 286]. These findings support an inadequate fracture profile on the basis of BMD alone, imploring AGEs as one aspect adding to the diabetic fracture puzzle.

Amongst osteoporotic fracture cases, osteoblasts and progenitors exposed to AGEs under-expressed *Runx2* and *osterix*, most pronounced in the diabetic sub-set [287]. However, pentosidine content alone cannot explain bone strength outcomes of diabetics compared to age-matched controls in both humans and rats, suggesting the presence of an underreported and broader AGE burden with T2DM [279, 288].

During post-translational modification, collagen glycation by addition of galactose and glucose to lysine and arginine side chains forms reversible AGEs. However, these moderate AGEs are susceptible to carbonyl stress by lipid peroxidation and rapid transformation to highly stabilised N^{ε}(carboxymethyl) lysine (CML), generating reactive nitrogen and oxygen species [289]. Oxidative stress is typically balanced by the scavenger receptor system, however exhausted over a lifetime of aging leading to elderly AGE accumulation. Premature surpass of the oxidative threshold by diabetes-induced AGE burden creates an established AGE environment in bone tissue historically masked in the elderly.

2.4.1.2 Carboxymethyl Lysine

A prospective US study of male elderly patients (median 78 years of age) found increasing CML as a BMD-independent risk factor of hip fracture even with diabetic adjustments [290]. CML is now ubiquitous in processed food, and enhanced by modern cooking practices, leading to heightened exposure and higher AGE burden than the past [291, 292].

Non-diabetic wild type CD-1 mice fed an AGE-enhanced high fat diet demonstrated a perturbed hypothalamic-pituitary axis implicated in obesity and insulin resistance [293]. The excessive intake of AGEs and pre-cursors increases likelihood of bone deposits. Chronic low-grade inflammation, excess metabolites and limited bone cell resilience underscore the diabetic disposition to fracture. Following this premise, the discovery of CML revolutionised AGE pathology in diabetes and end-organ disease.

Recently, Erckhardt and colleagues showed these findings in a T2DM mouse model, discovering premature osteocyte senescence and high CML levels in both serum and bone [294]. Together, high glucose and AGEs are evident of unoccupied lacunae and increasing cortical porosity contributing to the secondary osteoporosis of longstanding T2DM [287, 295]. More work is required to address the dynamic interaction of short-lived osteoclasts and the longevity of osteoblast cell types. This temporality is further evident in skeletal remodelling, with contrary AGE findings in trabecular and cortical bone types.

Odetti and colleagues reported the cancellous fraction comprised 6 times less pentosidine than cortical bone, in a peri-surgical cohort of mean age 74 years [296]. Interestingly, the authors noted an exponential rise in pentosidine content amongst the 65-70 year old age bracket, suggesting that by this time of trabecular loss and cortical bone remainder, that AGE accumulation reflects aging [296].

However, Karim and colleagues used cadaveric samples of a wider age range to report increasing content of AGEs in trabecular bone by way of the increased trabecular surface area [297]. Furthermore, that the pentosidine contribution was a small portion of total AGE content in either type of bone, but detected at higher levels in trabecular than cortical samples [297]. This discrepancy underscores the importance of establishing age-specific perturbations of the skeleton, considering earlier onset of T2DM and the skeletal ramifications for premature bone cell dysfunction.

2.4.2 Lysyl Oxidase-Mediated Collagen Assembly

Vertebrate type 1 collagen requires several highly regulated post-translational modifications to achieve the final, multi-valent structure from the pro-collagen alpha chains [298]. Once exported, the lysyl oxidase (LOX) enzyme oxidises and deaminates precursor lysine and hydroxylysine groups into a condensation of inter- and intra-molecular cross links to achieve a functional tissue. LOX activity requires both Cu (II) ion and lysine tyrosylquinone (LTQ) co-factors to catalyse fibrillogenesis to generate tensile collagen [283]. This assembly is influenced by the intersection of mounting AGEs, raised homocysteine, and lowered pyridoxine of diabetes. The LOX family LOX and LOX-like 1 to 4 (LOXL1-4) are sensitive to oxidative stress and inflammation, with transcriptional repression potentiating the suppression of bone formation borne of T2DM.

2.4.2.1 Osteolathyrism

Famine-driven consumption of *L. odoratus* revealed the irreversible chelation of the LTQ co-factor preventing multi-valent collagen stabilisation [299]. Incubation with lathyrogen β-aminopropionitrile (BAPN) rendered chick osteoblast cultures lacking mineralisation, with reduced collagen assembly despite unaltered CTX secretion [300]. This loss of inorganic nucleation is supported by the co-localisation of LOX and active TGF-β necessary for mineral apposition [301]. Accordingly, LOX-family deficiencies support the necessity of LOX function to bone quality and both direct and indirect effects on BMD. The calvarial osteoblasts of $Lox^{-/-}$ null mice under-express Lox-family genes; proteins COL1, BSP,

RUNX2; with evidently lower differentiation and mineralisation competencies than wild type (WT) isolates [302].

LOX is highly expressed in adipose tissue, correlated with BMI in obesity irrespective of glycaemic status [303]. Amongst bariatric surgical patients, BAPN treatment reduced free fat mass and collagen correcting the typical loss of adiponectin and GLUT-4 in dysfunctional adipocytes [303]. In contrast, diabetic-AGE conditions revealed lower LOX expression in osteoblasts cultured with CML via the discoidin receptor 2 (DDR2), an integrin independent collagen receptor [304]. Metabolic aging and cumulative stress of obesity-borne T2DM may contribute to the interplay of AGEs, lost collagen integrity and ultimate fracture likelihood once postulated in the aging [305, 306].

2.4.2.2 Hyper Homocysteine and Vitamin B6 Deficiency

Pyridoxal 5'-phosphate (PLP, or Vitamin B6) deficiency and elevated homocysteine levels together impaired LOX and collagen stabilisation contributing to bone fragility of diabetes [285, 307]. Experimental B6-deficient rats demonstrated inferior cross-linkages, and higher solubility than WT bone collagen, which established PLP as a co-factor for ε-amino removal from lysine and hydroxylysine residues [308].

An essential dietary compound, PLP vitamers are crucial to metabolic functions: an antioxidant and AGE salvage co-enzyme thought to intercept harmful CML conversion [309, 310]. The excess adipose generated through obesity consumes PLP preventing AGE interference [311]. Adequate pyridoxine is crucial to prevent pathological elevation of homocysteine levels, as in diabetic Vitamin B6 deficiency and/or excess methionine intake [312, 313].

Diabetic hyperinsulinemia promotes excess homocysteine, problematic for its numerous detriments to bone and collagen [314]. Homocysteine directly inhibits LOX by competitive binding and modification of the LTQ active site, alike BAPN [315]. Non-diabetic CD-1 mice revealed a durational response to hyperhomocysteine, with early loss of tissue mineral density, and compensatory increase in osteocytes; later altered with increased apoptosis and mineralisation expression (*Dmp1, Phex, Sost*) formative of micropetrosis [316].

Irrespective of BMD, hip fracture patients reported less cross-linkage, higher pentosidine content, hyperhomocysteine and low PLP, corroborating animal evidence of an inferior and static bone collagen in methionine excess [285]. Diabetic amplification of this process

remains to be fully recapitulated, thus more work is required to deduce bone cell population dynamics implicated by the current body of knowledge.

2.4.2.3 Incretins

Incretins are enteric hormones which modulate post-prandial glucose homeostasis stimulating insulin secretion. The glucose-dependent insulinotropic peptide (GIP) acts on pancreatic beta cells, adipose, and other organs to regulate hyperglycaemia with pathological deficits in T2DM [317]. GIP is also osteoanabolic with receptors on osteocytes and osteoblasts raising both intracellular calcium and converting cyclic AMP (cAMP), facilitating P1NP and ALP secretion [318, 319]. Mineralisation and collagen synthesis are preferentially increased at the expense of osteoclastogenic activity via GIP signalling [320]. In contrast, diabetes abolishes the incretin effect of GIP, common across various diabetic (eg. iatrogenic, frank, T1DM) phenotypes [321].

Adversely, the other major incretin Glucagon-like Peptide 1 (GLP-1) does not have receptors expressed in bone cells, remaining intact under diabetes [322]. In accordance, T2DM subjects demonstrated raised serum CTX however maintained P1NP levels, exerting a loss of remodelling with GIP attenuation under hyperglycaemia [323]. Bone turnover is impeded under hyperglycaemic alteration of the GIP-GIPR axis, shown in MC3T3 cell cultures as compromised cAMP activity, down-regulation of LOX and subsequent collagen immaturity [324]. A murine diabetic study verified this interaction, suggesting hyperinsulinemia-derived peripheral dopamine corruption of the GIP-LOX-bone axis as an impetus for bone stasis [325].

2.4.3 Competitive Adiposity

Age-related bone marrow proliferation enacts bone turn over by expansion of the medullary cavity [326]. This enlargement is intertwined with exhaustion of osteoprogenitors under growth attenuation and age-mounted stress. Fuel surfeit promotes adiposity within bone marrow at the expense of osteoprogenitors within the MSC pool. This maladaptation of aging is exacerbated by diabetes and orexigenic dietary pressures cultivating potential bone pathology.

Adipose hypertrophy and increased insulin signalling strategy are necessary to accommodate surplus metabolites, demonstrating the bone marrow MSC re-programming towards adiposity [327, 328]. High fat diet (HFD) assignment with tibial fracture impeded callus healing in male C57/BL6 mice with comprehensive localised peroxisome proliferator

activator receptor-gamma (PPAR-γ) response at the injury site [329]. Whilst C/EBPS -beta and -delta isoforms are necessary to *Runx2* and osteocalcin-modulated ossification processes, congregation of all four isoforms drives adipose proliferation [330, 331]. The temporality of this process is critical to bone tissue balance.

When young and older mice were subject to 60% kcal HFD then switched to normal diet, young mice were unable to recover lost bone at the femur metaphysis as the initial osteogenic threshold was lowered irrevocably [332]. The fate-committed deviation in the osteoblast MSC population could limit crucial gain of BLCs and osteocytes available in the growing skeleton. These population dynamics take time to amass, as 12 week HFD regime in 3 week old male C57/BL6 mice demonstrated increased marrow adipose proliferation, without detectable changes to cortical and trabecular features [333].

Mice started later on HFD show contrasting findings, with skeletal defects in femoral bone volume, fewer trabeculae and higher resorption markers apparent by 3 weeks of HF feeding [334, 335]. Building upon the diet induced obesity (DIO) studies, a comparison of TallyHo diabetic mice with SWR controls showed prolific marrow adipose expansion, consistently lower BMD and similar trabecular deficits to the prior studies, with lower remodelling at 17 weeks in the diabetic group [336].

Temporal changes coinciding with peak growth, skeletal osteoanabolism and circulating entities intersect younger onset diabetes. Contemporary obesity-borne T2DM may be distinguished from obesity by the prevalence of AGEs in both adipose and bone tissue [337, 338]. AGE interference during peak mass achievement could potentiate critical deficits in mature cell populations, unable to recover from diet imposed sanctions with less successive cycles of mineralisation.

This is especially crucial for osteocyte longevity and critical regulation density which may ultimately contribute to both the adipose-driven expansion of bone and loss of bone homeostasis. Generic adipose proliferation is bidirectional to obesity and insulin resistance foreshadowing pre-diabetes, setting precedent for obesity-borne T2DM and bone disorder [339]. More work is required to assess these processes together. A first step is to include bone marrow adipose in biochemical bone assessment to truly profile the overlapping contingencies of the tissues.

2.4.4 The *foz/foz* Mutation for Obesity-Borne T2DM Research

2.4.4.1 Discovery of the *Alms1 foz/foz* Mutation

The *foz/foz* genotype was derived from an 11 base pair truncating deletion of base 3918, exon 8, chromosome 6, leading to premature termination of the *ALMS1* protein initially characterised by Arsov and colleagues [340]. The deletion prevented localisation of *ALMS1* protein at the base of primary cilia, the non-motile signalling 'antennae' of transduction cascades initially reported in skeletal muscle and fibroblasts [341, 342]. Protein labelling has revealed the *ALMS1* distribution in human foetal pancreas, liver, skeletal muscle, kidney and brain: retained in alpha and beta pancreatic cells and the brain of adults [343].

Alms1 ciliary stabilisation is required for developmental Hedgehog signalling, and subsequent depletion of primary cilium function culminates in human Alström syndrome [OMIM 203800] [344]. The autosomal recessive multi-organ disorder includes severe childhood onset T2DM, obesity, shortened stature and loss of sight, hearing, and vestibular sensation [344-347].

Primary cilia of liver ito cells, pancreatic islets, and chondrocytes are implicated in human *ALMS1* mutations [348]. The *foz/foz* mutation was characterised for hypothalamic cilia of the murine brain, where full length cilia profoundly lack (-70%) adenyl cyclase 3 (AC-3) [340]. Without normal conversion of ATP to cAMP satiety and appetite were deregulated permitting obesity and diabetes in susceptible mice from 8 weeks of age [349].

Amongst gene trapped *ALMS* $1^{-/-}$ mice, only males develop diabetes, and obesity is achieved post-adolescence at 8-12 weeks of age [350]. Whilst rats bear a closer resemblance to human bone microstructure, the *Alms1* knock out retained metabolic homeostasis [351]. The focus on metabolic derangement and microstructural adaptations is justified by the finding of increased lumbar BMD in human Alström syndrome patients, which emphasised a trabecular response, greater than cortical adaptation [352]. Skeletal defects due to *ALMS1* mutations in mice have not been characterised at this time.

2.4.4.2 The NOD·B10 Strain Selection

The NOD·B10 is a 50/50 cross of the Non Obese Diabetic (NOD) mouse onto C57/BL10 (B10) background as described [353]. The NOD mouse is typically a T1DM model, however the *Alms 1 foz/foz* mutation originated spontaneously as a deletion (85537525 – 85652747 base pairs) in this strain [340]. Stabilisation by B10 out-cross enabled progeny breeding, such that NOD·B10 homozygotes exhibited the *foz/foz* mutation which can be incorporated

to other strains [354]. NOD·B10 WT mice have longevity similar to BALB/c and C57/BL6 strains exceeding 600 days [355]. Combined HF diet and genetic (*foz/foz*) stress on BALB/c background does not induce diabetes due to stable lipid storage in adipose tissue rather than liver [356].

3 Outline, Hypothesis and Aims

3.1 Outline

As discussed in the previous chapter, diabetic bone adaptations are unresolved and specific to the disease. The paradox of a higher BMD and a higher fragility and fracture disposition is not observed in obese, non-diabetic populations [357]. As diabetes onset is brought forward to a younger age, models which establish diabetes earlier, during peak mass acquisition are necessary to address the adaptations leading to orthopaedic interventions in a previously narrower age spectrum.

For this reason, younger, non-mated female mice are used to avoid aging confounders which may not apply. In this context, a focus on the more plentiful trabecular bone is justified to detect early adaptations possible prior to substantial aging, which are not distinguished by BMD alone. This project utilises the *foz/foz* model of obesity or obesity and diabetes in respective BALB/c and NOD·B10 strains to investigate the extent of early microstructural changes in the distal femur of 13 week old female mice.

3.2 Significance

Trabecular bone is comparatively immature and mobile enabling dynamic adaptations [358]. The short lifespan of osteoblasts, the surface restriction of osteocytes and the amplified physical surface area of trabecular tissue promote sensitive interactions [178]. This responsiveness is susceptible to pathological cell signalling, and irrecoverable changes in bone structure and properties as remodelling attenuates [4]. Trabecular-rich sites, such as the hip and spine are therefore implicated in impeding and established diabetes. The adaptation of trabecular tissue may be its ultimate downfall when predominant and highly responsive to the hostile T2DM environment accentuated in younger disease onset.

The paradoxical BMD in T2DM [237], the state of earlier onset T2DM and bone, and the state of younger, premenopausal femora of female mice will be considered in this project. The focus on trabecular bone microstructure complemented by biochemical probes seeks to address these critical gaps in bone quality assessment preceding fracture risk prediction. Holistic bone features contribute to an altered bone network and ultimate trade-off between fragility and utility.

3.2.1 Delimitations

The roles of osteoimmunology, endocrinology and neurology in diabetes and bone interactions are beyond the scope of this thesis. This project focuses on preliminary changes in trabecular bone investigated by bone microstructural indices and supporting biochemical data to detect early changes in younger bone tissue with diabetes onset.

3.3 Hypothesis and Aims

3.3.1 Central hypothesis

It is hypothesised early-onset T2DM has a compensatory effect on trabecular bone microstructure in explanation of equal or higher BMD to non-diabetic littermates. The younger age of mice, and early onset of diabetes in the prone group will exhibit adaptations in trabecular rather than cortical bone at this time. Diabetic mice will achieve equal or higher bone mineral density to non-diabetic groups without evidence of osteoporosis. Gene expression should support microstructural inferences of bone remodelling and osteogenic activity.

3.3.1.1 Project aims and subsidiary research questions

1. To establish the desired disease, phenotypes are represented in each strain background (BALB/c or NOD·B10); body weight, blood glucose and plasma insulin measurements will determine the allometric and metabolic status of each challenge group.

   Do strain backgrounds abide by the established model? What is the range of metabolic parameters affecting variable responses?

2. To quantify differences in bone microarchitecture of the distal femur pertaining to obesity or obesity-borne T2DM in respective BALB/c and NOD·B10 cohorts. To rule out osteoporosis at this age; and to demonstrate the equivalence of bone mineral density advocating trabecular bone consideration.

   How profound are deviations in bone microstructure amongst diabetic, obese mice from their non-diabetic littermates? Under identical treatment, does the bone microstructure of obese mice differ from their non-obese littermates?

How are these changes distinct from single challenge response(s) amongst healthy and intermediate comparators within a strain? Does either single treatment alter bone microstructure at 13 weeks of age in a given strain?

How are microstructural findings implicated with composite metabolic status?

3. To assess the extent of osteogenic gene expression variance in the diabetic cohort, contributing to the observed bone phenotypes of the NOD·B10 mouse femur. To inform a serum protein antigen selection to distinguish between diabetes susceptible groups.

   In what ways are osteogenic gene signalling expression altered in the diabetic group; how does this relate to microstructural findings?

   On the basis of systemic stress, how are diabetes susceptible groups distinguished by serum protein expression of the selected antigen?

4. Evaluation of the preliminary model in the broader discipline

   What do these findings contribute to earlier bone quality changes in T2DM?

   What are the strengths and limitations of the NOD·B10 foz/foz model? How do these affect interpretation and translation of project findings?

This thesis argues for consideration of trabecular microstructural analysis in T2DM, especially with the earlier onset of T2DM preceding peak mass acquisition. Trabecular survey could address the limitations of bone mineral density as the sole indicator of femoral bone quality, which is not representative of higher diabetic fracture risk in clinical populations.

The paradoxical bone mineral density is diabetes-specific, and not represented in obese non-diabetic bone features. Bone quality alongside bone density is integral to better characterise structural and metabolic dysregulation specific to T2DM, detected in this project in the previously unreported NOD·B10 *foz/foz* genotype.

4 Materials and Methods

4.1 Mice Regime

Mice were raised and housed at the Animal Phenomics Facility (APF) at the ANU, Canberra under 12 hour day/night light cycle in pathogen-free conditions with *ad libitum* access to autoclaved tap water. Females on NOD·B10 or BALB/c background were bred and genotyped to select wild type (WT) or *foz/foz* homozygous mutants as described [340, 359]. WT and *foz/foz* littermates of each strain were assigned to standard chow (Gordon's Specialty Feeds, NSW) or 23% kcal high fat diet (Specialty Feeds, WA) post-weaning from 4 to 13 weeks of age (Table 1).

At 12 weeks, an overnight fast (16 hours) and five day refeed was performed with final measurements obtained in fed-state at 13 weeks of age before mice were sacrificed per ethics protocol A2017/25. Fed-state body weight was measured (AE Adam, Able Scientific, Australia). Non-fasted blood glucose reading was obtained with calibrated glucometer (StatStrip Xpress™, Nova Biomedical, UK) and plasma insulin was measured by radioimmunoassay, as described [360]. As this was a preliminary study, adequate statistical group size for microstructural analysis ($n \geq 6$) was determined consulting primary literature of other younger onset obesity-borne T2DM murine models [295, 332, 361].

Table 1 Breakdown of Experimental Groups of Selected Mice

Strain	**BALB/c**				**NOD·B10**			
Genotype	WT		*foz/foz*		WT		*foz/foz*	
Diet (4-13 weeks)	Chow	HF	Chow	HF	Chow	HF	Chow	HF
Group size (*n=*)	8	6	9	6	7	7	8	8

4.2 Materials

Table 2 Electronic Equipment

Equipment name/model	Manufacturer and country of production
7900HT Realtime PCR System	Applied Biosystems, Thermo Fischer Scientific, USA
AB204 Analytical Balance	Mettler Toledo, Australia
Amersham^{tm} 680 Imager	Cytiva, Australia
Benchtop Centrifuge (5418)	Eppendorf AG, Germany
Bio-Line Platform Rocker	Edwards Instrument Co., Australia
Electronic Easypet Pipette	Eppendorf AG, Germany
Electronic S1 Pipette	Thermo Scientific, Usa
Fume Hood	Labsystems, Australia
Hettich Universal 32 Plate Centrifuge (BRF)	Zentrifugen, Germany
Magnetic Stirrer With Heating (MS-H) Pro	Bacto Laboratories, Australia
Master Cycler Ep Gradient S	Eppendorf AG, Germany
Mini Spin (5452)	Eppendorf AG, Germany
Nanodrop One Spectrophotometer	Thermo Fischer Scientific, USA
Qikspin Centrifuge (N2929)	Edwards Instrument Co., Australia
Quantstudio 12k Flex Real Time PCR	Applied Biosystems, Thermo Fischer Scientific, USA

Quantum FX System Micro-CT Scanner	Perkin Elmer, Australia
Ratek Vortex	Edwards Instrument Co., Australia
Refrigerated Centrifuge (5415c)	Eppendorf AG, Germany
Starter 3100 Bench PH Monitor	Ohaus, USA
Victor Nivo Plate Reader	Perkin Elmer, USA

Table 3 Chemical Reagents

Reagent	**Manufacturer and country of production**
Absolute Ethanol	Ajax finechem, Australia
Chloroform	Sigma-Aldrich, USA
DEPC Treated Water	Ambion, Life Technologies, USA
Distilled H_2O	JCSMR, Australia
Liquid Nitrogen	BOC Limited, Australia
Paraformaldehyde (Powder)	Chem Supply, Australia
Phosphate Buffered Saline (PBS)	JCSMR, Australia
Rnase Away	Molecular Bio Products, Sigma Aldrich, USA
Trizol LS	Ambion, Life Technologies, USA

Table 4 Molecular Products

Molecular product	**Manufacturer and country of production**
RT^2 SYBR Green ROX Mastermix	Qiagen, Australia

Table 5 Other Materials

Material	**Manufacturer and country of production**
Biopsy Histocassettes	ProSci Tech, Australia
Pathology containers	Sarstedt, Australia
BMD Phantom (2D0, 20mm diameter)	QRM MicroCT, Denmark
Aluminium foil	Confoil, AUSTRALIA
Transfer Pipette, sterile (2ml)	Sarstedt, Australia
No. 10 Carbon Steel Surgical Scalpel Blade	Swann-Morton, England
Cryopure Cryo tubes (2 ml), sterile	Sarstedt, Germany
Gammex© Surgical gloves, sterile	Ansell, Malaysia
Nitrile Soft Examination Gloves	Thermo Fischer Scientific, Malaysia
Foam Mount	Unknown, miscellaneous packaging
Parafilm Laboratory Film	American National Can, USA
Porcelain Mortar and Pestle	Staatlich, Berlin

Thermos © Insulated Flask	Thermos©, USA
Serological pipettes (5ml, 10 ml, 25 ml)	Costar, Corning, USA
0.2 ml PCR tubes	Biorad, USA
1.5 ml microtubes	Axygen, China
0.5 ml microtubes	Sasrtedt, Germany
15 ml conical tube, flat base	Corning, China
50 ml Cell Culture Flask	Beckton Dickinson, USA
RT^2 PCR Array Loading Reservoir	Qiagen, Australia
50 ml Loading Reservoir	Corning Inc., China
Kimtech Wipes	Kimberley Clarke, Australia

Table 6 Solutions

Solution	**Composition, Preparation and Storage**
4% (w/v) Paraformaldehyde (PFA) fixation solution	6 g PFA powder to 150 ml PBS heated to 60°C until completely dissolved. Stored at 4°C.
70% Ethanol (w/w), or 80% (v/v)	Absolute ethanol diluted 7 parts to 3 parts DEPC water. Prepared on demand (no storage).
RPE buffer, Qiagen©	Reconstituted with 70% ethanol

Table 7 Commercial Kits

Commercial Kit	**Supplier**
Mouse aFGF ELISA kit [EM5RB] lot [580081320]	Thermo Scientific, USA
RNEasy Mini Kit	Qiagen, Australia
RT^2 First Strand Kit	Qiagen, Australia
RT^2 Profiler Osteogenesis Mouse PCR Array [PAMM-026-Z]	Qiagen, Australia

Table 8 Computer Software

Software	**Supplier**
EndNote X8/X9	Thomson Reuters, USA
GeneGlobe© Data Analysis Centre version 2019/2020	Qiagen , USA
CT Vol©(version 2.2.3.0)	Bruker, USA
CT An© (version 1.12.8.1)	Bruker, USA
GraphPad© Prism 7.0/8.0/9.0	San Diego, USA
Caliper Analyze© version 11.0	BIR Mayo Clinic, USA

4.3 Methods

4.3.1 Sampling of Mice

After sacrifice, the femur was dissected using tweezers and No.10 blade to detach the bone and remove skin, fur and fascia with care to avoid damaging bony features. The right femur underwent paraformaldehyde (PFA) preservation immersed in same-day prepared PFA for 5 days, at 4°C, before rinse and replacement of suspension with 70% (w/w) ethanol. Stabilised samples were stored at 4°C for micro-CT scanning (Section 3.3.2). The left femur was cut into four bone chips, placed into a cryotube and snap frozen with liquid nitrogen, stored at -80°C for RNA isolation (Section 3.3.5).

4.3.2 Micro-Computed Tomography Scanning

Non-destructive micro-computed tomography (micro-CT) of the right femur was performed following fixation using the 'Quantum FX System' (Perkin Elmer, Melbourne, Australia: Caliper Life sciences, version 2.2). A given sample was air mounted in a foam insert, with the distal condyles prone to the base of the scanning bore. The stage was manually calibrated to orient samples uniformly within the scanning frame. Scanning of the distal femoral end was conducted at 90 Kvp (peak voltage), 160 µA (tube current) encompassing a 5 mm field of view for a 3 min fine scan (exposure), totalling 512 frames with 100 second integration time and voxel size 10 µm (Table 9). Data were exported as BITMAP and DICOM file formats.

Table 9 Micro-CT Scan Conditions for Femur Image Acquisition

Setting	**Value**
Peak Voltage	90 kVp
Tube Current	160 µA
Field of View	5 mm
Exposure time	3 min
Integration time	100 sec
Voxel size	10 µm

4.3.3 Micro-CT Image Region of Interest (ROI) Analysis

4.3.3.1 Image Processing of Micro-CT Scans, Trabecular Bone

BITMAP data sets were loaded into 'CT Analyser' program for binarised image processing (Bruker microCT, v 1.12.8.1). The metaphyseal growth plate was located as the imminent convergence of four distinct markings obtained for each sample (Figure 1). The individual landmark was used to standardise the area of sampling for microstructural analysis: at a range of 80 slices above the growth plate, for a total height of 100 slices. This ensured the selected ROI captured the trabecular tissue confined to the immediate metaphysis [362]. The endocortical border was manually drawn every five slices within this range to exclude cortical tissue from trabecular analysis. Pixels were binarised by global threshold to report trabecular measurements in µm. Final data were exported for analysis in Graph Pad 'Prism' 8.0 (San Diego, USA).

4.3.3.2 Image Processing of Micro-CT Scans, Cortical Bone

The cortical landmark was matched to the previous slice obtained for each sample, using the original Bitmap images (Figure 1). Cortical bone was not segmented to exclude trabecular bone, rather the image background was removed from the entire bone object. ROIs were processed as described above. Final data were exported to GraphPad 'Prism' 8.0 for statistical analysis (San Diego, USA).

4.3.3.3 Three Dimensional Reconstruction of Median Scan Representatives

The three dimensional (3D) representations of the trabecular segment selected above (Section 3.3.3.1) were produced by launching processed trabecular ROI images in 'CT Analyser', and thresholding the binarised image between 80 to 100 grayscale intensity units. The resultant P3G images were opened in 'CT Vol' (Bruker microCT, v2.2.3.0), cropped from the image background and saved (Figure 1). Images were not resized. The median animal of each group was selected (whereby 2 images were in agreement, and the third did not concur, one of the two was selected).

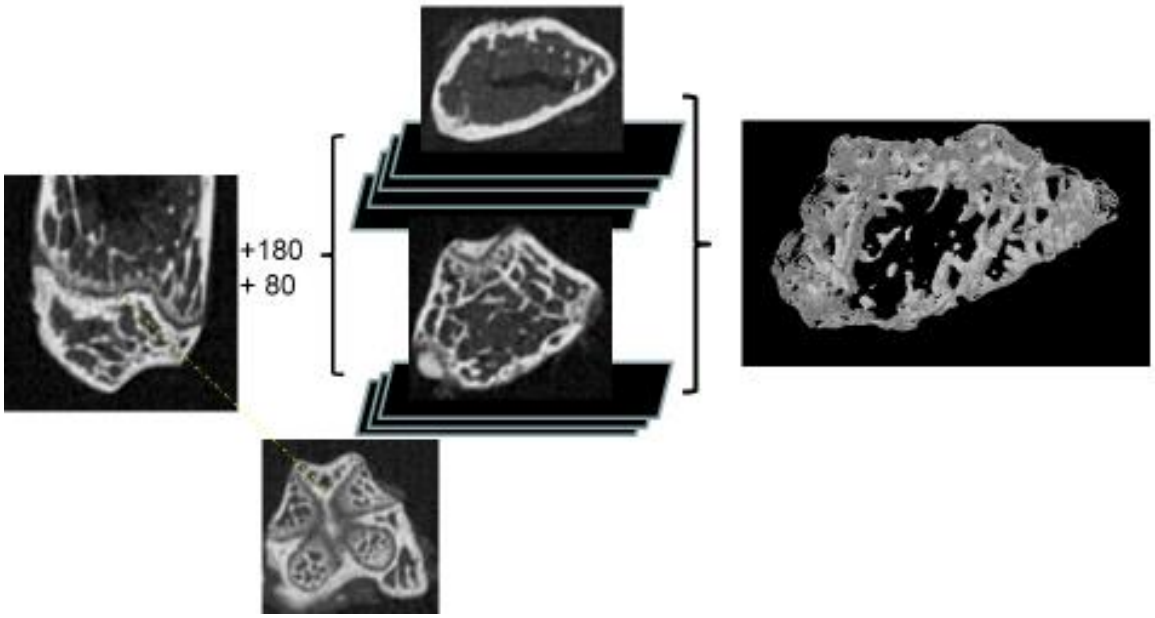

Figure 1 Workflow for Acquiring the Region of Interest of the Distal Femur to 3D Reconstruction of the Desired Sample Space

From raw CT images totalling 512 slices of the distal femur, the growth plate was located as the convergence of four points (approximated by yellow line) on transverse section. From this landmark slice the sample space was offset 80 slices, to a total height 180 slices above the growth plate encompassing the trabecular region. A 3D reconstruction was performed on the binarised volume of interest generated from transverse section integration. Cartoon not to scale.

4.3.4 BMD Calibration

4.3.4.1 BMD Phantom Value Acquisition

A BMD Phantom (QRM MicroCT 2D0, 20 mm diameter) containing five rods of hydroxyapatite (densities 0, 50, 200, 800 and 1200 mg HA/cm^3) was subject to air micro-CT scanning at the same conditions as the experimental samples using the Perkin Elmer 'Quantum FX' machine (see Table 1). Images were exported as BITMAP and DICOM files, whereby DICOM images were imported to 'Caliper Analyze'© software (version 11.0, BIR Mayo Clinic, USA). A 3D volume of the 512 composite images was constructed for analysis to generate a calibration curve for establishing bone mineral density of each sample (per Analyze instruction manual). The scatterplot of the 5 densities generated a calibration curve with linear regression trend line equation (*y=5.4774x+1566.3*, R^2 = 0.9999). To determine BMD conversion from mean grayscale intensity, the above equation was manipulated to [BMD=(input-intercept)/slope].

$$BMD\ (mg\ HA/cm^3) = (input - 1566.3)/5.4774$$

4.3.4.2 Image Processing and Analysis

Raw DICOM image datasets (512 images per sample) were uploaded to 'Analyzer'©, and volume construction performed on import. The bone volume was segmented from the background, with a constant minimum threshold of 297 grayscale units, whilst the maximum was raised as high as possible for each sample, without oversaturating the image. Processing of the object against the calibration curve equation reported the resultant volumetric BMD in milligrams of hydroxyapatite per cm^3. Final data were exported to GraphPad 'Prism' 8.0 (San Diego, USA) for statistical analysis.

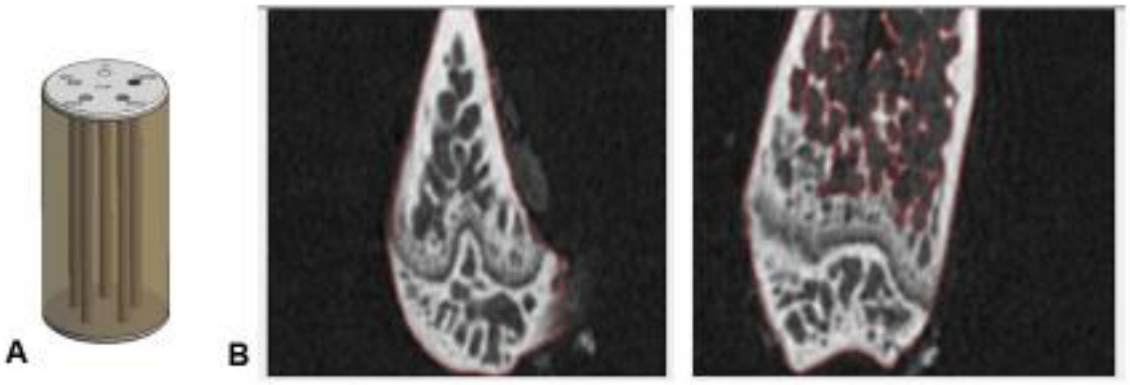

Figure 2 Volumetric Bone Mineral Density Calibration of Distal Femur from Micro-CT Scanning Images

(A) BMD phantom of known hydroxyapatite density inserts used to generate a calibration curve in 'Analyzer'© software. (B) Bone segmentation outlined in red of the compiled volume from micro-CT reconstruction for interpolation of the grayscale intensity converted to hydroxyapatite content of volumetric BMD.

4.3.5 RNA Preparation

4.3.5.1 Total RNA Extraction

Bone gene expression was determined from processing of the whole femur including bone marrow adipose tissue. The left hindlimbs of all mice were collected at 13 weeks of age by dissection after euthanasia. The femur was cut into 4 bone chips placed into cryotubes exposed to liquid nitrogen, snap frozen and stored at -80°C. Bone chips were macerated under liquid nitrogen in mortar and pestle until finely ground. Powdered bone was collected in the cryotube and exposed to 1 ml of TriZol reagent for 10 mins at room temperature, optimised by brief vortex.

Eppendorf tubes (1.5 ml) were prepared with 200 ml of chloroform to which the Trizol suspension (1 ml) was added. Contents were mixed by vigorous shaking for 15 sec and held at room temperature for 3 mins. The solution was then centrifuged at 12,000 x g for 15 mins at 4°C (5415C, Eppendorf AG, Germany). Seventy percent ethanol was produced by diluting absolute ethanol with DEPC water (7:10) whilst samples were centrifuged.

The colourless, upper layer of sample tubes was transferred as 400 µl draw and 50 µl draw into a new micro-centrifuge tube, avoiding contamination with the undesired lower pink layer. The 70% ethanol solution was added to a matching volume of mRNA elute to the centrifuge tubes and contents were shaken vigorously to resuspend precipitates. A 700 µl aliquot of sample was pipetted into RNEasy mini spin column (Qiagen, Australia) atop a 2 ml collection tube. Contents were centrifuged at 10,000 rpm for 15 sec at room temperature (5418, Eppendorf AG, Germany) and flow through discarded. Further 700 µl aliquots and process were repeated for remaining volume and accompanying precipitates.

After removal of unbound material, further refinement of silica membrane bound contents occurred according to the manufacturer's instructions (RNeasy mini kit, Qiagen, Australia). Next 350 µl of proprietary buffer RW1 was added to the column, and spun down at 10,000 rpm for 15 sec, with flow through discarded. Separately, 10 µl of DNAse I stock solution was added to 70 µl proprietary RDD buffer (per sample) and combined by gentle inversion. Then 80 µl of DNAse I-RDD solution was pipetted onto the membrane and incubated at room temperature for 15 mins. An additional 350 µl of proprietary RW1 buffer was added to the column and centrifuged at 10,000 rpm for 15 sec, discarding flow through.

The spin column was transferred to a new collection tube, with addition of 500 µl proprietary RPE buffer, centrifuged at 10,000 rpm for 15 secs, discarding flow through. Another 500 µl

of RPE buffer was added to the membrane, and centrifuged at 10,000 rpm for two mins to dry the membrane. The mini spin tube was inserted to a new collection tube spun at 12,000 rpm for 2 mins to remove final wash contaminants. The spin column was placed into an RNAse-free collection tube, with addition of 50 µl RNase free water to the column membrane, held for one minute at room temperature. The final solution was centrifuged at 10,000 rpm for 1 minute to collect RNA elute.

RNA concentration and purity was determined by the Nanodrop One spectrophotometer instrument (Thermo Fischer scientific, USA). Readings were calibrated by 2 µl aliquot to ddH_2O. The threshold for RNA integrity was set at 2.0 for A260/A280 ratio, with secondary threshold of 1.8 for A260/A230 ratio of nucleic acid content. The final concentration of RNA (ng/µl) was recorded for cDNA conversion below. RNA was stored at -80°C prior to cDNA synthesis, or immediately converted to cDNA (Section 4.8).

4.3.5.2 Complementary DNA Synthesis

Isolated total RNA was reverse transcribed to complementary single strand DNA (cDNA) for quantitative PCR of the mRNA surrogate. A uniform quantity of 1 µg of isolated RNA was calculated from Nanodrop concentration yield in ng/µl.

RT^2 first strand kit reagents were stored and prepared according to the manufacturer's instructions (Qiagen, Australia). On ice, standardised RNA was mixed with 2 µl of Buffer GE and calculated volume of water to final volume of 10 µl (Table 10). The reaction mix was incubated for 5 mins at 42°C (Master cycler ep gradient S, Eppendorf AG, Germany) and instantly cooled for 60 sec to halt the reaction.

Table 10 Qiagen Genomic DNA Exclusion Mixture Preparation

Reagent	**Quantity**
Buffer GE	2 µl
Isolated RNA	1 µg (varied volume)
RNAse free water	varied
Total volume	10 µl

RNA was transcribed to cDNA by according to the manufacturer's directions (Qiagen, Australia) (Table 11).

Table 11 Qiagen Reverse Transcription Master Mix Preparation

Reagent	**Volume for 1 reaction (µl)**	**Volume for 4 reactions* (µl)** **(*to slight excess)**
5x buffer BC3	4	16.4
Control P2	1	4.1
RE3 Reverse transcriptase mix	2	8.2
RNA-se free water	3	12.3
Total volume	10	44

Ten µl of the reverse transcription mixture was added to each genomic DNA-eliminated RNA sample following incubation, and incorporated by gentle pipette mixing. The complete mix was incubated at 42°C for 15 mins (Master cycler ep gradient S, Eppendorf AG, Germany) to bind oligonucleotides and generate the desired complementary DNA single strand. The reaction was halted by incubation at 95°C for 5 mins. Finally 91 µl of RNAse free water was added to each sample and mixed by repeated pipetting. Samples were stored at -80°C until PCR.

4.3.6 Osteogenesis Pathway Signalling Determined by RT-qPCR Array

To determine the osteogenic gene expression profile of NOD·B10 mice, real-time quantitative PCR array (RT-qPCR) of 84 genes of interest was performed following the manufacturer's protocol (PAMM-026Z, Qiagen, Australia). SYBR green ROX mastermix was centrifuged to pull contents to base of tube out of direct light (Qiagen, Australia). The PCR reaction mix was prepared (Table 12). A multi-channel pipette was used to load wells with 10 µl the PCR mix per manufacturer's configuration (Qiagen, Australia). Each plate was prepared separately with four replicates of a single group.

Table 12 Qiagen PCR Component Mixture Preparation

Reagent	**Volume for 384 wells (4x96 format)**
RT^2 SYBR Green mastermix	650 µl
cDNA synthesis reaction	102 µl
RNA-se free water	548 µl
Total master mix volume	1300* µl (*deliberate excess 340 µl)

Each plate was sealed with the plate covering and centrifuged at 1500 rpm for 2 mins before running on PCR thermal cyclers (7900HT real time PCR system, Applied Biosystems, USA; Quantstudio 12k flex real time PCR instrument, Applied Biosystems, USA) in a two-step cycle protocol (Table 13) per the manufacturer's instructions (Qiagen, Australia). The manual threshold was uniform across each plate.

Table 13 Qiagen PCR System Protocol

Stage	**Configuration**	**Cycle(s)**
Holding	95°C (10 mins)	1
Denaturation Annealing	95°C (15 sec) 60°C (1 mins)	 40
Melt curve	95°C (15 sec) 60°C (1 mins) 95°C (15 sec)	continuous

4.3.6.1 RT-qPCR Analysis

C_T values from the real time PCR were collected using SDS software package (SABiosciences). The melt curve of each plate was checked for primer specificity. Genes of interest were normalised to housekeeping gene (*Gusb)* for relative fold expression (fold change) calculated using Livak's equation ($2^{-\Delta\Delta C_T}$) in Gene Globe© software (Qiagen, USA) [363]. Fold regulation was used to convert under-expressed genes more readily.

$$Fold\ change = 2^{-\Delta\Delta C_T}$$

$$Fold\ regulation = (2^{-\Delta\Delta C_T})^{-1}$$

$$\Delta C_T = C_T(gene\ of\ interest) - C_T(housekeeping\ gene).$$

$$\Delta\Delta C_T = \Delta C_T(gene\ of\ interest\ experimental\ group) - \Delta C_T(gene\ of\ interest\ experimental\ control)$$

The gene expression results for each experimental group are expressed relative to chow-WT mice.

4.3.7 Fibroblast Growth Factor 1 Enzyme Linked Immunosorbent Assay

FGF1 (aFGF) levels were measured using the ThermoScientific ™ Pierce ™ pre-coated Mouse aFGF Enzyme Linked Immunosorbent assay (ELISA) kit in 96 well plate format. The assay was sensitive to 12 pg/ml, with intra-assay coefficient of variation <10%, and inter-assay coefficient of variation <12%.

4.3.7.1 Serum Sample Preparation

At time of sacrifice, 200 µl aliquots of serum from cardiac puncture were collected and stored at -80°C. Samples were thawed and spun at 1,000 x g for 10 mins at 4°C to bring cells to the bottom of the tube. Samples were then allowed to return to room temperature. Serum aliquots were undiluted (neat), or diluted to 1:2 and 1:4 working solutions to a final volume of 100 µl per well, prepared in duplicate.

4.3.7.2 Reagent Preparation

Concentrated assay diluent was diluted to 1:5 working solution with distilled water (dH_2O). The 20x Wash buffer concentrate was diluted to 1:20 working solution with dH_2O. The biotin-conjugated secondary antibody was diluted to 1:80 working solution with 1x assay

diluent. The HRP-Streptavidin solution was diluted to 1:300 working solution with 1x assay diluent.

4.3.7.3 Standard Preparation

The standard was briefly spun to resuspend contents (minipsin, Eppendorf). Next, 400 µl of 1x assay diluent was added and allowed to stand for 10 min to reconstitute the protein with gentle mixing. Meanwhile, 300 µl of 1x assay diluent was added to seven 1.5 ml centrifuge tubes. Thirty µl of the resulting 50 ng/ml standard solution was transferred to a 1.5 ml Eppendorf tube containing 470 µl of 1x assay diluent and thoroughly incorporated by pipette to yield a 3,000 pg/ml stock solution.

Then 200 µl of this stock was transferred to the next tube, containing 300 µl of assay diluent. A serial dilution series was made, with transfer of 200 µl aliquot to sequential tubes, with thorough mixing and a new pipette tip each time. The seventh transfer of 200 µl of serial diluted protein was discarded, leaving the eighth tube as a blank containing only 300 µl of assay diluent (0 pg/ml). All tubes contained a final volume of 300 µl with known protein concentrations.

4.3.7.4 ELISA Performance

The desired kit contents were thawed and brought to room temperature. Next 100 µl of standard working solutions (3,000-0 pg/ml) and sample working solutions (neat, 1:2, or 1:4) were pipetted into the pre-coated plate in duplicate. The plate was covered with aluminium foil and incubated at room temperature (RT) for 2.5 hours with gentle shaking (Bioline platform rocker, Edwards Instrument Co., Australia).

After the elapsed incubation, the plate was washed four times with 150 µl volumes of 1x wash buffer using a multi-channel pipette to prevent over-binding. The plate was inverted to discard the undesired unbound material between washes, and the plate was blotted dry with paper towel after the fourth rinse. Care was taken to avoid drying of the plate.

Then 100 µl of 1:80 Biotinylated secondary antibody was added to each well using a multi-channel pipette. The plate was covered in aluminium foil and incubated at room temperature for 1 hour with gentle shaking (Bioline platform rocker, Edwards Instrument Co., Australia). The plate was rinsed as described above.

Next 100 µl of 1:300 Streptavidin-HRP solution was added to each well using a multi-channel pipette to label the bound product. The plate was covered with aluminium foil and incubated at RT for 45 mins with gentle shaking. The plate was rinsed as described above to remove unbound material.

In a dimmed room, 100 µl of TMB substrate was added to each well using a multi-channel pipette to convert the chromogenic label. The plate was covered with aluminium foil and developed at RT for 30 mins with gentle shaking in the dark (Bioline platform rocker, Edwards Instrument Co., Australia).

After the incubation time, 50 µl of stop solution was added to each well to simultaneously halt the reaction. The plate was analysed on the Victor Nivo (Perkin Elmer, USA) at 450 nm and 550 nm wavelengths, at 39.5°C with 250 ms exposure to measure optical density of the 64 well plate.

Kit reagents were stored at 4°C per the manufacturer's instructions for later use. The unused well strips were kept at -20°C until later use. The protocol was repeated with the remaining 32 wells, with the plate reading taken at 24.2°C.

4.3.7.5 Results Equation for Antigen Determination

Data were collected and processed according to the following. The 550 nm readings were subtracted from 450 nm readings to correct for microplate deviations in the density measurement. The background absorbance was obtained and averaged across blank (0 pg/ml) wells. This value was subtracted from the reading for each well. Adjusted results were imported to GraphPad 'Prism' 9 software, entered as X values for the known (standard) protein concentrations; and Y values as duplicate absorbance readings for each sample. The "interpolate standard curve" function was applied, selecting the sigmoidal 4 parameter logistic (4PL) curve, ensuring X values were concentration units. Unknown concentrations of the experimental samples were interpolated from the standard curve by the software (Figure 3A). A separate standard curve and equation were generated for the second experiment (Figure 3B).

$$y = \text{bottom} + [(x^{\text{hillslope}}) * (\text{top-bottom})/(x^{\text{hillslope}} + EC50^{\text{hillslope}})]$$

Where y is absorbance, x is concentration

i) 64-well standard curve equation $y=0.00097+ [(x^{1.025}) * (2.33-0.00097)/(x^{1.025} +1660^{1.025})$

ii) 32-well standard curve equation $y=0.01972 + [(x^{1.573}) * (2.127-0.01972)/(x^{1.573} + 846.9^{1.573})]$

Interpolated values were multiplied by respective dilution factor to give final concentrations of FGF1 measured in the assay expressed in pg/ml.

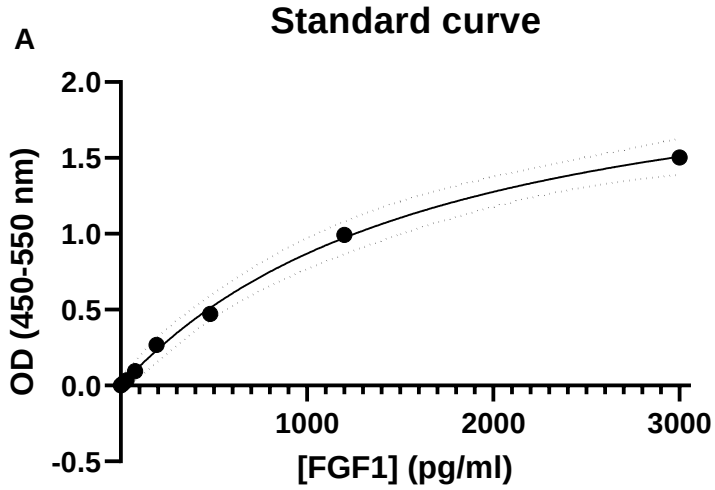

R squared	0.9833
Adjusted R squared	0.9792

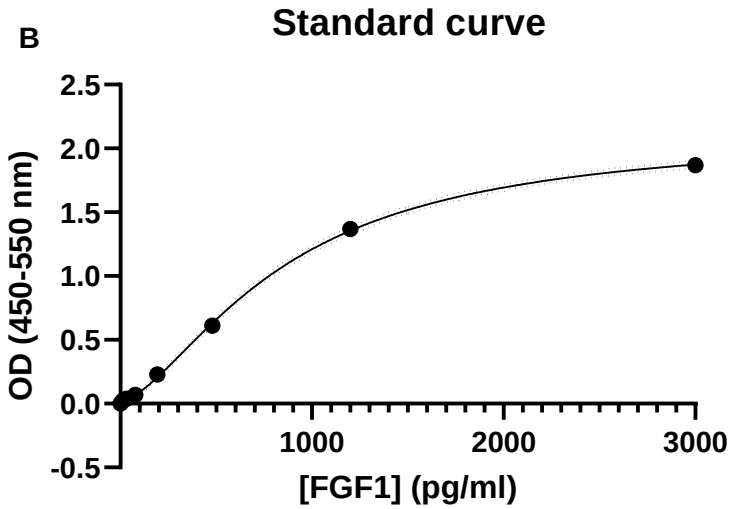

R squared	0.9993
Adjusted R squared	0.9991

Figure 3 Standard Curves of Known FGF1 Concentrations.

(A) Generated from 64-well assay (B) Generated from 32-well assay.

4.4 Statistical Analysis

Values are presented as box plots of minimum to maximum values with median, unless stipulated as 95% confidence interval. Data were imported to 'Prism' software package and checked for normality violations by the Shapiro-Wilk test with less than 10 observations per group. Outliers were removed using the 1.5 interquartile range rule. Data were transformed to log (base 2) distributions as necessary to satisfy analysis of variance (ANOVA) assumptions.

Successfully normalised data were analysed by multiple comparisons for the main effects of strain, genotype and diet. A preliminary 3-way ANOVA was used to detect interactions of the three variable combinations. Follow up 2-way ANOVA was performed, with Sidak's correction for multiple comparisons. Significance was set to 0.05 with a 95% confidence interval. Data which could not be transformed to a normal distribution were analysed by Mann-Whitney rank of unpaired, non-parametric t-test. Values were ranked indiscriminately then assigned to groups for mean rank assessment, further adjusting for tied positions to sum of ranks comparison (GraphPad© Prism, 8.4.2).

Gene expression data was analysed by software upload to the Qiagen© database (http://www.qiagen.com/geneglobe). Data were normalised by manual selection of the lowest arithmetic mean reference gene and 2-tailed t-test was performed between control and experimental groups. Relative to the control group, results are presented as mean over 95% confidence interval, with alpha set to 0.05.

4.5 Reproducibility

To ensure scientific rigour of the findings, at least two operators performed the sampling and processing workflows, except the PCR array and ELISA. Other operators were blind to the mouse identities and treatment groups.

5 Confirmation of Disease Phenotypes by Mouse Strain

5.1 Introduction

Prior to characterising bone microstructure, disease phenotypes must be confirmed in each strain. Disease progression must be contextually defined when interpreting findings in a chronic and progressive condition such as T2DM or obesity. No rodent or murine model can recapitulate spontaneous obesity-borne T2DM after skeletal maturity [176]. Furthermore, life staging is not directly scalable between humans and mice [364, 365]. Thus comprehensive animal models are necessary to develop mechanistic inquiry.

Younger mice were used to detect urgent disruptions to bone remodelling coinciding with earlier disease acquisitions. Female mice were utilised for improved indication of low turnover, and slower disease onset than previous metabolic bone research. This sensitivity would detect significant bone downturn otherwise masked by using male mice. The end point was considered at 3 months of age, approximating the peak of growth from the similar longevity of C57/BL6J mice [177, 355]. This earlier end point precedes substantial aging, to account for the rapidity of potential bone remodelling coinciding with metabolic changes in younger bone.

At the expense of carbohydrates, HFD is a vehicle for accelerating metabolic derangement. Fat content can range from 20-60% kcal and best recapitulates human metabolic disease aetiology [176]. The hypothalamus is especially vulnerable to hyperphagia exacerbated by HFD causing metabolic inflammation [366, 367]. The *foz/foz* mice achieve obesity by 120 days of age on chow feed due to hypothalamic ciliopathy [340]. The mutation is exploited with high fat feeding conducive to earlier hypothalamic deregulation catalysing diabetes and obesity onset.

Rodent models differ from human metabolism, requiring comparatively supra-physiological stimuli to elicit responses, owing to rapidity of metabolite processing afforded of small body size and two year lifespan [368]. Animal diabetes models lack unanimous criteria for pre- and established disease, unlike human diagnostic criteria. In addition to hyperinsulinemia indicating insulin resistance, mice exhibiting non-fasted blood glucose level exceeding 8 mM (mmol/L) are considered diabetic. This value was determined from the previous work of Dagpo and colleagues, who performed serial sampling of the *foz/foz* mice to demonstrate the impaired glucose tolerance of diabetes-susceptible HF-fed NOD·B10 mice [353].

5.2 Disease Phenotype Results

5.2.1 NOD·B10 *foz/foz* Mice Achieved Diabetes and Obesity with 9 Week HFD

To determine the allometric response to dietary fat content and genetic stress, fed-state body weight was measured. NOD·B10 *foz/foz* mice were overweight on chow feed (36.64 ± 6.21 g), and obese on high fat feed (53.29 ± 4.92 g) (Figure 5). The considerable increase in fed-state body weight was not apparent in the healthy WT mice which could not be differentiated by diet regime. Notably, chow-*foz/foz* mice were not distinguished from HF-WT (30.41 ± 5.78 g) mice, yet were heavier than chow-WT (26.83 ± 3.53 g). Amongst *foz/foz* mutants, HF-fed mice with combined diet and genetic stress achieved the heaviest body weight compared to all other experimental groups, consistent with obesity (Figure 4).

To confirm the circulating insulin response of each group, plasma insulin concentration was detected (Figure 6). The plasma insulin concentration of *foz/foz* mice was significantly elevated in contrast to the WT mice. The overweight and obese mutant groups achieved similar hyperinsulinemia upon 9 week feeding regime independent of diet assignment (chow-*foz/foz*: 14.52 ± 17.15 ng/ml; HF-*foz/foz*: 27.17 ± 17.55 ng/ml).

To confirm the diabetic state of the desired experimental group, blood glucose concentration was obtained (Figure 7). HF-*foz/foz* mice achieved overt hyperglycaemia by this protocol (13.95 ± 5.41 mM) in contrast to the other experimental groups. This finding differentiates the HF-*foz/foz* mice from the chow-*foz/foz* mice as diabetic, rather than in a pre-diabetic and/or insulin resistant state considering the similarity in hyperinsulinemia. Together, measures of body weight, plasma insulin concentration and blood glucose concentration support previous diagnoses of murine T2DM. This confirms the validity of the female NOD·B10 *foz/foz* mice as obese and diabetic when fed a 23% kcal diet from 4 to 13 weeks of age.

5.2.2 BALB/c *foz/foz* Mice Achieved Obesity without Diabetes on 9 Week HFD

To confirm the weight gain response to dietary fat content and genetic stress, fed-state body weight was measured. BALB/c *foz/foz* mice were overweight on chow feed (36.24 ± 4.84 g), and obese on high fat feed (51.26 ± 5.45 g) (Figure 5). This considerable increase in fed-state body weight was not apparent in the healthy WT mice which could not be differentiated by diet regime (chow-WT: 22.62 ± 2.04 g; HF-WT: 27.41 ± 2.87 g). Amongst *foz/foz* mutants, HF-fed mice achieved the heaviest body weight compared to all other experimental groups, with combined diet and genetic stress.

To measure the circulating insulin response of each group, plasma insulin concentration was detected (Figure 6). The plasma insulin concentration of *foz/foz* mice was significantly elevated in contrast to the WT mice. The obese mutant group achieved the highest plasma insulin levels (3.75 ± 2.42 ng/ml), relative to single treatment groups. Chow-*foz/foz* mice also achieved higher insulin than WT mice (1.51 ± 0.82 ng/ml), however were not significantly discriminated from the HF-WT group.

To confirm the absence of diabetes across the BALB/c strain blood glucose concentration was obtained (Figure 7). All experimental groups were euglycaemic without substantial variation (For example, HF-*foz/foz*: 6.90 ± 0.43 mM). Together, the heavier body weight, elevated insulin status and euglycaemia of HF-*foz/foz* mice confirm the BALB/c cohort are obese but resistant to diabetes when fed a 23% fat kcal diet from 4 to 13 weeks of age (Figure 4).

5.2.3 Strain Effect Underscored Disposition and Resilience to Diabetes

BALB/c and NOD·B10 mice achieved matched body weight by treatment groups, whereby the strain effect was not significant (*p=0.0558*, 3-way ANOVA). Body weight response to diet and genotype had a significant interaction (*p<0.0001*, 3-way ANOVA) which persisted within each strain (BALB/c, *p=0.0025*; NOD·B10 *p=0.0022*, both 2-way ANOVAs). Mice fed HF feed were heavier than chow-fed counterparts; and heaviest when combined with the *foz/foz* mutation. Therefore, by treatment groups, mice of either strain background measured similar body weight at 13 weeks of age exerting similar mass effects on bone.

The strain divergence in metabolic response was evident by plasma insulin levels, as strain was a significant interaction with genotype (*p=0.0009*, 3-way ANOVA). NOD·B10 *foz/foz* plasma insulin levels were significantly higher than BALB/c mutants (*p<0.0001*, 2-way ANOVA) highlighting the endemic difference in background metabolic susceptibility. Therefore the NOD·B10 HF-*foz/foz* group achieved marked hyperinsulinemia at 13 weeks of age, which was not reflected in the metabolically protected BALB/c littermates under identical assignments.

When establishing diabetes against 8 mM blood glucose criteria, only NOD·B10 HF-*foz/foz* mice exceeded this threshold. Strain, diet and genotype variables all interacted significantly (*p=0.0023*, 3-way ANOVA) highlighting the susceptibility of this group to the combined treatment stress, and apparent hyperglycaemia. Therefore, the NOD·B10 HF-*foz/foz* mice demonstrated markedly impaired glucose tolerance to all other experimental groups,

consistent with type 2 diabetes. Based on these findings, within-strain comparisons are presented in figures to provide meaningful comparisons in each strain background.

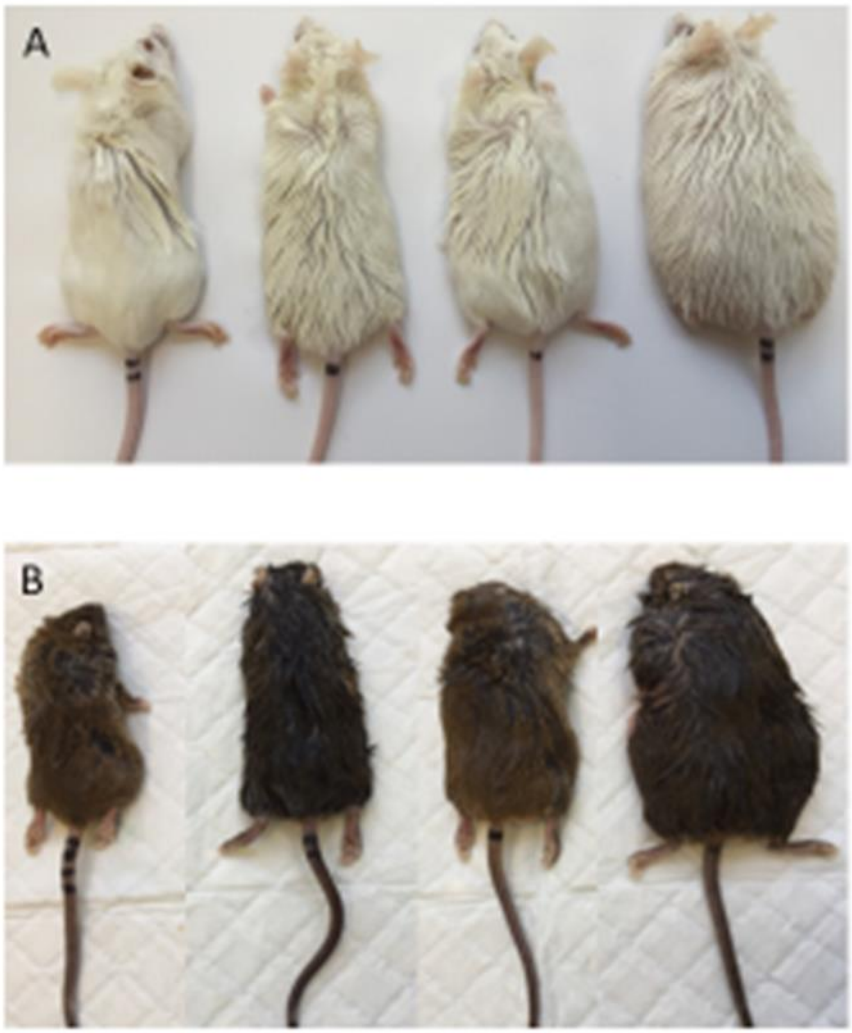

Figure 4 Desired Phenotypes of Female Mice on Each Background Were Achieved at 13 Weeks of Age by Treatment Assignments

(A) BALB/c (B) NOD·B10. From left to right: chow-WT, HF-WT, chow-*foz/foz*, HF-*foz/foz.* Mice on HFD had an oily sheen to their fur. HF-*foz/foz* mice on either background with combined diet and genetic stress were markedly obese.

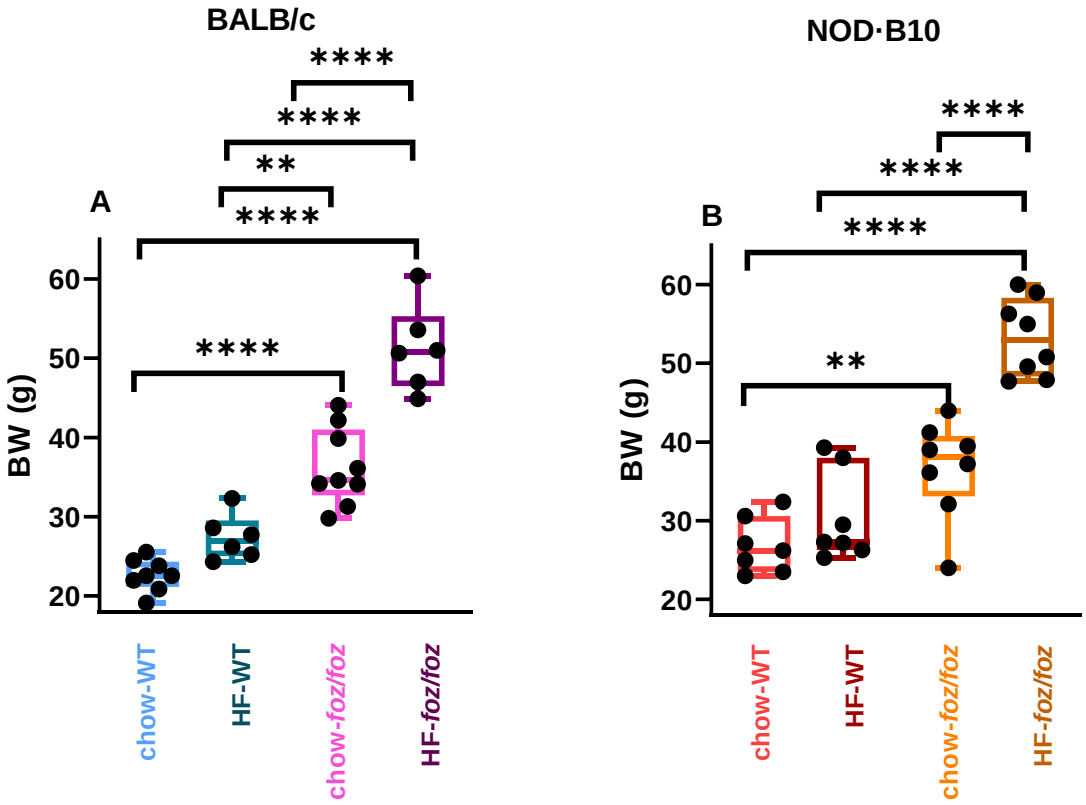

Figure 5 Effect of Diet and Genetic Challenge(s) On Female Fed-State Body Weight at 13 Weeks of Age

(A) BALB/c HF-*foz/foz* mice achieved obesity at 13 weeks of age (*n=6-9/group*). Significance determined by 2-way ANOVA (interaction effect *p=0.0025*) with Sidak's adjustment for multiple comparisons. (B) NOD·B10 HF-*foz/foz* mice achieved obesity at 13 weeks of age (*n=7-8/group*). Significance determined by 2-way ANOVA (interaction effect *p=0.0022*) with Sidak's adjustment for multiple comparisons. Values presented as min to max, all values plotted,**p<0.05, **p<0.01, ***p<0.001, ****p<0.0001*. 'BW' body weight, as expressed by grams (g).

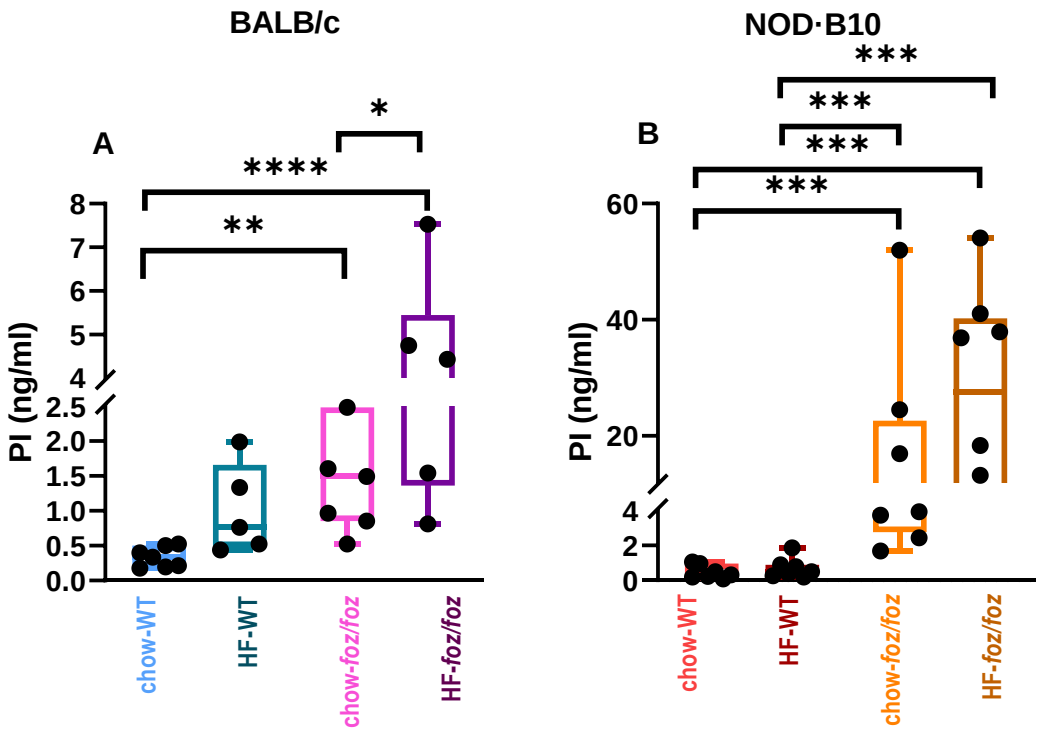

Figure 6 Effect of Diet and Genetic Challenge(s) On Female Plasma Insulin Concentration at 13 Weeks of Age

(A) HF-*foz/foz* BALB/c mice achieved mild hyperinsulinemia compared with non-obese littermates (*n=6-9/group*). Significance determined by 2-way ANOVA (mutation effect *p<0.0001*; diet effect *p=0.0016*) with Sidak's adjustment for multiple comparisons. (B) *foz/foz* mice on NOD·B10 background achieved marked hyperinsulinemia by chow and HFD (*n=7-8/group*). Significance determined by 2-way ANOVA (mutation effect *p<0.0001*) with Sidak's adjustment for multiple comparisons. Values presented as min to max, all data plotted.**p<0.05, **p<0.01, ***p<0.001, ****p<0.0001*. 'PI' plasma insulin concentration, as expressed by nanograms per millilitre (ng/ml).

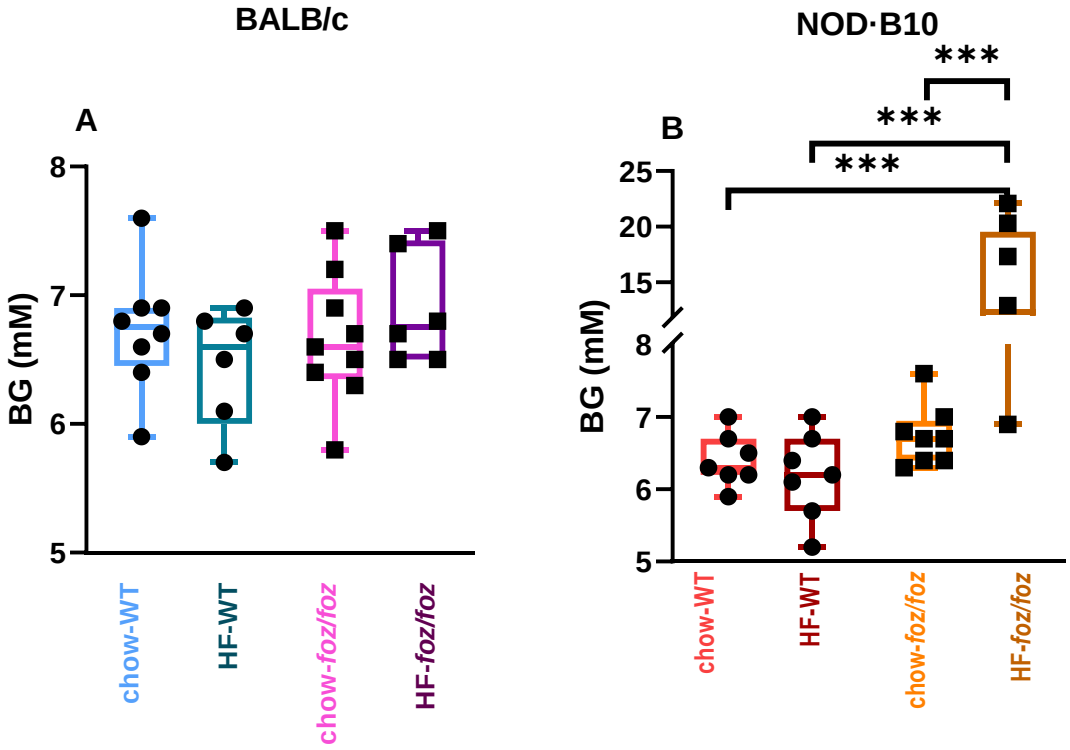

Figure 7 Effect of Diet and Genetic Challenge(s) On Female Fed-State Blood Glucose Concentration at 13 Weeks of Age

(A) HF-*foz/foz* BALB/c mice were euglycaemic and resembled non-obese littermates (*n=6-9/group*). Significance determined by 2-way ANOVA with Sidak's adjustment for multiple comparisons (*p>0.05*). (B) HF-*foz/foz* NOD·B10 mice were hyperglycaemic compared to non-diabetic littermates (*n=7-8/group*). Significance determined by Mann-Whitney U test. Values presented as min to max, all data plotted. **p<0.05, **p<0.01, ***p<0.001, ****p<0.0001*; 'BG' blood glucose concentration, as expressed by mM (mmol/L).

5.3 Discussion of Disease Phenotypes

5.3.1 Female NOD·B10 Mice Were Obese and Diabetic By Combined Diet and Genetic Challenge

HF-*foz/foz* NOD·B10 mice achieved diabetes and obesity at 13 weeks of age in accordance with the established model [340, 353]. HF-*foz/foz* mice were heaviest, with marked hyperinsulinemia and hyperglycaemia compared to the remaining NOD·B10 cohort. Chow-WT mice served as a healthy, lean comparator group corroborated with invariant blood glucose and plasma insulin levels to HF-WT mice. Chow-*foz/foz* mice reported higher body weight and plasma insulin to chow-WT mice, which implicated mutation stress with standard diet.

As a positive control for diet, HF-WT mice had lower body weight, plasma insulin and blood glucose than HF-*foz/foz* mice, and resembled the chow-WT cohort. The mutation effect drove increase in body weight, whilst only the HF-*foz/foz* mice exceed 8 mM criterion for diabetic glycaemia. Taken together, these data indicated that the NOD·B10 metabolic susceptibility to diabetes was driven by *foz/foz* mutation and exacerbated by HFD in agreement with the literature.

The mutation effect observed in NOD·B10 mice may originate from the *Alms1 (foz/foz)* hypothalamic ciliary defect by onset of hyperphagia from day 30, and a tendency to consume more feed *ad libitum* than WT mice [340]. Furthermore, with modest carbohydrate substitution hyperphagic animals may have partially mitigated diet stress by consuming more total feed. The stress of HFD alone did not reveal profound differences in WT cohorts, with equivalent body weight, plasma insulin and blood glucose measurements.

The *foz/foz* mutation could include other ciliary defects, leading to exaggerated experimental response in support of the statistically significant mutation effect. Under a matched feed study, NOD·B10 *foz/foz* mutants achieved greater lipid uptake and subsequent obesity to WT mice, proposed as an intestinal ciliopathy added to the hypothalamic defect [369]. Similar to the *foz/foz* mouse, the *Alms1* gene trapped mouse model achieved obesity attributed to GLUT-4 impairment, which facilitated adipose expansion [370]. More research is needed to investigate the potential of other ciliopathies contributing to obesity-associated T2DM by 13 weeks of age in HF-*foz/foz* NOD·B10 mice.

5.3.2 Female BALB/c Mice Were Diabetes Resistant Despite Combined Challenge Obesity

HF-*foz/foz* BALB/c mice achieved obesity and mildly elevated plasma insulin concentration compared to the single treatment groups. Across the BALB/c cohort, there was a trend of increasing body weights and slight increases in plasma insulin which indicated metabolic sensitivity to diet and/or mutation assignments. Chow-*foz/foz* mice achieved higher body weight and plasma insulin than HF-WT mice indicative of mutation-driven stress. All mice were euglycaemic in accordance with the prior established model. Taken together, this confirmed the BALB/c resistance to developing T2DM upon this regime, instead achieving healthy obesity by combined HFD and *foz/foz* mutation.

A moderate increase in plasma insulin concentrations was detected for the combined treatment group, verified by the established model [353]. BALB/c mice maintained euglycaemia across treatment groups as expected, with superior glucose tolerance by preserved insulin sensitivity. The BALB/c strain has demonstrated hepatic protection with lower lipid accumulation despite HFD, defining the atypical diabetes resistance strategy [356]. In explanation, Farrell and colleagues found highest serum triglycerides for BALB/c compared with NOD·B10 and C57/BL6 strains, attributed to the compensatory lipid detour to adipose [359].

5.3.3 Further Discussion

HF-*foz/foz* NOD·B10 mice developed obesity and T2DM by 13 weeks of age, unlike BALB/c mice which achieved obesity under identical regime. Equal blood glucose was reflected in all cases except the diabetic NOD·B10 HF-*foz/foz* group which also exhibited obesity and marked hyperinsulinemia.

The variation in plasma insulin was markedly higher in the NOD·B10 strain. Thus direct inter-strain comparisons are not made hereafter to avoid over-representation of the single diabetic cohort of HF-*foz/foz* NOD·B10 mice. The spectrum of healthy to obese sub-groups within each strain was investigated to address how trabecular bone is altered by younger onset T2DM in the NOD·B10 mice, separate to sole obesity effects on bone as represented by BALB/c mice.

The metabolic differentiation at 13 weeks of age supported the sensitivity of the study model coinciding with murine skeletal maturity. In contrast, a study using male TallyHo mice as diabetic obese strain, compared with SWR control strain could not discern metabolic nor microstructural differences between 20% kcal HFD-sucrose and chow-fed mice, leading to

augmentation of the diet groups [336]. It is unclear if this was due to the strain selection or the amplified metabolic stress seen in male mice. In older C57/BL6 mice females inevitably lose bone regardless of diet; whereas males show sensitivity over study duration losing more bone with HFD [371]. Therefore, female mice can represent slower onset disease such as the prolonged insulin resistance of human pre-diabetes leading to eventual overt disease.

The NOD·B10 HF-*foz/foz* results at 13 weeks of age supported this earlier diabetic capture. Polygenic hyperglycaemia and obesity were manifest from 10 weeks of age in TSOD mice, in comparison to healthy age-matched and older comparator animals [295]. Similarly, a T1DM study using NOD and NOD·SCID mice supported changes to bone independent of BMD, were dictated by the life stage and time of diabetes induction [372]. The use of diet-mutation vulnerability has been successfully demonstrated in this chapter, in agreement with the previous literature. This premise supports the research aim to investigate emerging diabetes effects on younger bone.

A 9 week feed regime to assess femoral bone microstructure under T2DM induction is well supported by the literature. Brown and colleagues conducted a 12 week diet study in male C57/BL6 mice from 5 weeks of age, revealing differences by diet-induced T2DM [329]. This protocol was also used by Inzana and colleagues, concurring similar adaptations at the femur in these younger mice, and more pronounced than in older mice of typical aging studies [332].

Immature mice on HFD later switched to standard diet did not recover bone aspects unlike initially mature mice who were able to rectify skeletal changes, identifying the challenge of bone remodelling overwriting structural adaptations [332]. In a non-diabetic study of selective *Pkd1* mutants, profound deficiencies observed at 8 weeks of age were repaired 8 weeks later as aging presided above mutation [373]. Thus earlier time course studies such as 13 weeks of age are essential to intersect peak growth and disease emergence, to capture dynamic bone alterations under T2DM.

A lifetime bone aging study of WT BALB/c from 2-20 months concluded the strain's desirability as an intermediate phenotype for bone structure [374, 375]. This is further supported by earlier genetic analysis confirming BALB/c's validity as a moderate, or intermediate strain: thus serving appropriate spectrum of lean to obesity groups for this study [364]. Similar body weight, euglycaemia and mildly elevated plasma insulin lend the

BALB/c to developing healthy obesity, with resistance to T2DM under the genetic and dietary conditions imposed.

NOD·B10 HF-*foz/foz* female mice achieved the desired phenotype with highest body weight, hyperinsulinemia and hyperglycaemia by 13 weeks of age [353]. Metabolic bone structural work has concentrated on C57/BL6 as a polygenic mouse model of obesity via HFD. The diversity of diabetes demands a variety of models to capture the disease heterogeneity. The existing literature does not delve further into the bone microarchitecture nor strength of NOD·B10 mice, such that peak growth and strain characterisation are unknown, the focus of the next chapter.

6 Microstructural Results of the Distal Femur by Strain

6.1 Introduction

The previous chapter established the desired disease phenotypes in accordance with the existing literature. Female NOD·B10 HF-*foz/foz* mice developed diabetes and obesity whilst BALB/c mice developed only obesity by identical treatment. The NOD·B10 strain is yet to be characterised for bone microstructure whereas WT BALB/c mice have been studied prior [374]. Therefore we believe this was the first characterisation of the selected strains by this regime.

We posed the microstructural benefits of studying younger female mice with heightened sensitivity for low bone turnover and bone loss. Aged bone presents greater heterogeneity in both humans and mice complicating interpretations of pathologic change, thus younger mice avoided senile osteoporosis [376, 377]. This project focused on investigating bone microstructure during disease emergence as a critical starting point for future work.

As a long bone the femur is a trabecular rich site, which is responsive to load bearing and the metabolic demands of younger tissue. The femur is profoundly implicated in human T2DM, in defiance of the classical obese protection at this site. In practice, the distal femur encapsulates the distal growth plate providing a reproducible and reliable landmark for micro-CT analyses [362].

Non-destructive micro-CT enables quantitative analysis of compositional bone structure in addition to BMD. Desktop micro-CT is a high resolution tool for 3D imaging of bone structures, superior to two dimensional stereological techniques [378]. The 360 degree image acquisition provides higher accuracy of true spatial parameters using the sphere-fitting method. Modern analyses build upon the original cone-beam equation published by Feldkamp and colleagues using a polychromatic x-ray beam to directly render images [379].

Three measures are reported to describe trabecular microstructure and infer strength properties. Trabecular number (Tb.N) reports the incidence of trabeculae for a stipulated unit length (mm^{-1} or μm^{-1}). Trabecular thickness (Tb.Th) is the average width of any given trabeculae (μm), and trabecular separation (Tb.Sp) is the average distance between adjacent trabeculae (μm). Both thickness and separation parameters are calculated by the 3D sphere-fitting model for the largest negative space fit to the structure or background, respectively. The bone volume fraction (BV/TV) is a percentage (%) expression of the

quantity of trabecular bone relative to other tissue elements in a sample, site specifically [380].

Excessive changes in the distribution or size of trabeculae indicate pathological changes to bone metabolism and structural integrity [381]. As bone remodelling depreciates, the bone volume fraction diminishes, most drastically in postmenopausal women [382]. Trabecular bone state is accordingly most responsive in young tissue which is inevitably lost over the lifetime [178]. Loss of trabeculae increases the proportion of the cortical compartment, leading to trabecularisation of the remaining bone surface [358].

The orientation of bone tissue is essential to its redundancy under stress, whereby intact samples exhibited greater heterogeneity than isotropic fracture cases, despite matched bone volume fraction and trabecular number [263]. Three dimensional organisation is represented by the degree of anisotropy (DA), with values above 1.0 indicating favourable heterogeneity [378].

BMD is indirectly measured, with conversion of the attenuation coefficient (inverse distance of x-ray beam) absorption. Phantoms of known elemental composition and mass of calcium hydroxyapatite ($Ca_5(PO_4)^3(OH)$) are used to approximate the mineral content of bone tissue. The x-ray attenuation co-efficient for a given experiment is calibrated allowing calculation of calcium hydroxyapatite content present under the experimental conditions imposed. Bone mineral density is distinguished from tissue mineral density (TMD), an exclusively cortical measure of the hydroxyapatite content present in a sample without peripheral tissue inclusion [378]. BMD is favoured as a holistic but non-specific measure of the hydroxyapatite composition present in a bone sample [358].

Inclusion of the cortical perimeter of the distal femur encapsulates the extent of connectivity of the sampled bone network. Cortical porosity is implicated in bone fragility, as pore volume increases with diabetes and age impairing bone strength [383, 384]. Connectivity can be inferred by the extent of open or closed nature of the pore system. Open pores enable the shear fluid system to maintain diffusion critical to trabecular bone, with a minimum of one other connection in 3D space [385], as opposed to closed pore volume which contributes to the total porosity.

6.2 Micro-CT Results

6.2.1 Diabetic NOD·B10 Achieved Trabecular Distinction with Equivalent BMD

Microarchitecture analysis of the distal femur revealed differential trabecular thickness (Tb.Th) amongst HF-fed NOD·B10 mice (Figure 9). HF-*foz/foz* mice achieved significantly thinner trabeculae (4.18 ± 0.27 µm, *log2 transform*) than the HF-WT mice (4.29 ± 0.12 µm, *log2 transform*). A trend for thinner trabeculae was observed amongst chow-*foz/foz* mice, however did not reach significance. The diabetic group also showed a trend for higher trabecular number than the non-diabetic mice, however did not reach significance (Figure 10).

HF-WT mice appeared to have fewer trabeculae than HF-*foz/foz* mice however this finding did not reach significance. The large variation amongst *foz/foz* mutants of both diets may have obscured this finding. Microarchitecture did not differ on the basis of trabecular separation (Tb.Sp), which was maintained across the NOD·B10 cohort irrespective of diet nor mutation stress (Figure 11). Bone volume fraction (BV/TV) was agreeable between littermates confirming equal sampling of the femur (Figure 12). Together the data supported true distinction among HF-fed mice by trabecular number, secondary to the observed thickness result.

NOD·B10 mice exhibited equal femoral BMD across the cohort (Figure 13). The HF-*foz/foz* mice reported equivalent hydroxyapatite content to non-diabetic mice despite hyperinsulinemia, hyperglycaemia and marked obesity. Notably chow-WT mice showed the lowest mean however largest variation, which may have obscured a slightly higher BMD of all three experimental groups relative to the control. However, the consistent and high BV/TV across each group supports a conserved BMD irrespective of diet and genetic stress at 13 weeks of age. To ensure the BMD result was not influenced by cortical bone, porosity measurements encompassing both compartments of the sampled bone volume were also obtained.

The high BV/TV prohibited structure model index characterisation of the distal femur, insightful to conversion of plate to rod-like architecture with aging and osteoporosis [378]. Instead, the degree of anisotropy (DA) provided a relative measure of the tissue organisation across the cohort as secondary evidence to the BMD results (Figure 14). Invariant differences in the DA validated similar tissue organisation at 13 weeks of age. To confirm mice were not osteoporotic, the open (Op. V) and total pore volumes (Po.Tot V) were compared by groups (Figure 15, 16). Pore volumes were insignificant, and showed

the abundance of open, rather than isolated pores contributed to the overall volume. 3D image representations supported an emerging difference between *foz/foz* mutants and WT (Figure 8). NOD·B10 mice were not osteoporotic as anticipated at 13 weeks of age exhibiting a well-connected and similarly organised bone tissue network at the distal femur.

6.2.2 Obese BALB/c Mice Conserved Trabecular Architecture and BMD

BALB/c mice exhibited similar trabecular parameters at the distal femur irrespective of treatment condition(s). Despite obesity and mild hyperinsulinemia, the HF-*foz/foz* mice measured equal parameters to the single treatment groups. Trabecular thickness (Tb.Th) appeared slightly lower amongst HF-fed littermates yet did not reach significance (Figure 9). Trabecular number (Tb.N) appeared slightly higher amongst HF-fed mice however did not reach significance compared with chow-fed counterparts (Figure 10).

Trabecular separation (Tb.Sp) reflected a complementary pattern, whereby HF-fed mice reported nearer trabeculae than chow-fed mice, without achieving significance (Figure 11). Bone volume fraction (BV/TV) was agreeable between groups (Figure 12). The undifferentiated profile of BALB/c mice suggested a conserved trabecular microarchitecture of the distal femur at 13 weeks of age.

In accordance with a conserved BV/TV the BMD was high amongst all groups (Figure 13). There appeared a trend of increasing mean BMD with diet and genetic treatments which did not achieve significance. The DA was consistent across the cohort (Figure 14). By cortical inclusion, BALB/c littermates showed similar pore volumes, largely comprised of connected pores, which contraindicated osteoporosis at 13 weeks of age (Figure 15, 16). The distal femur maintained stable microarchitecture despite obesity and slight hyperinsulinemia detected in the obese BALB/c mice.

6.2.3 Inherent Strain Differences Precluded Microstructural Comparisons

Strain was the significant effect driving microstructural outcomes by 3-way ANOVA. Trabecular number and thickness were affected by strain (Tb.N: $p=0.0001$; Tb. Th: $p<0.0001$, both 3-way ANOVAs). Trabecular separation was not significantly different, and the degree of anisotropy was also consistent across strain backgrounds which supported similar orientation of measured trabeculae. The bone volume fraction was equivalent, demonstrating sampling consistency in the femoral metaphysis.

Rather, microstructural differences were reflected in the BMD ($p<0.0001$) and the open ($p=0.0017$) and total porosity ($p=0.0015$) by strain (*strain effect*, all 3-way ANOVAs). Diet

and genotype were not significant or interacting effects at this level. In consideration with the other results, these stark and inherent differences did not support direct comparisons between strains for over-representation of diabetic changes, and other strain variation undistinguished from the treatment response.

Consulting the qualitative images (Figure 9) this stance was affirmed. The BALB/c mice showed a larger cortical fraction at the maximum height (180 slices offset from growth plate) of the ROI than NOD·B10 mice in all cases. The 3D reconstructions showed much greater trabecular population of the volume of interest for BALB/c mice. Despite uniform sampling referenced by the growth plate landmark, bone shape appeared to differ by strain, irrespective of treatment group. The distal femur section of NOD·B10 mice was trapezoid, whereas the BALB/c section was ellipsoid, which suggested different properties and size. Altogether these observations supported the inference of strain-endemic BMD. Together these outcomes contraindicated comparisons across strain backgrounds.

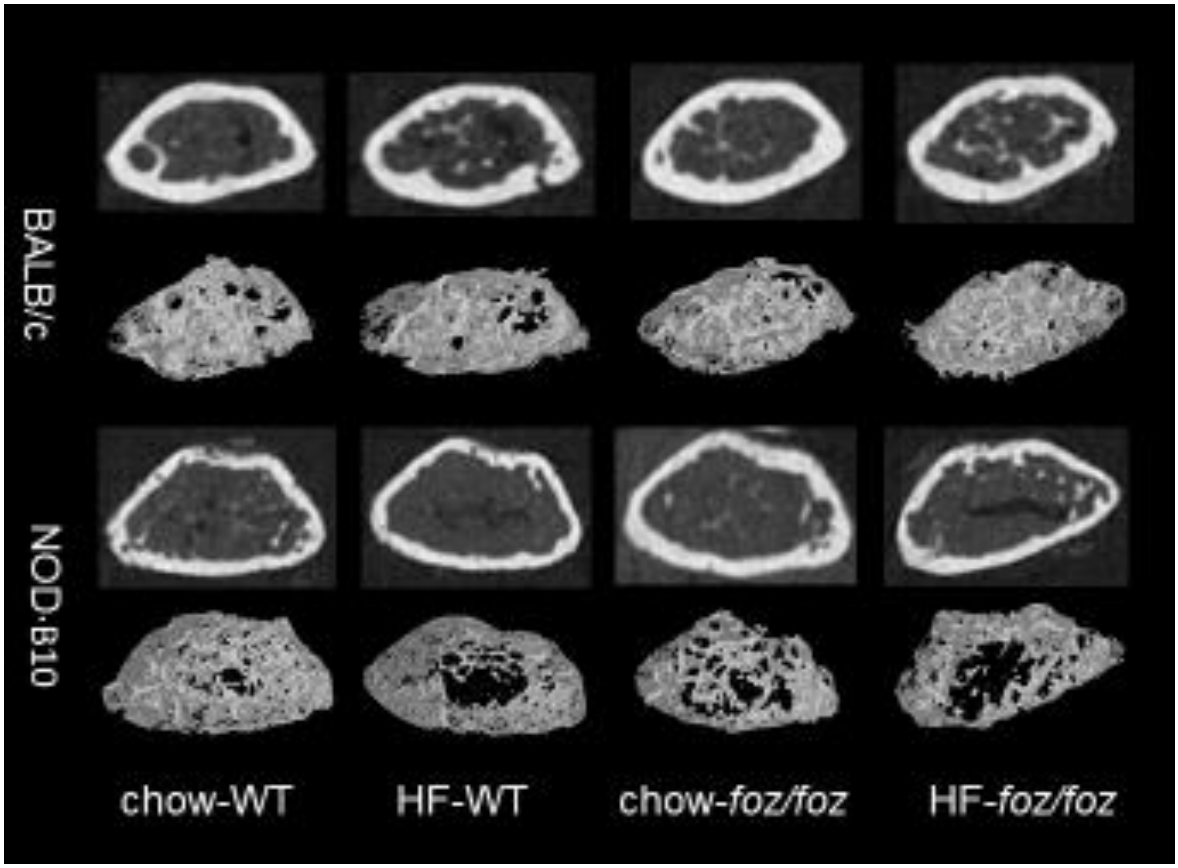

Figure 8 Microstructural Evidence of Inherent Strain-Specific Architecture of the Distal Femur at 13 Weeks of Age amongst Female Mice Regardless Of Challenge Group

By strain, upper row: Micro-CT image of highest slice sampled in ROI (180 slices above growth plate), 2D transverse section predominantly cortical bone. By strain, lower row: 3D reconstructions of volume of interest from binarised image sets (composite 100 slices). Images resized, ordered by challenge group from left to right: chow-WT, HF-WT, chow-*foz/foz,* HF-*foz/foz*. Profound inter-strain differences in microstructure of the distal femur supported strain-endemic analyses.

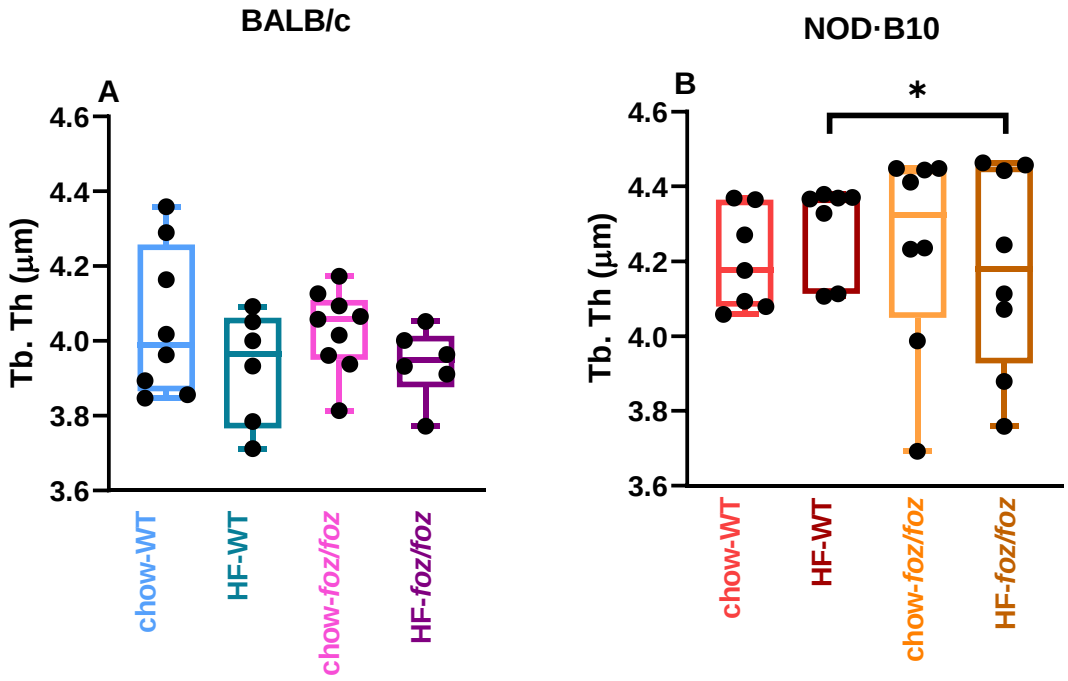

Figure 9 Trabecular Thickness by Diet and Genetic Challenge(s) at the Distal Femur of 13 Week Old Female Mice

(A) HF-*foz/foz* BALB/c mice maintained trabecular thickness to healthy littermates at 13 weeks of age (*n=6-9/group*). Significance determined by 2-way ANOVA with Sidak's adjustment for multiple comparisons *(p>0.05).* (B) NOD·B10 mice on HFD showed differential trabecular thickness by mutation *(n=7-8/group).* Significance determined by Mann-Whitney U test *(p<0.05*). Data plotted as min to max, transformed by log (base 2) scale. **p<0.05*. Trabecular thickness (Tb.Th) expressed in micro-metres (µm).

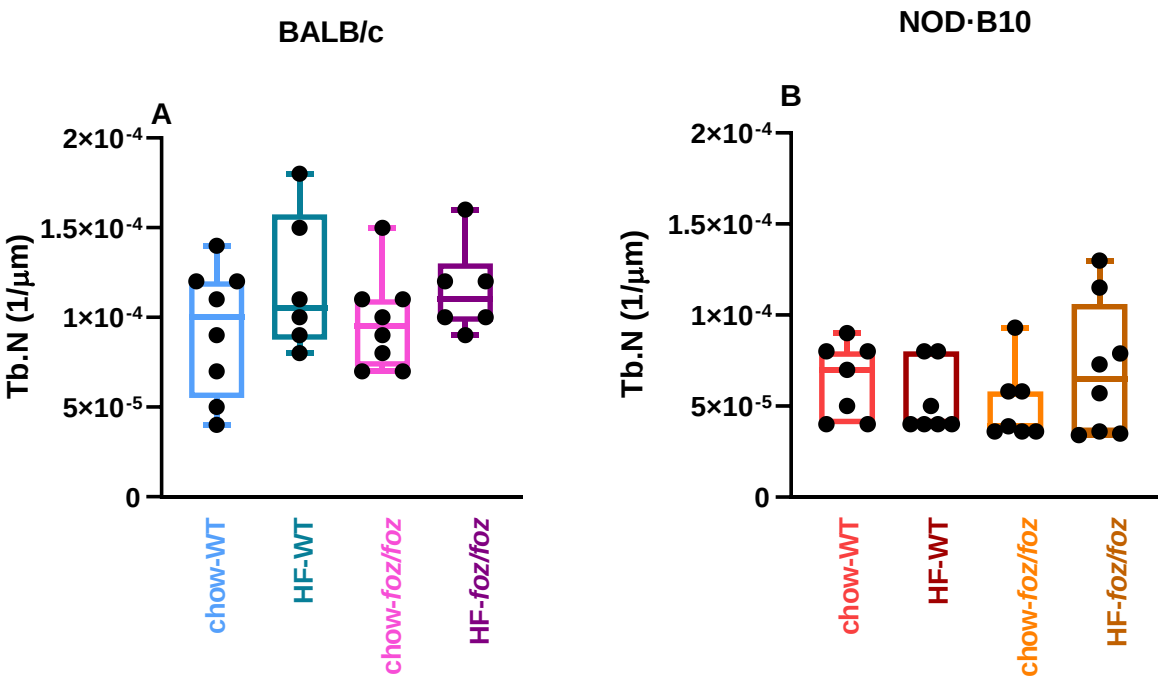

Figure 10 Trabecular Number by Diet and Genetic Challenge(s) at the Distal Femur of 13 Week Old Female Mice

(A) HF-*foz/foz* BALB/c mice maintained trabecular number to non-obese littermates *(n=6-9/group*). Significance determined by 2-way ANOVA with Sidak's adjustment for multiple comparisons *(p>0.05).* (B) HF-*foz/foz* NOD·B10 trabecular number was consistent with non-diabetic littermates (*n=7-8/group*). Significance determined by Mann-Whitney U test (*p>0.05*). Data plotted as min to max. No significance. Trabecular number (Tb. N) expressed as incidence per micrometre (1/µm).

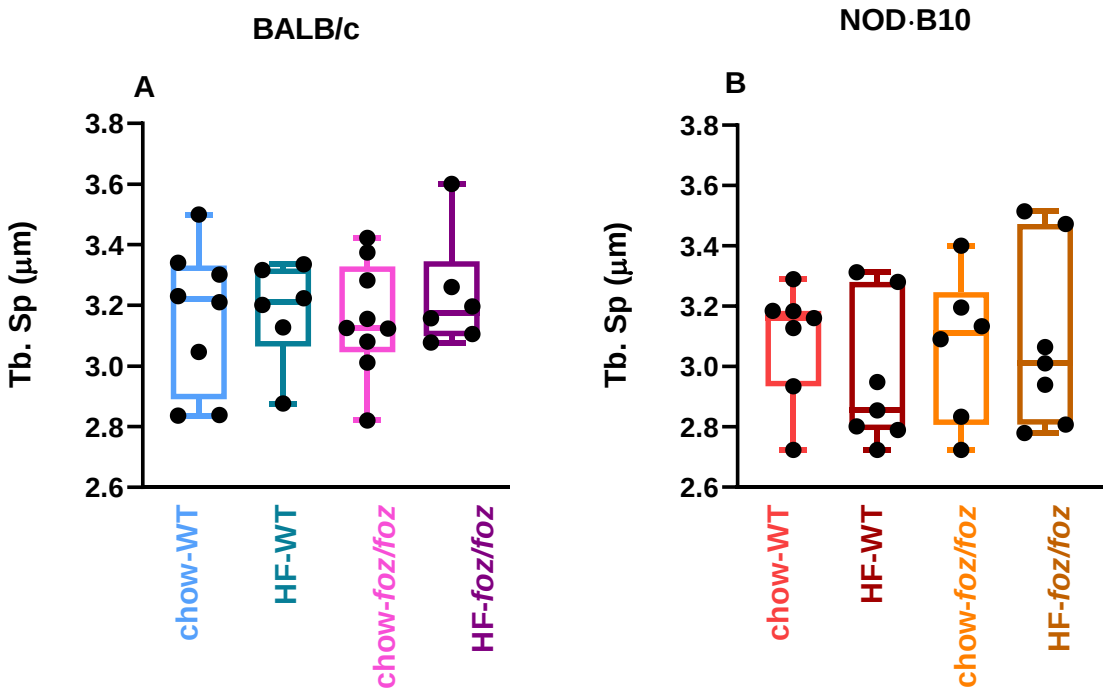

Figure 11 Trabecular Separation by Diet and Genetic Challenge(s) at the Distal Femur of 13 Week Old Female Mice

(A) HF-*foz/foz* BALB/c mice maintained trabecular separation to non-obese littermates *(n=6-9/group)*. Significance determined by 2-way ANOVA with Sidak's adjustment for multiple comparisons *(p>0.05).* (B) HF-*foz/foz* NOD·B10 mice maintained trabecular separation to non-diabetic littermates *(n=7-8/group).* Significance determined by 2-way ANOVA with Sidak's adjustment for multiple comparisons *(p>0.05).* Data plotted as min to max, transformed by log (base 2) scale. No significance. Trabecular separation (Tb.Sp) expressed in micrometres (µm).

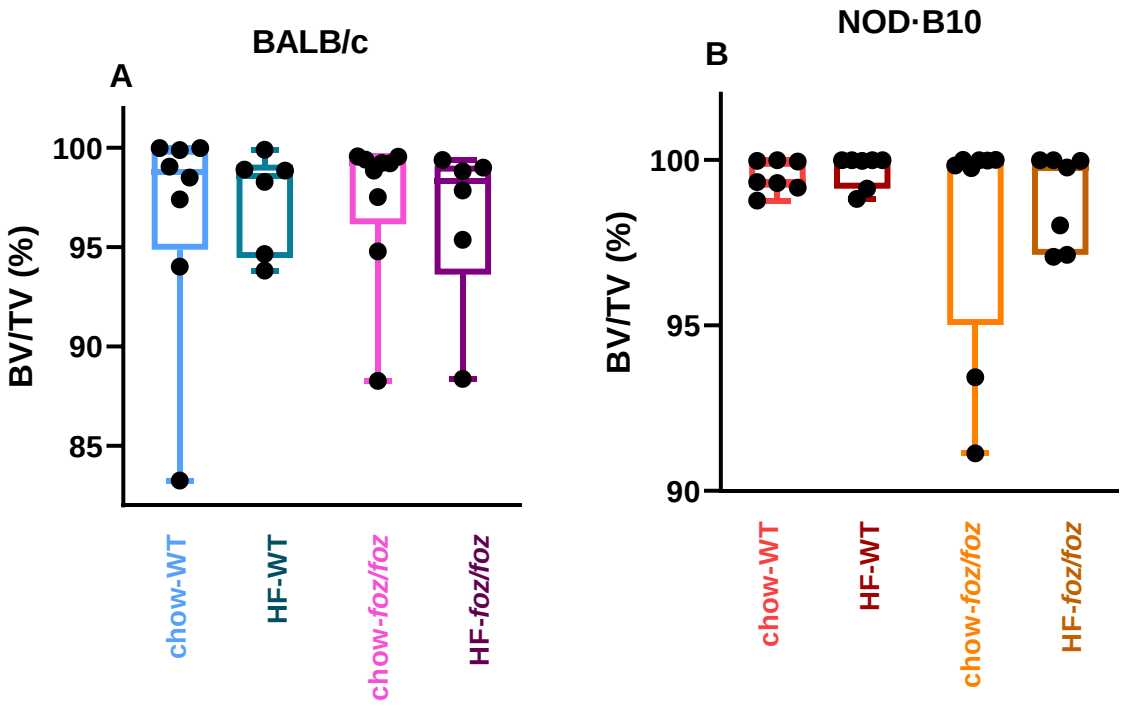

Figure 12 Trabecular Bone Volume Fraction by Diet and Genetic Challenge(s) at the Distal Femur of 13 Week Old Female Mice

(A) HF-*foz/foz* BALB/c mice measured equivalent bone volume fraction to non-obese littermates *(n=6-9/group).* Significance determined by Mann-Whitney U test *(p>0.05).* (B) HF-*foz/foz* NOD·B10 mice measured equivalent bone volume fraction to non-diabetic littermates *(n=7-8/group).* Significance determined by Mann-Whitney U test (*p>0.05).* Data plotted as min to max. No significance. Bone volume fraction expressed as bone volume/tissue volume (BV/TV) as a percentage (%).

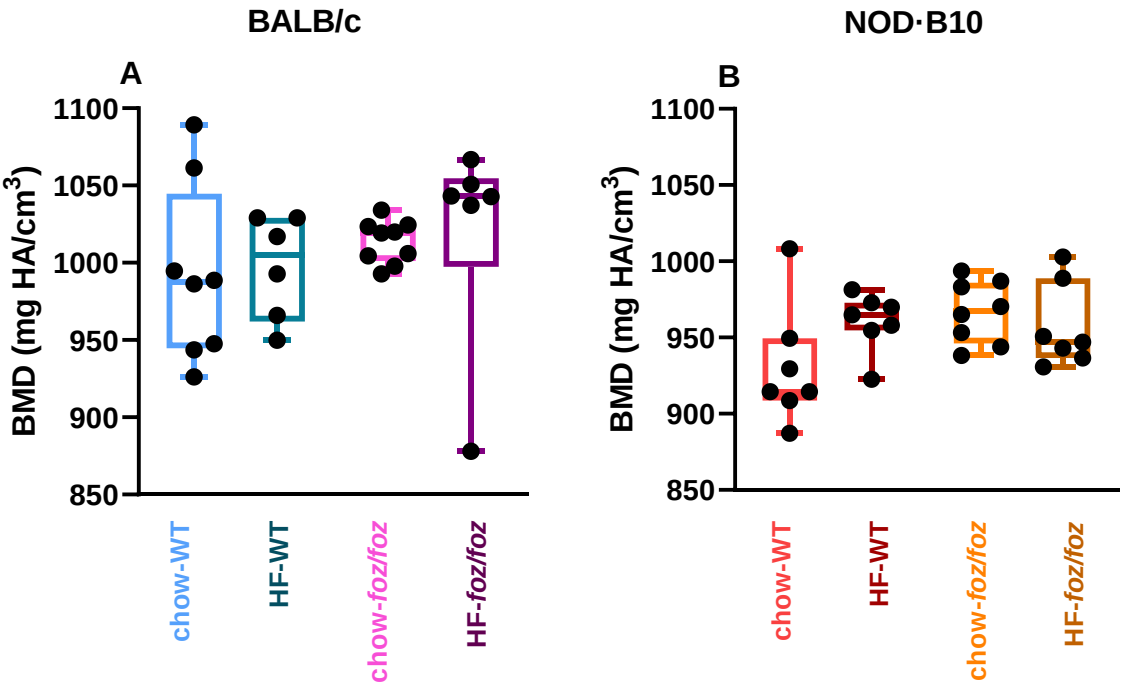

Figure 13 Bone Mineral Density by Diet and Genetic Challenge(s) at the Distal Femur of 13 Week Old Female Mice

(A) HF-*foz/foz* BALB/c mice measured equal bone mineral density to non-obese littermates *(n=6-9/group).* Significance determined by 2-way ANOVA with Sidak's adjustment for multiple comparisons *(p>0.05).* (B) HF-*foz/foz* NOD·B10 mice measured equal bone mineral density to non-diabetic littermates *(n=7-8/group).* Significance determined by 2-way ANOVA with Sidak's adjustment for multiple comparisons *(p>0.05).* Data plotted min to max. No significance. Bone mineral density (BMD) expressed as milligrams of hydroxyapatite per centimetre cubed (mg HA/cm^3).

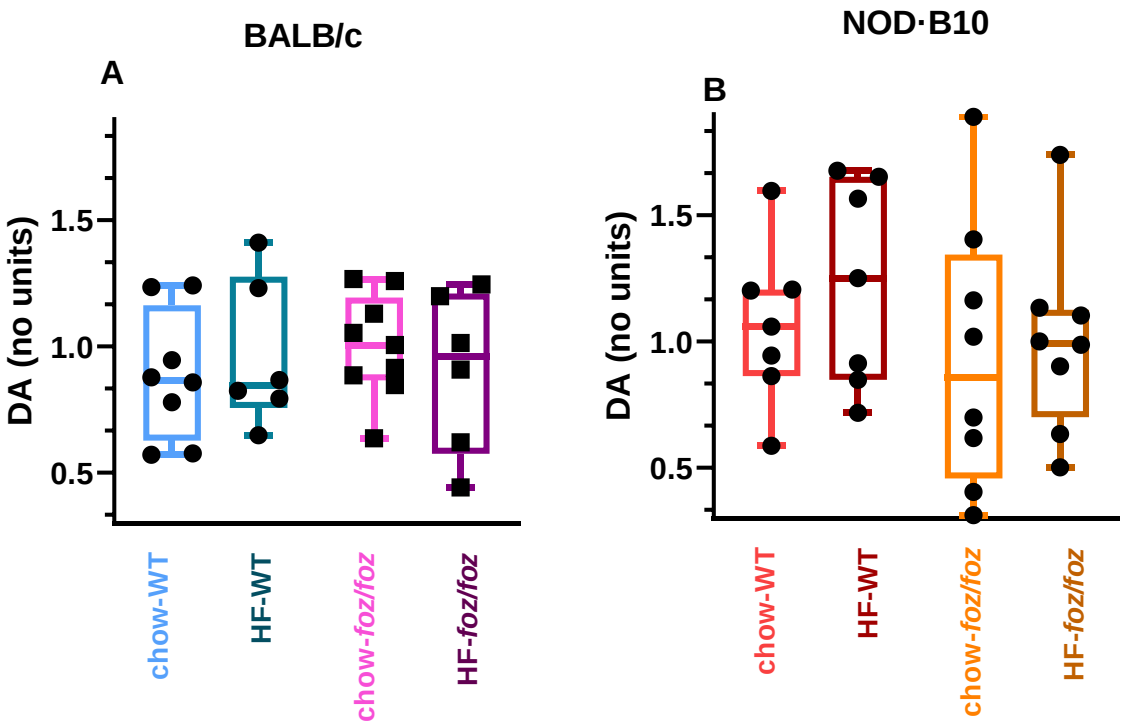

Figure 14 Trabecular Degree of Anisotropy by Diet and Genetic Challenge(s) at the Distal Femur of 13 Week Old Female Mice

(A) HF-*foz/foz* BALB/c mice had similar anisotropy to non-obese littermates *(n=6-9/group).* Significance determined by 2-way ANOVA with Sidak's adjustment for multiple comparisons *(p>0.05).* (B) HF-*foz/foz* NOD·B10 mice had similar anisotropy to non-diabetic littermates *(n=7-8/group).* Significance determined by 2-way ANOVA with Sidak's adjustment for multiple comparisons *(p>0.05).* Data plotted min to max, transformed by log (base 2) scale. No significance. Degree of anisotropy (DA) expressed with no units.

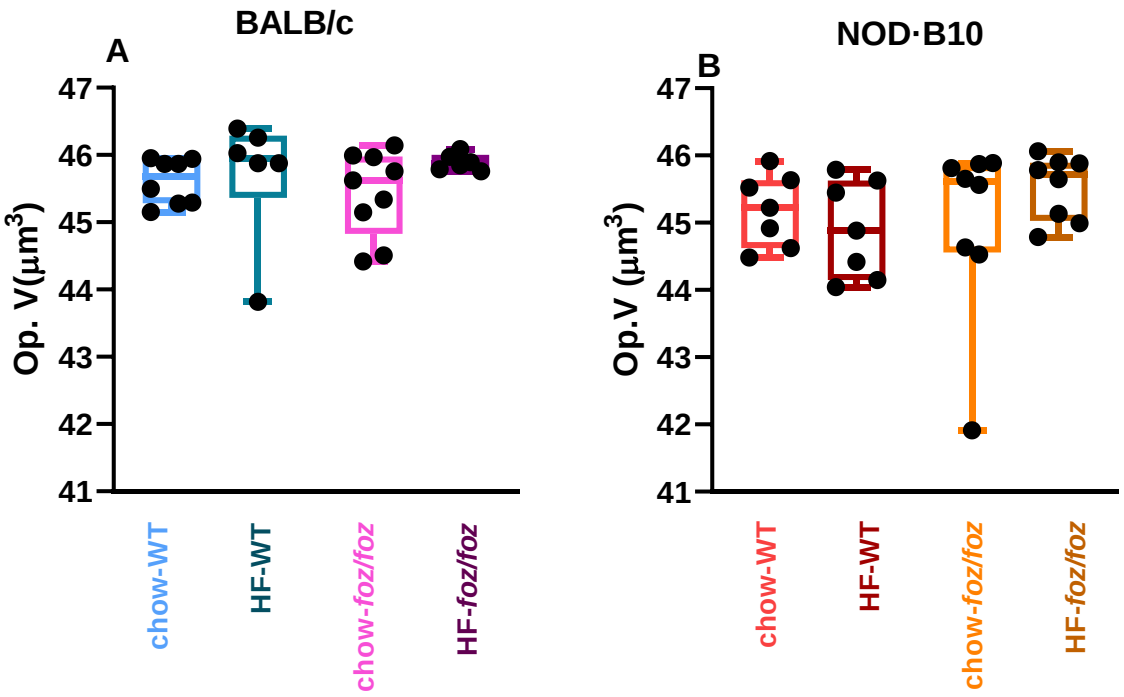

Figure 15 Cortical Open Pore Volume by Diet and Genetic Challenge(s) at the Distal Femur of 13 Week Old Female Mice

(A) HF-*foz/foz* BALB/c mice had equal pore volume to non-obese littermates (*n=6-9/group)*. Significance determined by 2-way ANOVA with Sidak's adjustment for multiple comparisons *(p>0.05).* (B) HF-*foz/foz* NOD·B10 mice had equal pore volume to non-diabetic littermates *(n=7-8/group).* Significance determined by Mann-Whitney ranking *(p>0.05).* Data plotted as min to max transformed by log (base 2) scale. No significance. Open pore volume (Op.V) expressed as cubic volume in micrometres (μm^3).

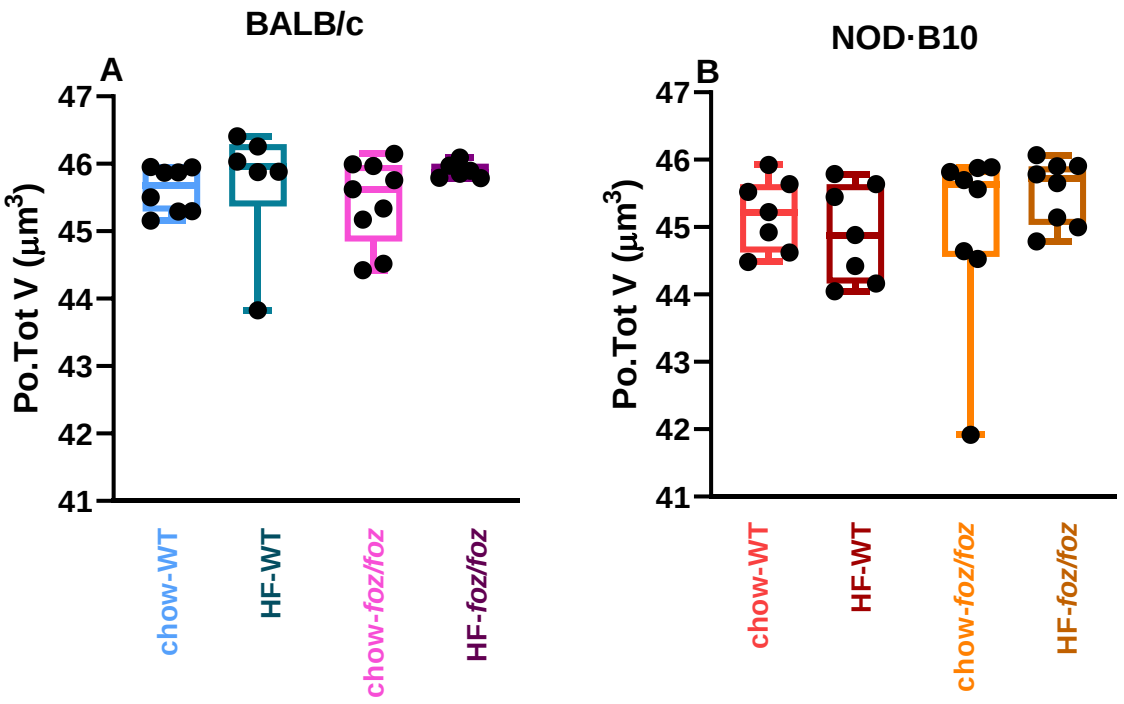

Figure 16 Cortical Total Pore Volume by Diet and Genetic Challenge(s) at the Distal Femur of 13 Week Old Female Mice

(A) Obese BALB/c mice maintained total pore volume to non-obese littermates (*n=6-9/group).* Significance determined by 2-way ANOVA with Sidak's adjustment for multiple comparisons *(p>0.05).* (B) HF-*foz/foz* NOD·B10 mice maintained total pore volume to non-diabetic littermates (n=7-8/group). Significance determined by Mann-Whitney U-test *(p>0.05).* Data plotted as min to max transformed by log (base 2) scale. No significance. Total pore volume (Po.Tot.V) expressed as cubic volume in micrometres (μm^3).

6.3 Discussion of Microstructural Findings

6.3.1 Diabetic Mice Achieved Thinner Trabeculae at the Distal Femur

The HF- fed groups of NOD·B10 mice showed different trabecular thickness responses. WT mice achieved thicker trabeculae compared to *foz/foz* mutants without further distinction. HF-WT mice were not significantly heavier, glycaemic, nor insulinemic compared to the chow-WT mice. Reciprocally, HF-*foz/foz* mice achieved thinner trabeculae yet no further discrimination amongst the cohort. Irrespective of mutation, chow-fed mice did not reflect altered trabecular thickness. This subtle difference in trabecular compensation was not captured by BMD of diabetic mice, supporting the contention of trabecular inclusion in bone appraisal.

Trabecular indices can compensate one another in bone diseases such as osteoporosis, whereby diminishing trabeculae (as product of age) is mediated by thickening, to retain bone volume fraction as periosteum expands and trabeculae migrate [265]. Typically, thinner trabeculae have inferior protection, and age-related decline in trabecular thickness is associated with increased fracture likelihood or collapse, clinically observed as sub-chondral fracture crescent [263].

A reduction in trabecular thickness was observed in the HF-*foz/foz* mice, posited as an early diabetic compensation. In a non-diabetic longitudinal study of male and female C57/BL6 mice, Glatt and colleagues demonstrated the gradual increase in trabecular thickness, and loss of trabecular number with transition from bone modelling to remodelling from 2-6 months of age [177]. Contrary to larger-bodied mammals, Barak and colleagues contend that Tb.N is more responsive than Tb.Th in mice and rodents [386]. The femoral result for the HF-*foz/foz* mice opposes this generalisation of standard remodelling.

Mice have a lower range of trabecular thickness, due to rapid osteoblast activity (scaled to lifespan), small body size and a lack of secondary remodelling. The human range for trabecular number is less varied, and thickness can readily adapt, whereby intratrabecular tunnelling is observed in larger mammals [387]. Osteoclasts can sub-divide existing trabeculae to new struts. Under PTH administration, trabecular density increases whilst remodelling cycles uphold trabecular thickness [388]. Exaggerated tunnelling can lead to perforation when the anisotropic maximum is exceeded [389]. The differential thickness result amongst HF-fed NOD·B10 may be an intratrabecular tunnelling strategy.

In the previous study, the cortical BMD did not increase to match enlarged surface area under longstanding PTH intervention, whereas the trabecular fraction responded [390]. In agreement, a study of intracortical bone loss in T2DM patients averaging 63 years of age found a 10% increase in trabecular BMD thought to offset age-associated porosity, however cortical trabecularisation was not explored [391]. With a common BMD amongst NOD·B10 mice, differences in trabecular features were reflective of emerging adaptations nonetheless still confined to the non-diabetic range by the 9 week regime.

To contextually frame this investigation as a growth and disease onset study, rather than an aging convergence, cortical parameters were expected to be negligible. To check the totality of BMD was not influenced by osteoporosis, cortical analysis for the same region of interest was performed. The closed pore volume contribution was negligible when observing the portion of total pore volume provided by open pores. All tissue scored similar anisotropy supporting similar micro-crack protection. This emphasises the connectivity of the tissue conformed as expected and did not indicate osteoporosis, complementing high BV/TV and BMD outcomes expected of the femur metaphysis proximal to the growth plate.

Alongside equal BMD, the fundamental trabecular contribution to femoral bone quality was demonstrated. In accord, a study comparing NOD (T1DM) with NOD·SCID (non-diabetic) mice showed less trabecular number from 5 weeks of age; less trabecular bone volume and apparent osteoporosis despite unchanged BMD [372]. Similarly, in overt T1DM, osteopenia was apparent by trabecular deficits from 10 weeks after STZ-induced disease: supported by lesser biomechanical strength outcomes and tissue mineralisation [392]. By the same sensitivity, if osteoporosis were an influence, the current protocol would have detected this fragility refuted by the data.

Identical porosity outcomes across treatments suggested the trabecular thickness and distribution for HF-WT mice comprised an increased volume as opposed to surface area than HF-*foz/foz* mice. Greater volume limits the remodelling capacity as trabecular osteons are restricted to surface movement in two dimensions [4]. This outcome was surprising, and may hint at other connotations of surface area to volume expansion.

The relative abundance of osteocytes to adequately regulate the bone surface; the area exposed to AGE attachment; and the net diffusion properties of lesser surface area to greater volume require further examination. A limited mineral interface for bone remodelling may also prevent addition of new trabeculae, but could also avoid perforation. Different structural adaptations require further appraisal to clarify exact mechanisms at work.

In an undisclosed osteopetrotic strain murine trabeculae were thinner, proximal and more abundant at 4 and 7 month measurement, supported by osteoclastic marker reduction [38]. Despite gaining the most body weight, HF-*foz/foz* mice did not report higher BMD and trabecular features contraindicating osteopetrosis. Osteophyte growths to dissipate load were also contraindicated; without lowered Tb.N accompanying trabecular thinning proposed to expand osteoarthritic joint surfaces [393]. The detected HF-*foz/foz* response was discriminated by overt hyperglycaemia from control and single treatment groups.

The equal porosity across the NOD·B10 cohort supported the relevance of trabecular variation at this age in the distal femur. The divergence may expand over a longer timeframe of both age and diabetes. More work is required to explore the implicit diabetic response of sustained hyperglycaemia, such as frank diabetic animals. The detrimental extent of these factors on skeletal acquisition and lifetime bone remodelling capacity remains to be determined by longitudinal studies.

In the current field of research, trabecular assessment may have been obscured by end point sampling. Spontaneous frank diabetic KK-Ay male mice reported thinner, more dispersed trabeculae than C57/BL6 comparators by 15-week chow diet [394]. Authors observed higher TMD but lower trabecular BMD at the distal femur of diabetic mice, opposing our findings [394]. On the contrary, the ongoing modification of bone coincident with aging can also remove thinner trabeculae to reinforce the residual struts. Diabetic male C57/BL6 mice on 14 week 60% kcal HFD showed this trabecular audit, and fortified their fewer trabeculae than chow-fed mice [395].

Variations based on disease status, diet protocols, the opted ROI and study durations all factor into the apparent heterogeneity in the literature. Among this wider disparity, studies on female mouse bone microstructure at ovulation age (preceding osteoporosis) are scarce [257]. The dominance of male mouse models does not capture the sex-specific differences in initial architecture and metabolic sensitivity that may produce different microstructural outcomes.

6.3.2 Obese BALB/c Mice Maintained Distal Femoral Microstructure

The HFD tendency to more and adjacent trabeculae, whilst not achieving significance, appeared independent of body weight loading on the skeleton. HF-WT mice were indistinct from chow-WT metabolic outcomes. BALB/c microarchitecture did not follow the increasing body weight trend. A longitudinal study of lean, healthy (WT) BALB/c mice reported pronounced increase in TMD between 2 and 4 months of age due to slower cortical

thickening and increasing body mass [374]. Whilst the current study obtained BMD rather than mid-diaphyseal TMD, it is plausible that peak growth was still occurring at the time of sampling. In the prior study, authors reported tibial BV/TV peaked slightly later at 4 months of age before subsequent decline [374].

Despite mild hyperinsulinemia and obesity, trabecular architecture conformed to non-obese and healthy experimental groups at 13 weeks of age. By long-term regime, trabecular architecture might improve, alike 9 month 24% kcal fat regime in Wistar rats [396]. The HF-fed rats exhibited unchanged bone turn over markers, yet improved BV/TV, Tb.N and decreased Tb.Sp [396]. The fat content of our design is not disputed, however may require chronic feeding duration to detect statistically significant structural changes implied by this finding. Furthermore, caged mice may have limited physical activity, which could have dampened the contrast between the underactive *foz/foz* mutants and their WT counterparts.

Diet induced obesity (DIO) models predominantly based on male C57/BL6 mice do not report trabecular thickness outcomes, unlike this project. Upon 60% kcal high fat feeding for 24 weeks an increase in trabecular separation and reduction in trabecular number were reported with later loss of connectivity [335]. Increased separation at the micro-metre scale is negatively associated with bone strength [397]. This vulnerability was not detected in BALB/c mice at 13 weeks of age, despite 9 weeks of HFD.

C57/BL6 mice did not report changed femoral volumetric BMD, yield strain or maximal strain by diet, rather the expansion of bone size and cortical indices with obesity and displacement of adjacent trabeculae [398]. Conducted longer term, at a higher fat content, this finding unsurprisingly challenges our own result. The androgen protection of male mice in longer duration studies and the inherent differences in nutritional metabolism and skeletal structure contraindicated inter-strain generalisations, compounded by different protocols [399, 400].

Supported by bone turn over analyses, 45% kcal HFD appeared to halt bone remodelling, sustaining higher BMD at the expense of bone quality in male C57/BL6 [401]. Instigating HFD after skeletal maturity, higher BV/TV correlated with thicker, abundant trabeculae compared to both age-matched and entry-age chow-fed mice [401]. This finding contradicts the previous DIO study demonstrating the temporal specifications which ultimately dictate skeletal adaptation. The BALB/c mice do not exhibit altered BMD or other bone microstructural indices irrespective of diet or mutation assignment at 13 weeks of age.

Longitudinal investigation is required to ascertain time of skeletal response to stress challenge(s) in the strain.

In murine DIO models, high fat feeding increased initial weight and body size, however attenuated size-dependence to an upper limit imposed by 18 weeks of age [398]. Importantly, Dagpo's work states how BALB/c mice achieve smaller body size than NOD·B10 mice, despite equivalent body weight at 12 weeks of age [353]. Longer term validation beyond 120 days of age is justified as the microarchitecture of both strains under identical protocol has not been previously reported.

6.3.3 BALB/c and NOD·B10 Distal Femoral Microstructure Was Inherently Different

The aim of this chapter was to establish the bone microstructure and BMD responses of BALB/c and NOD·B10 cohorts with micro-CT of the distal femur. The structural adaptation of femoral bone to the diet and genetic challenges provides the basis for later non-imaging characterisation of pathological modifications. Micro-CT analysis revealed modest changes to bone microstructure at 13 weeks of age within strains. In contrast, the profound differences in strain-specific bone microstructure were apparent. This thesis characterises the previously unreported bone phenotype for healthy and diseased NOD·B10 mice, markedly different to the BALB/c cohort.

BALB/c mice reflected greater frequency of thinner, abundant trabeculae, and higher BMD than NOD·B10 mice across all treatment regimes. A greater density of thinner trabeculae lends greater surface area for osteoid deposition, in explanation of the higher BMD per volumetric unit than equal weight NOD·B10 mice. Further microstructural validation of the NOD·B10 strain is warranted to identify the appropriate clinical sub-population represented by this model.

Trabecular inter-strain differences were previously reported at both 6 and 12 weeks between C3H and C57/BL6 mice [402]. A follow-up study using electron microscopy did not find significant micro or nano evidence for the opposing structural features of each age-matched strain [403]. By extension, longitudinal growth amongst BALB/c, C57/BL6 and C3H males proceeded equally from 8-10 weeks, before significant divergence between strains [375]. Vertebral architecture became more marked and permanently distinct by strain, whilst tibial architecture was more dynamic by thickness and bone volume fraction over time [375]. The trabecular thickening in a similar length regime supported our finding of the emerging difference in trabecular response to HFD by WT and *foz/foz* mutants

among NOD·B10 mice. This new finding requires further validation with complementary genetic analysis and longitudinal structural analyses as NOD·B10 mice have not been characterised previously.

Secondarily the conforming BALB/c microarchitecture across experimental groups reflects the inferior architecture observed by Buie and colleagues in comparison to the C3H and C57/BL6 [375]. Therefore, direct comparisons across strains were not presented to avoid over-representation of the bone phenotype present in only the diabetic NOD·B10 HF-*foz/foz* mice. Other research groups have addressed this issue with comparisons of closer related strains of diabetic and non-diabetic mice, such as the TSOD and TNSO mice [295]. The structural resilience of the BALB/c cohort affirmed the decision to avoid an inter-strain approach, and excluded the BALB/c mice from further investigation in this thesis.

It is highly plausible that the selected strains achieved different growth trajectories, which would explain the differences detected at 13 weeks of age. In 2015, Dagpo observed different weight gain projections for each strain: initially NOD·B10 mice were heavier; however BALB/c mice caught up by 8-12 weeks [353]. Mutant *foz/foz* mice in this project achieved equivalent body weight at 13 weeks across strains by experimental group. Body size measurements were not taken. However, similar body weight at 13 weeks of age contraindicated a correction for trabecular parameters. The high BV/TV affirmed good sampling practice and excluded operator error in trabecular boundary mapping of micro-CT images.

Despite the similar lifespan of the two strains, skeletogenesis and life staging events may occur differentially in female BALB/c and NOD·B10 mice. The possibility of peak growth beyond 13 weeks of age requires further validation to ensure that longitudinal sampling is an accurate representation of bone microstructure, especially considering the inter-strain variation demonstrated in this study.

The NOD·B10 cohort requires further investigation to interpret diet and genetic stress responses which may not yet manifest in ongoing bone microstructure. The NOD·B10 strain was selected for biochemical analyses in the following chapter to investigate group-specific changes in bone metabolism to capture non-structural adaptations to obesity-borne diabetes.

7 Biochemical Results of Female NOD·B10 Mice

7.1 Introduction

The prior chapter describes the relatively consistent trabecular bone microarchitecture observed for the NOD·B10 mice. These findings require further characterisation by gene expression profile to inform the extent of cell signalling responses yet to manifest in trabecular features. This chapter aims to profile NOD·B10 treatment groups for detection of differentially expressed genes, to provide insight to the state of transcriptional bone metabolism at 13 weeks of age.

This data will assist to contextualise the young NOD·B10 model amongst the wider literature of T2DM rodent models, and orient the murine findings to human disease. Left femurs were processed for isolation of RNA and reverse transcription to synthesise a single strand of cDNA for RT-qPCR analysis by comprehensive 84-gene profiler array of osteogenesis.

PCR is the amplification of a DNA product in the genome, to infer gene activity with relative expression levels to a control. Whole RNA isolation and purification removes prior DNA and other contaminants from which a single strand of purified complementary DNA is synthesised. The manufactured cDNA provides a proxy for the mRNA transcript encoded by genes to detect altered cell responses. Prior to translation, aberrant gene expression may or may not constitute an altered protein product. This PCR performance included the whole bone, encapsulating the bone tissue, marrow, and vasculature to detect the extent of variant gene expression to reconcile with microstructural data.

Relative expression of each gene was normalised to the housekeeping reference gene β-glucuronidase (*Gusb)*. To surpass background noise, the significance threshold was determined by 1.5-fold absolute change compared to the chow-WT group. Whilst this method may over-represent some findings, it enables detection of genes with a narrow or wide dynamic range, whereby an arbitrary fold change may be comparatively significant in one gene and not in another.

From the breadth of PCR findings one gene of interest was selected for protein expression levels in serum. Rather than confirming or denying the same pattern of expression in the blood, this approach was useful to inform a systemic point of differentiation between groups. ELISA was used to quantify protein levels, measured by relative optical density of the plate reader absorbance.

ELISA uses antibody binding to capture the protein of interest present in a sample [404]. Once bound to the primary antibody, further steps are undertaken to remove contaminants and refine the antigen binding. A secondary antibody, which binds to other epitopes of the primary antibody is conjugated to biotin. Addition of horseradish peroxidase (HRP)-Streptavidin amplifies the desired antibody-antigen capture improving detection. A chromogenic substrate is added to convert the HRP-labelled complex to a colorimetric product. The end point is invoked by addition of a stop solution preventing further enzyme conversion. The colorimetric product is excited by plate reader laser, with intensity of signal proportional to the desired antigen. The sensitivity of ELISA favours routine diagnostic use to determine protein analyte levels.

7.2 Gene Expression Profile Results Determined by RT-qPCR Array

7.2.1 Skeletal Development Signalling Was Most Differential for Diabetic Mice

Amongst the NOD·B10 cohort, the obese diabetic group differentially expressed four skeletal development genes detected by PCR array. HF-*foz/foz* mice under-expressed fibroblast growth factor receptor 2 (*Fgfr2*), insulin-like growth factor 1 receptor (*Igf1r*) and runt-related transcription factor 2 (*Runx2*) genes at 13 weeks of age (Figures 18, 20, 21). *Igf1r* is specific to ossification, whilst *Fgfr2* and *Runx2* genes are pertinent to both ossification and osteoblast differentiation. Under-expression of master osteoblast transcription factor *Runx2* was not reflected in downstream target genes (*Dlx5, Sp7, Spp1, Bglap*) at this time, a key finding of this project (Figure 19).

These bone matrix protein gene expression levels were conspicuously lower in the HF-*foz/foz* group compared to single-treatment groups however did not reach significance. *Sox 9* expression levels were similar across all experimental groups. Together, the evidence contraindicated immature osteoblast induction from MSC progenitors in the femur. The lack of overt under-expression of afore mentioned bone matrix proteins indicated transcriptional regulation of osteoblasts was not profoundly impaired at 13 weeks of age.

Only bone morphogenic protein 5 (*Bmp5*) was over-expressed at statistical significance by the HF-*foz/foz* group, which supported the inference of non-proliferative signalling (Figure 17). Osteoinductive genes (*Acvr1, Bmpr1a, Bmpr1b, Bmp2r, Bmp2, 4, 6, 7, Col1a1, Col2a1, Csf1, Fgf2, Igf1*) were invariantly expressed across the cohort. Inhibitory Bmp/Tgf-β genes (*Ahsg, Bmp3, Smad 1, 3, Chrd, Gdf10, Gli1, Nog, Tgfb1, 2, 3*) were not detectably altered by mutation nor feed assignment despite markedly high *Smad1* expression amongst HF-WT mice.

In conjunction with *Runx2* under-expression, *Cdh11* levels were consistent across the cohort. *Twist1* stability and invariant *Sox9* levels corroborated diminished *Runx2* expression without canonical Wnt activation to maintain the MSC progeny pool. Unremarkable *Ihh* expression levels supported normal developmental ossification for all NOD·B10 littermates.

Amongst mutants, there was a trend of lower expression than the HF-WT mean for osteogenic genes (*Sost, Smad1, Rankl, Bmp4, Bmpr2*, and *Runx2)* however, this did not reach significance. Single treatment groups did not reveal differential expression of ossification genes nor osteoblast differentiation by femoral profiling at 13 weeks of age. The extent of modelling drift captured by the transcript profile requires further investigation.

Amongst other skeletal development genes HF-WT mice exclusively under expressed cartilage oligomeric matrix protein (*Comp*) at statistical significance (Figure 22). Relative expression of cartilage condensation genes (Figure 23) was consistent across the cohort of female NOD·B10 mice. Osteoclast differentiation genes (Figure 24) were not detected to be significantly altered across the cohort, irrespective of mutation or diet treatment(s). Downstream NF-KB, NFATc1 and p38/MAPK/ERK pathways were not substantially altered, remaining within the background threshold. This evidence did not suggest presence of skeletal dysplasia arising from aberrant osteoclast or chondrocyte populations.

The relative under-expression of *Runx2* could have indicated terminal differentiation and maturity of osteoblastic cell types. However, the hallmarks of osteoblastic maturity including over-expression of osteoinductive genes, *Alpl*, and coupled osteoclastic factors was not detected. Taken together, this evidence did not suggest an increased mineralising competency, or hyper-active osteoblastic activity to explain the femoral microstructure observed of the diabetic HF-*foz/foz* mice.

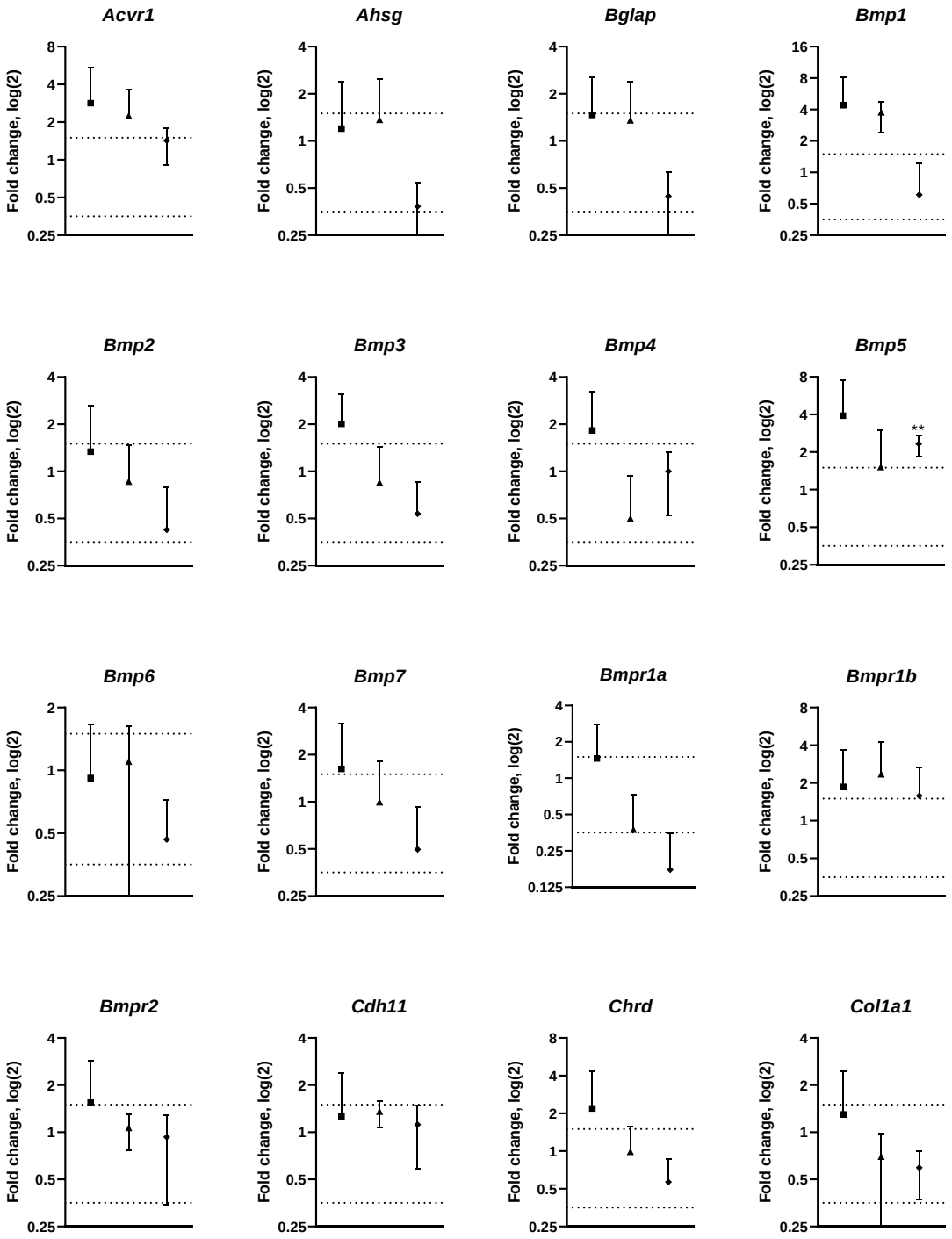

Figure 17 Ossification Gene *Bmp5* Was Differentially Expressed in the Femur of Female HF-*foz/foz* Mice at 13 Weeks of Age

RT-qPCR array data expressed as fold change relative to chow-WT control ($2^{-\Delta\Delta}$CT) ■ HF-WT, ▲chow-*foz/foz*, ◆HF-*foz/foz (n=3-4/group*), performed in unicate. Data presented as mean and 95% confidence interval (error bars). 2-tailed t-tests, reported from Qiagen© Gene globe data analysis software. All data normalised by β-glucoronidase (*Gusb*). Cut-off 1.5-fold absolute threshold depicted by dotted lines. Significance *'*' (p<0.05) '**'(p<0.01).*

SKELETAL DEVELOPMENT- Ossification (2)

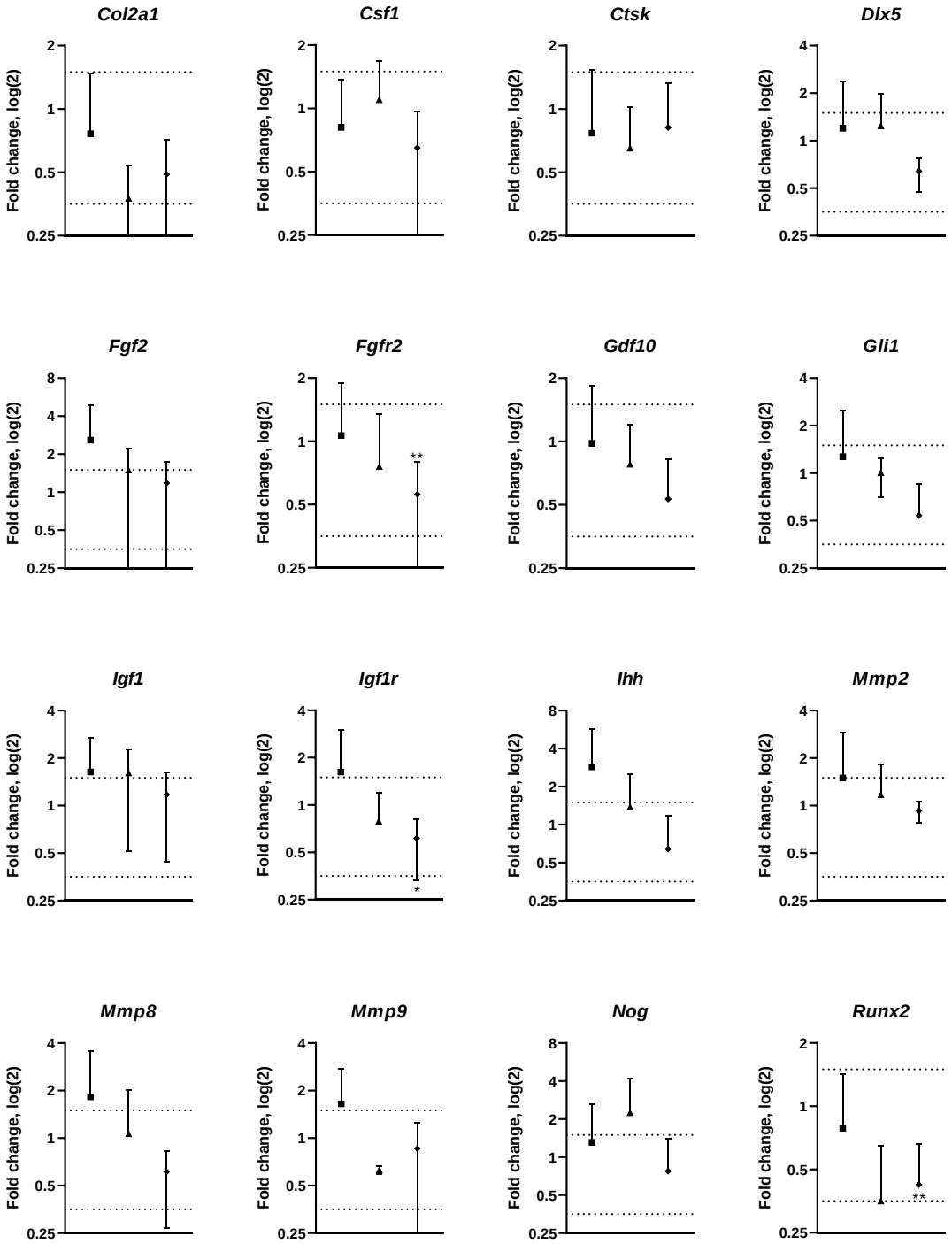

Figure 18 Ossification Genes *Fgfr2, Igf1r* and *Runx2* Were Differentially Expressed by Female HF-*foz/foz* Mice at 13 Weeks of Age

RT-qPCR array data expressed as fold change relative to chow-WT control ($2^{-\Delta\Delta}$CT) ■ HF-WT, ▲chow-*foz/foz*, ◆HF-*foz/foz* (*n=3-4/group),* performed in unicate*.* Data presented as mean and 95% confidence interval (error bars). 2-tailed t-tests, reported from Qiagen© Gene globe data analysis software. All data normalised by β-glucoronidase (*Gusb*). Cut-off 1.5-fold absolute threshold depicted by dotted lines. Significance *'*' (p<0.05) '**'(p<0.01).*

SKELTAL DEVELOPMENT- Ossification (3)

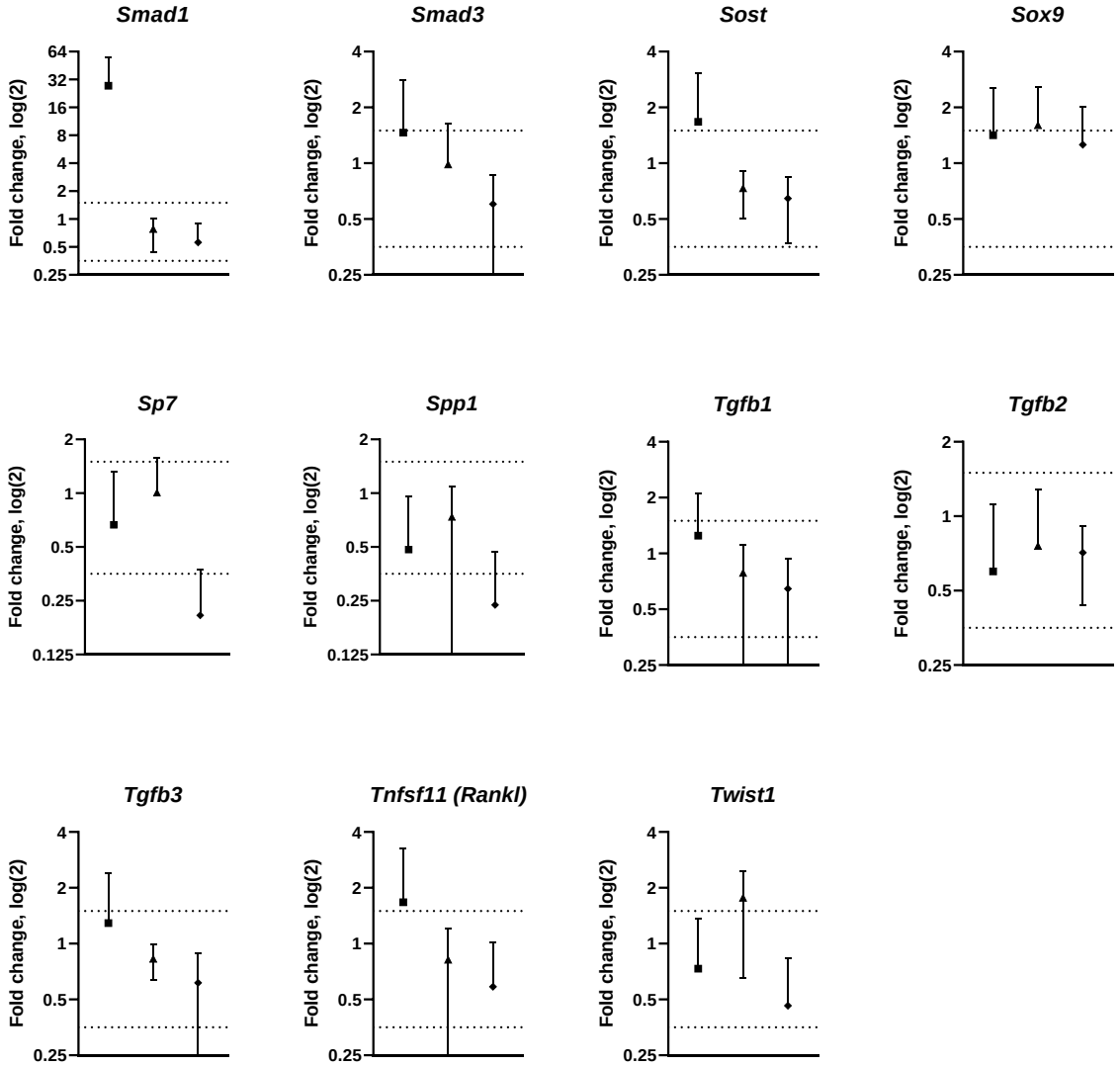

Figure 19 Other Ossification Genes Were Invariantly Expressed amongst Female NOD·B10 Mice at 13 Weeks of Age

RT-qPCR array data expressed as fold change relative to chow-WT control ($2^{-\Delta\Delta}$CT) ■ HF-WT, ▲chow-*foz/foz*, ◆HF-*foz/foz (n=3-4/group)*, performed in unicate. Data presented as mean and 95% confidence interval (error bars). 2-tailed t-tests, reported from Qiagen© Gene globe data analysis software. All data normalised by β-glucoronidase (*Gusb*). Cut-off 1.5-fold absolute threshold depicted by dotted lines. No significance.

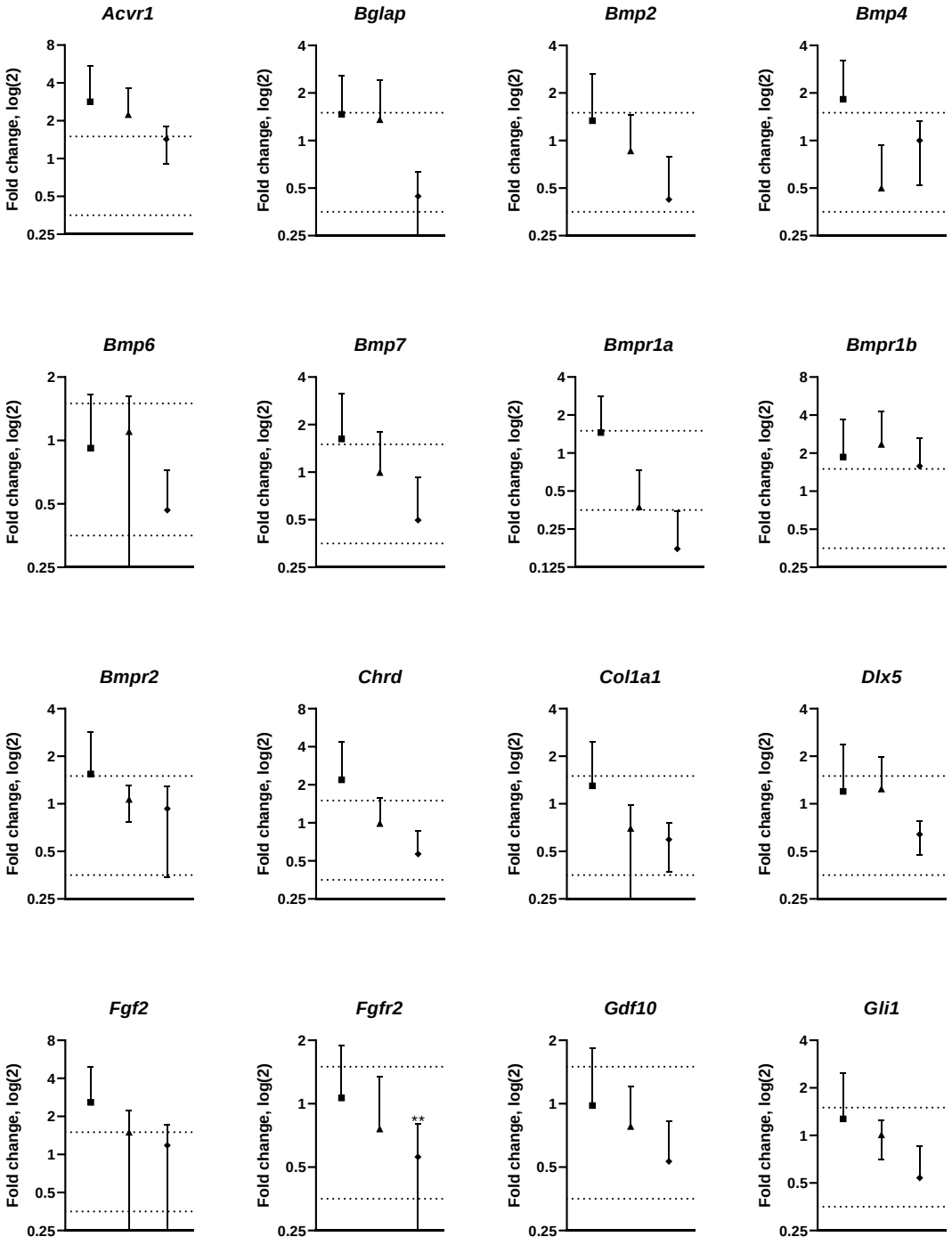

Figure 20 Osteoblast Differentiation Gene *Fgfr2* Was Under-expressed by Female HF-*foz/foz* Mice at 13 Weeks of Age

RT-qPCR array data expressed as fold change relative to chow-WT control ($2^{-\Delta\Delta}$CT) ■ HF-WT, ▲chow-*foz/foz*, ◆HF-*foz/foz (n=3-4/group)*, performed in unicate. Data presented as mean and 95% confidence interval (error bars). 2-tailed t-tests, reported from Qiagen© Gene globe data analysis software. All data normalised by β-glucoronidase (*Gusb*). Cut-off 1.5-fold absolute threshold depicted by dotted lines. Significance *'*' (p<0.05) '**'(p<0.01).*

SKELETAL DEVELOPMENT- Osteoblast Differentiation (2)

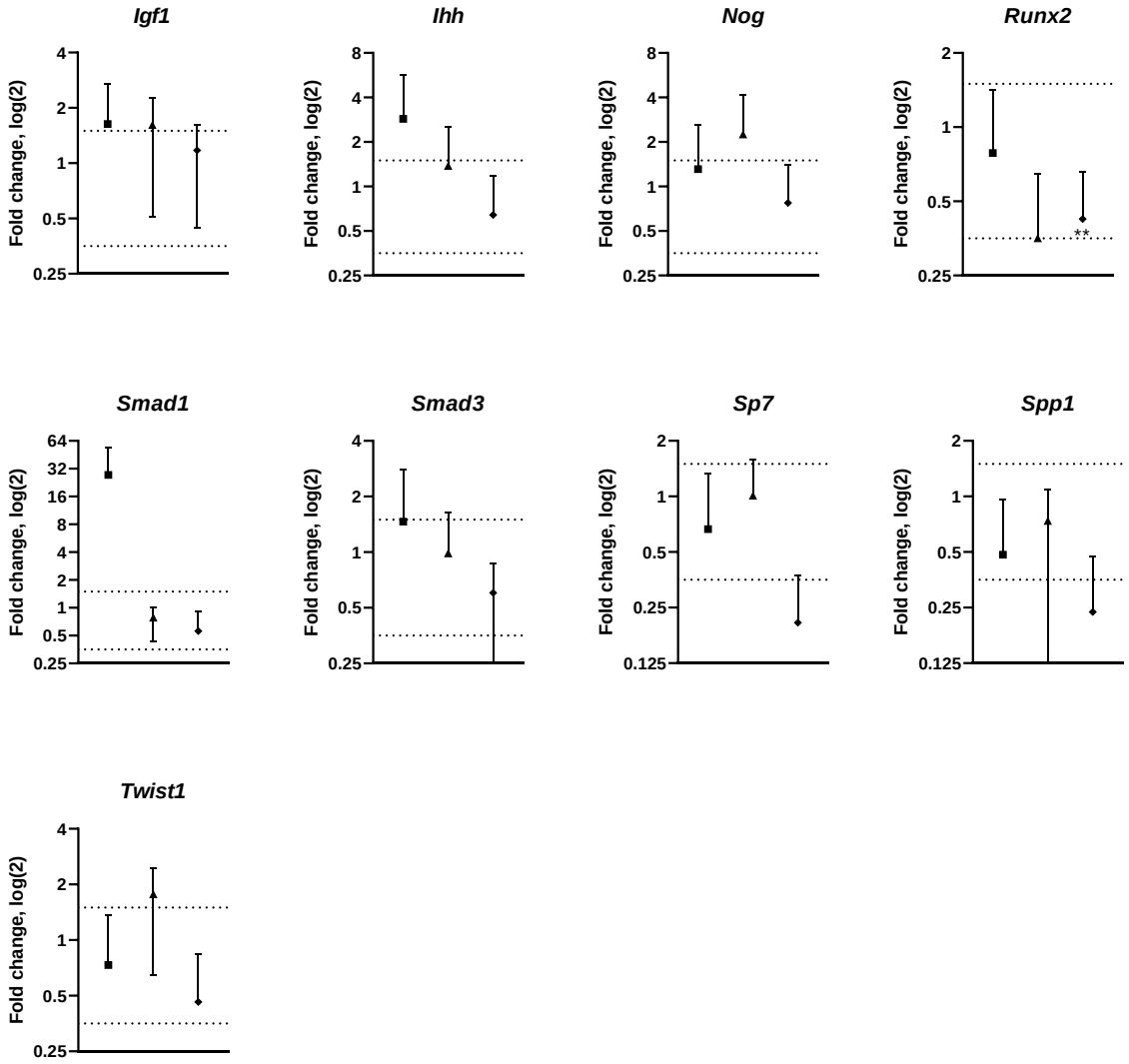

Figure 21 Osteoblast Differentiation Gene *Runx2* Was Under-expressed by Female HF-*foz/foz* Mice at 13 Weeks of Age

RT-qPCR array data expressed as fold change relative to chow-WT control ($2^{-\Delta\Delta}$CT) ■ HF-WT, ▲chow-*foz/foz*, ◆HF-*foz/foz (n=3-4/group)*, performed in unicate. Data presented as mean and 95% confidence interval (error bars). 2-tailed t-tests, reported from Qiagen© Gene globe data analysis software. All data normalised by β-glucoronidase (*Gusb*). Cut-off 1.5-fold absolute threshold depicted by dotted lines. Significance *'*' (p<0.05) '**'(p<0.01).*

SKELETAL DEVELOPMENT- Other Skeletal Development

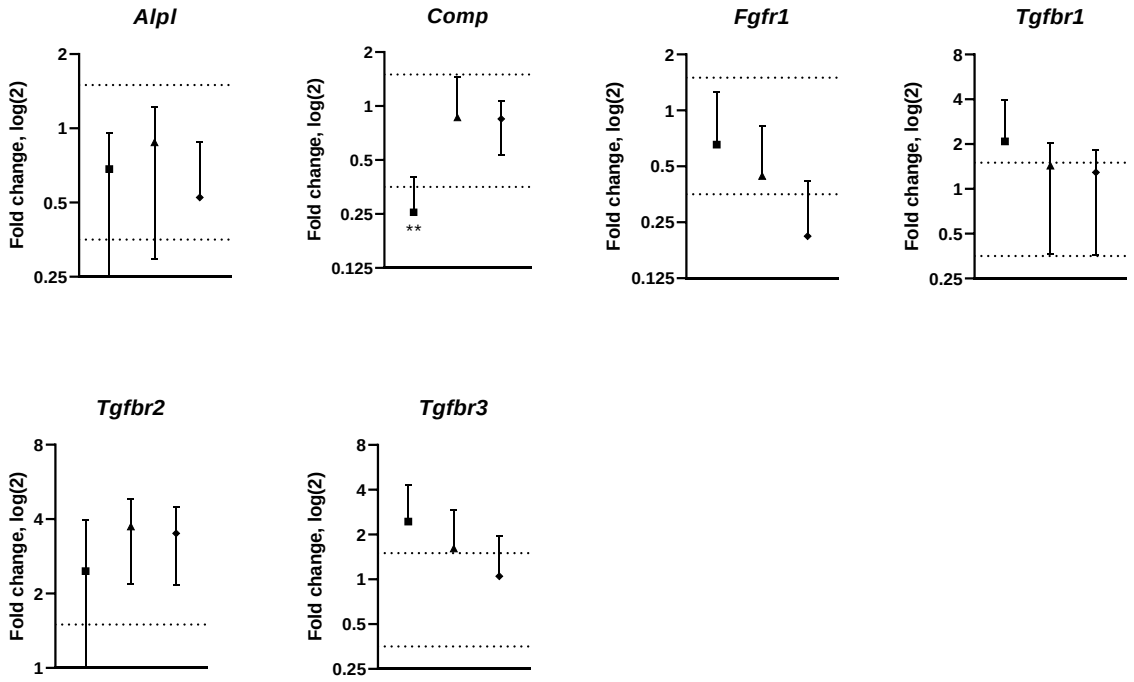

Figure 22 Other Skeletal Development Gene *Comp* Was Under-expressed in Female HF-WT Mice at 13 Weeks of Age

RT-qPCR array data expressed as fold change relative to chow-WT control ($2^{-\Delta\Delta}$CT) ■ HF-WT, ▲chow-*foz/foz*, ◆HF-*foz/foz (n=3-4/group)*, performed in unicate. Data presented as mean and 95% confidence interval (error bars). 2-tailed t-tests, reported from Qiagen© Gene globe data analysis software. All data normalised by β-glucoronidase (*Gusb*). Cut-off 1.5-fold absolute threshold depicted by dotted lines. Significance *'*' (p<0.05) '**'(p<0.01).*

SKELETAL DEVELOPMENT- Cartilage Condensation

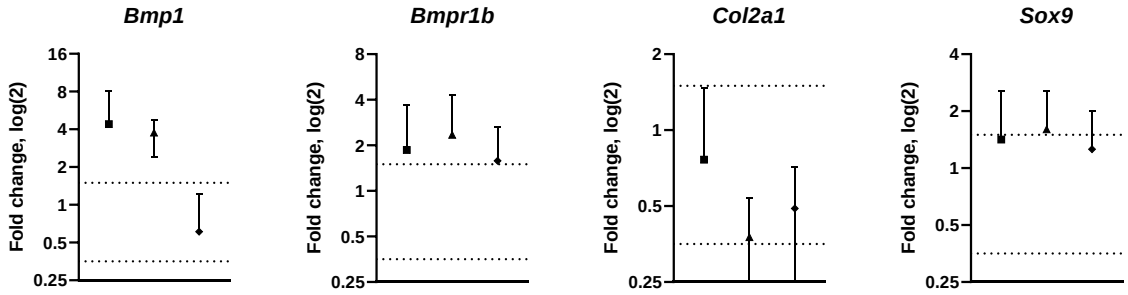

Figure 23 Cartilage Condensation Genes Were Invariantly Expressed by Female NOD·B10 Mice at 13 Weeks of Age

RT-qPCR array data expressed as fold change relative to chow-WT control ($2^{-\Delta\Delta}$CT) ■ HF-WT, ▲chow-*foz/foz*, ◆HF-*foz/foz (n=3-4/group)*, performed in unicate. Data presented as mean and 95% confidence interval (error bars). 2-tailed t-tests, reported from Qiagen© Gene globe data analysis software. All data normalised by β-glucoronidase *(Gusb).* Cut-off 1.5-fold absolute threshold depicted by dotted lines. No significance.

SKELETAL DVELOPMENT- Osteoclast Differentiation

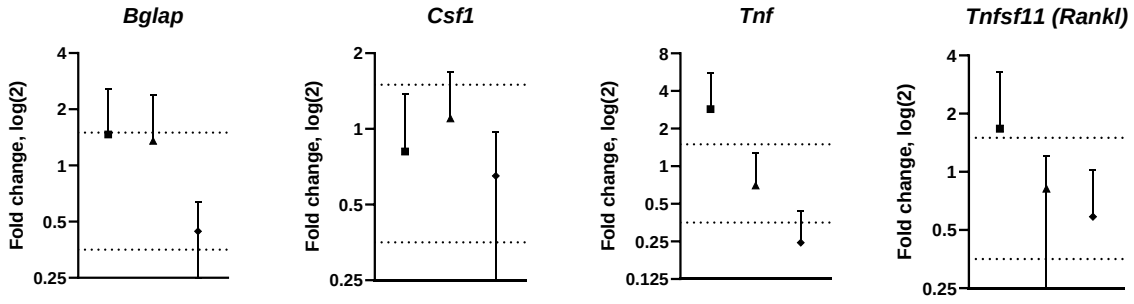

Figure 24 Osteoclast Differentiation Genes Were Invariantly Expressed by Female NOD·B10 Mice at 13 Weeks of Age

RT-qPCR array data expressed as fold change relative to chow-WT control ($2^{-\Delta\Delta}$CT) ■ HF-WT, ▲chow-*foz/foz*, ◆HF-*foz/foz (n=3-4/group)*, performed in unicate. Data presented as mean and 95% confidence interval (error bars). 2-tailed t-tests, reported from Qiagen© Gene globe data analysis software. All data normalised by β-glucoronidase *(Gusb).* Cut-off 1.5-fold absolute threshold depicted by dotted lines. No significance.

7.2.2 Bone Mineral Metabolism Signalling Was Variable by Challenge Group

Bone mineralisation gene *Fgfr2* was under-expressed at significance by the HF-*foz/foz* mice that concurred reciprocal regulation with *Runx2* (Figure 25). Other experimental groups did not exhibit changes to bone mineralisation genes, in accordance with the skeletal development findings (Figure 26).

Instead, calcium ion binding and homeostasis genes were differentially expressed by the single treatment groups (Figure 27). HF-WT mice under-expressed cartilage oligomeric matrix protein (*Comp)* unlike chow-fed and diabetic littermates. Chow-*foz/foz* mice over-expressed annexin a5 (*Anxa5)* gene at statistical significance, whilst HF-WT mice showed similar increase in expression, without reaching significance. All other bone mineralisation genes were not significantly varied by femoral PCR array.

In agreement with *Runx2* under-expression, pro-osteoblast *Egf* expression was not significantly altered. Integrin genes (*Itgav, Itgb1*) were not differentially expressed, therefore consistent with unchanged *Alp* expression across the cohort. *Fgf2*, contrary to the receptor was not discriminately expressed by any experimental group.

The vitamin D receptor (*Vdr)* gene appeared lower amongst the diabetic group without achieving statistical significance. Taken together, these findings suggested intact calcium and PTH feedback system across the cohort of female NOD·B10 mice. There was no transcriptional evidence for proliferative demand of mineral competent mature osteoblasts irrespective of mutation or diet stress.

7.2.3 Extracellular Matrix Signalling Was Differential for Diabetic Mice

The ECM protease gene phosphate regulating gene with homologies to endopeptidases on the X-chromosome (*Phex)* was under-expressed in HF-*foz/foz* mice at statistical significance (Figure 28). HF-WT mice exhibited the highest relative expression of *Phex*, which was decreased in chow-*foz/foz* mice and most reduced in the combined treatment group. No differences in relative expression of collagens, protease inhibitors and other ECM molecule genes were detected across the cohort of female NOD·B10 mice (Figures 29-31).

The *Bgn* levels exceeded the over-expression threshold across the cohort, however did not reach statistical significance in accord with a mildly quiescent osteogenic profile. *Flt 1* appeared lower in the HF-*foz/foz* group, however did not reach statistical significance: which contraindicated an increase in osteoblast differentiation. *Col1a2* exhibited higher

expression levels across the cohort than most fold-change data, but was not statistically profound. The solidarity of *Sepinh1* expression supported intact collagen and ECM component genes of the transcriptional profile.

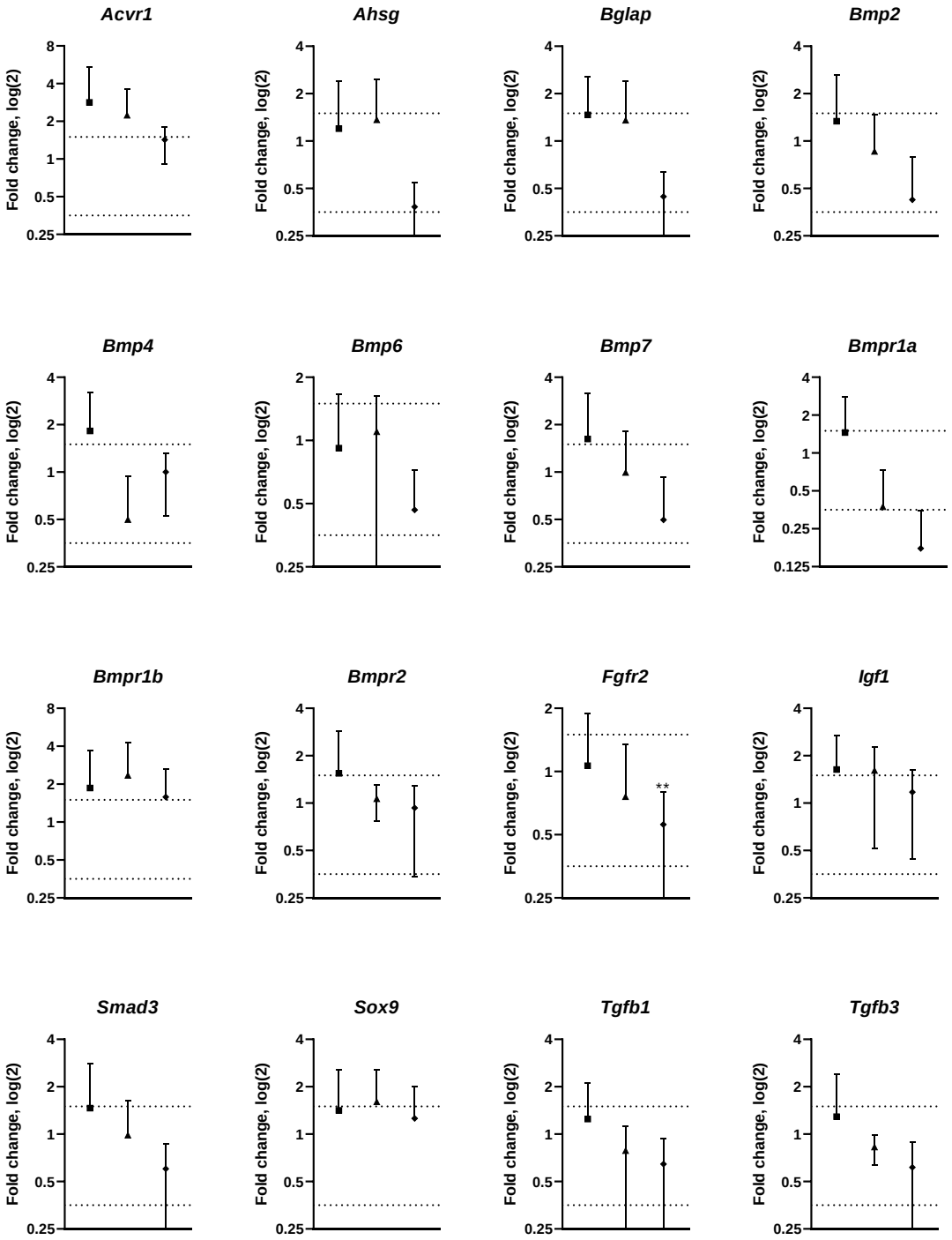

Figure 25 Bone Mineralisation Gene *Fgfr2* Was Under-expressed by Female HF-*foz/foz* Mice at 13 Weeks of Age

RT-qPCR array data expressed as fold change relative to chow-WT control ($2^{-\Delta\Delta}$CT) ■ HF-WT, ▲chow-*foz/foz*, ◆HF-*foz/foz (n=3-4/group)*, performed in unicate. Data presented as mean and 95% confidence interval (error bars). 2-tailed t-tests, reported from Qiagen© Gene globe data analysis software. All data normalised by β-glucoronidase *(Gusb).* Cut-off 1.5-fold absolute threshold depicted by dotted lines. Significance *'*' (p<0.05) '**'(p<0.01).*

BONE MINERAL METABOLISM- Bone Mineralisation (2)

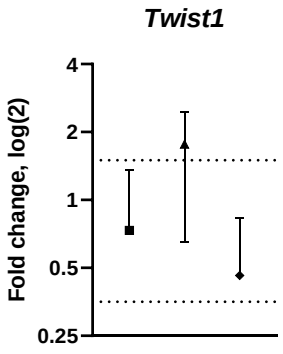

Figure 26 Bone Mineralisation (continued).

RT-qPCR array data expressed as fold change relative to chow-WT control ($2^{-\Delta\Delta}$CT) ■ HF-WT, ▲chow-*foz/foz*, ◆HF-*foz/foz (n=3-4/group)*, performed in unicate. Data presented as mean and 95% confidence interval (error bars). 2-tailed t-tests, reported from Qiagen© Gene globe data analysis software. All data normalised by β-glucoronidase (*Gusb*). Cut-off 1.5-fold absolute threshold depicted by dotted lines. No significance.

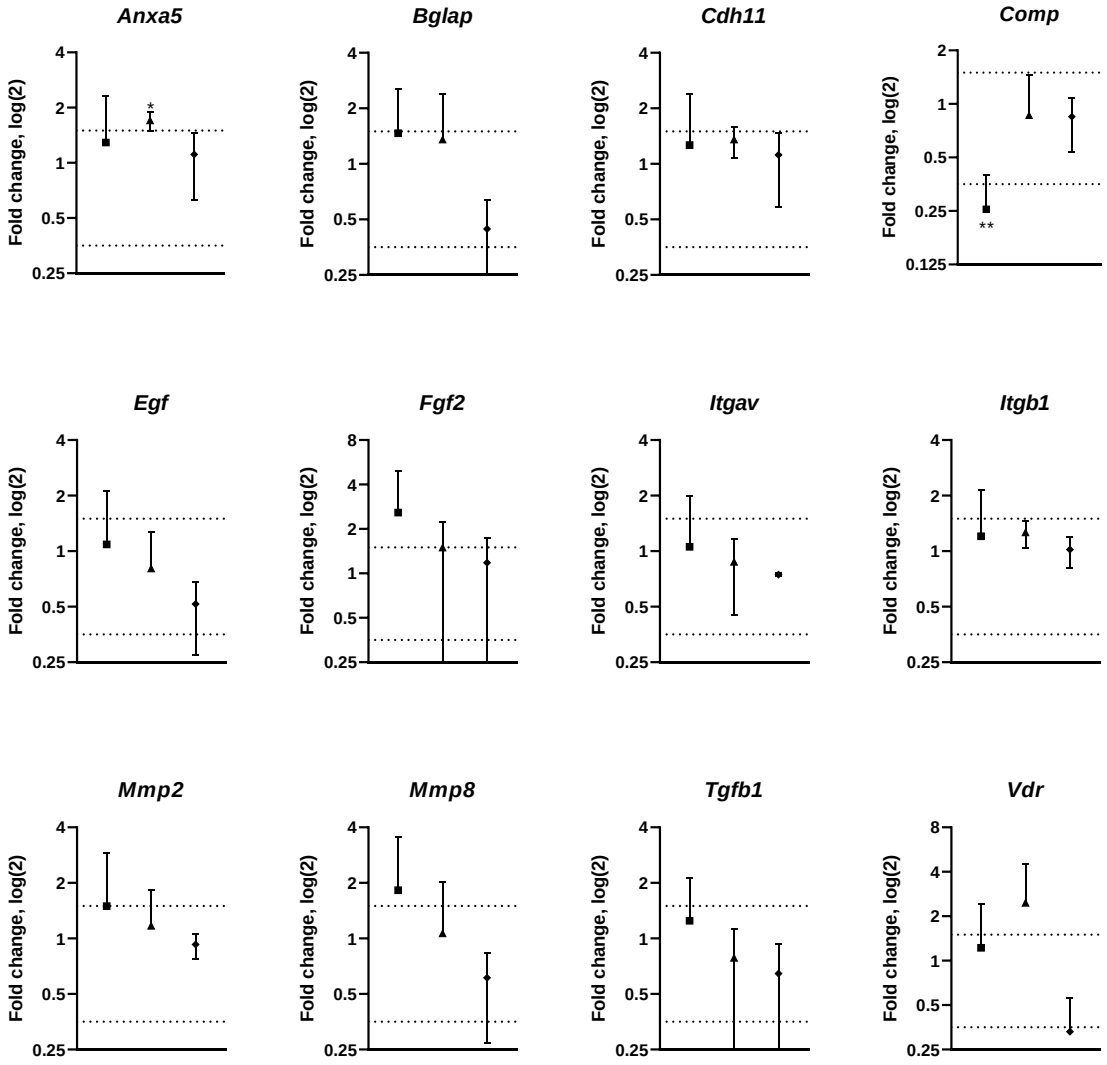

Figure 27 Calcium Ion Binding and Homeostasis Gene *Anxa5* Was Over-expressed in Chow-*foz/foz* Mice; *Comp* Was Under-expressed by HF-WT Mice at 13 Weeks of Age

RT-qPCR array data expressed as fold change relative to chow-WT control ($2^{-\Delta\Delta}$CT) ■ HF-WT, ▲chow-*foz/foz*, ◆HF-*foz/foz (n=3-4/group),* performed in unicate. Data presented as mean and 95% confidence interval (error bars). 2-tailed t-tests, reported from Qiagen© Gene globe data analysis software. All data normalised by β-glucoronidase *(Gusb).* Cut-off 1.5-fold absolute threshold depicted by dotted lines. Significance *'*' (p<0.05) '**'(p<0.01).*

EXTRACEULLUAR MATRIX MOLECULES- Proteases

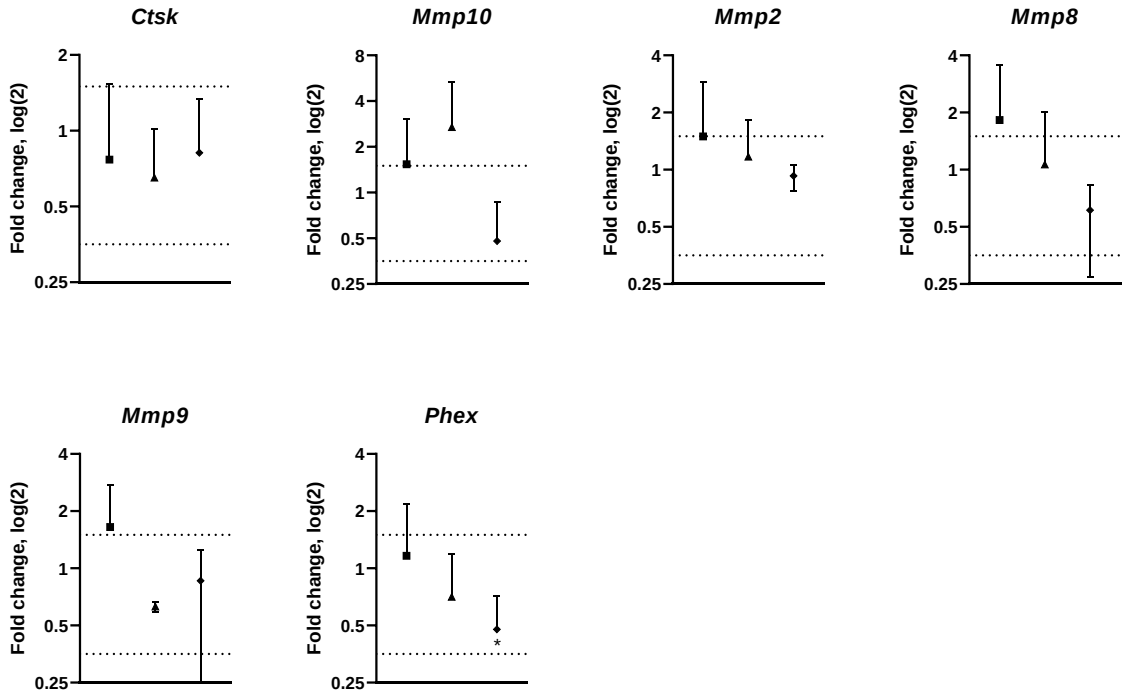

Figure 28 ECM Proteases Gene *Phex* Was Under-expressed by Female HF-*foz/foz* Mice at 13 Weeks of Age

RT-qPCR array data expressed as fold change relative to chow-WT control ($2^{-\Delta\Delta}$CT)■ HF-WT, ▲chow-*foz/foz*, ◆HF-*foz/foz (n=3-4/group),* performed in unicate*.* Data presented as mean and 95% confidence interval (error bars). 2-tailed t-tests, reported from Qiagen© Gene globe data analysis software. All data normalised by β-glucoronidase *(Gusb).* Cut-off 1.5-fold absolute threshold depicted by dotted lines. Significance *'*' (p<0.05) '**'(p<0.01).*

EXTRACEULLUAR MATRIX MOLECULES- Other ECM Molecules

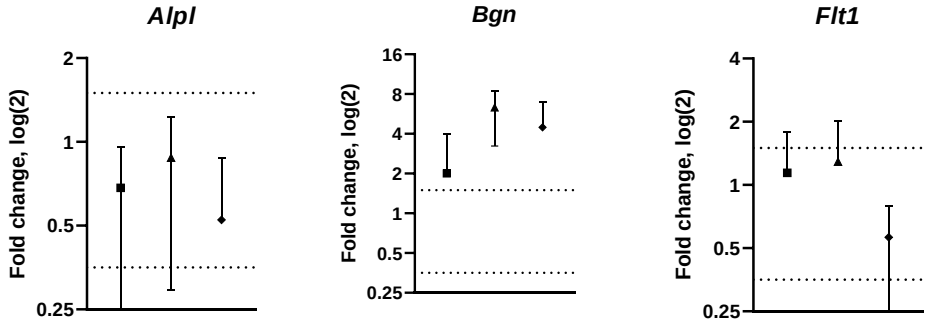

Figure 29 Other ECM Molecule Genes Were Invariantly Expressed by Female NOD·B10 Mice at 13 Weeks of Age

RT-qPCR array data expressed as fold change relative to chow-WT control ($2^{-\Delta\Delta}$CT) ■ HF-WT, ▲chow-*foz/foz*, ◆HF-*foz/foz (n=3-4/group)*, performed in unicate. Data presented as mean and 95% confidence interval (error bars). 2-tailed t-tests, reported from Qiagen© Gene globe data analysis software. All data normalised by β-glucoronidase (*Gusb*). Cut-off 1.5-fold absolute threshold depicted by dotted lines. No significance.

EXTRACEULLULAR MATRIX MOLECULES- Collagens

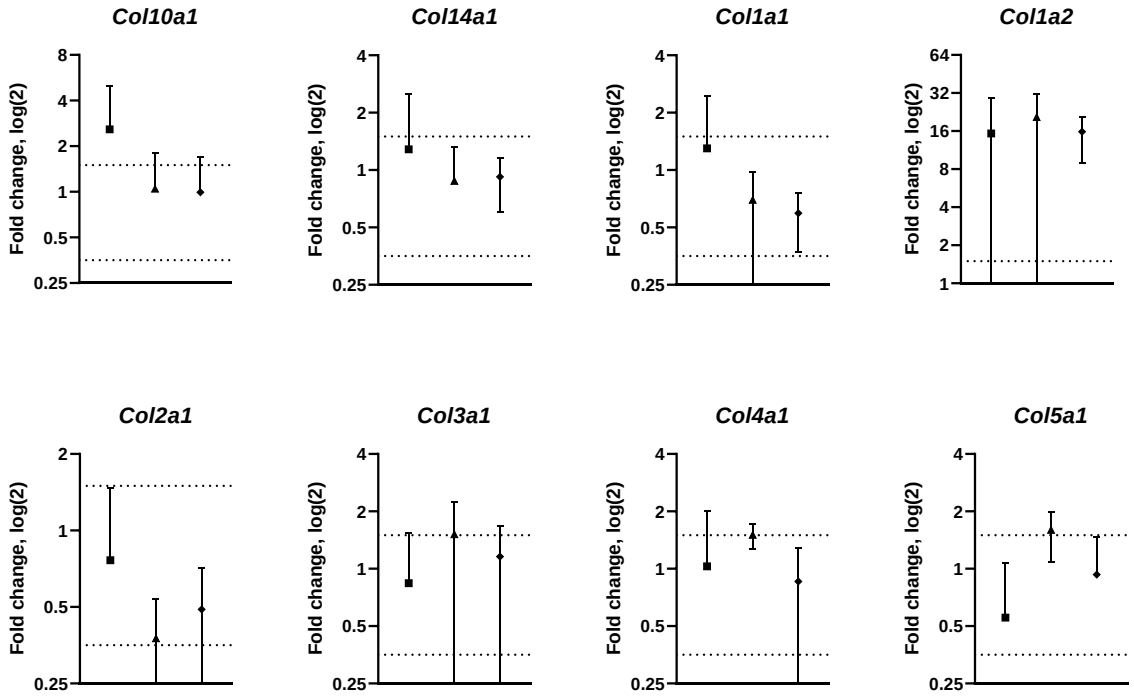

Figure 30 Collagen Genes Were Invariantly Expressed by Female NOD·B10 Mice at 13 Weeks of Age

RT-qPCR array data expressed as fold change relative to chow-WT control ($2^{-\Delta\Delta}$CT) ■ HF-WT, ▲chow-*foz/foz*, ◆HF-*foz/foz* (*n=3-4/group*), performed in unicate. Data presented as mean and 95% confidence interval (error bars). 2-tailed t-tests, reported from Qiagen© Gene globe data analysis software. All data normalised by β-glucoronidase *(Gusb).* Cut-off 1.5-fold absolute threshold depicted by dotted lines. No significance. .

EXTRACELLULAR MATRIX MOLECULES- ECM Protease Inhibitors

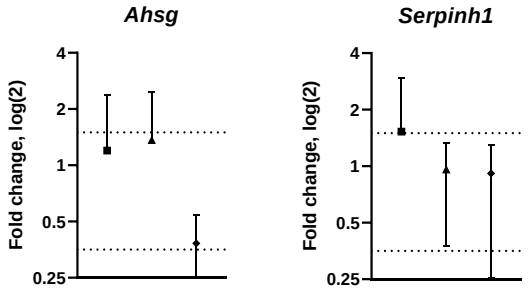

Figure 31 ECM Protease Inhibitor Genes Were Invariantly Expressed by Female NOD·B10 Mice at 13 Weeks of Age

RT-qPCR array data expressed as fold change relative to chow-WT control ($2^{-\Delta\Delta}$CT) ■ HF-WT, ▲chow-*foz/foz*, ◆HF-*foz/foz (n=3-4/group)*, performed in unicate. Data presented as mean and 95% confidence interval (error bars). 2-tailed t-tests, reported from Qiagen© Gene globe data analysis software. All data normalised by β-glucoronidase (*Gusb*). Cut-off 1.5-fold absolute threshold depicted by dotted lines. No significance.

7.2.4 Cell Adhesion Molecule Signalling Was Altered for HF-WT Mice

HF-WT mice under-expressed *Comp* at significance, unlike the *foz/foz* mutants on either diet (Figure 32). Cell-cell adhesion and Cell-ECM adhesion genes were not statistically varied across the NOD·B10 cohort at 13 weeks of age (Figures 33, 34). Whilst statistically significant, *Cd36* was deemed a biological outlier that exceeded variation across the sample space disqualifying this result from biological interpretation.

Integrin genes (*Itg2a, 2b, a3, am, av)* and bone matrix protein gene *Fn1* were not differentially expressed, suggesting that osteoblast, osteoclast and chondrocyte adhesion capabilities were indiscriminate by NOD·B10 feed nor genetic assignment. The anti-osteoprogenitor *Tnf* gene levels were not detected at significance, however appeared lowest amongst diabetic mice, alike the expression pattern of target *Igf1*, whereby neither reached significance. These results further supported the invariant osteoclast profile across the regime, without increased *Rankl* or *Nfkb* transcription activity within the femur.

7.2.5 Growth Factor Signalling Was Varied for Chow-*foz/foz* Mice

Amongst osteogenic growth factor genes, *Fgf1* was solely over-expressed in chow-*foz/foz* mice by the array (Figure 35). Other growth factors were not differentially expressed across the cohort. *Csf2* was detected at significance, attributed to the substantial variation depicted by the confidence interval error bars which indicated disqualification from biological interpretation. Other osteoblastic proliferative genes (*Csf3, Pdgfa, Vegfa, Vegfb*) were not expressed at statistical significance, which corroborated the absence of bone lesions or over-active remodelling. This supported the osteoblast quiescent and osteoclast indifferent transcript findings of diabetic HF-*foz/foz* mice.

7.2.6 Transcription Factor Signalling Was Differential for Diabetic Mice

HF-*foz/foz* mice exclusively under-expressed *Runx2* transcription factor at statistical significance (Figure 36). All other osteogenic transcription factors were not statistically differentiated by PCR array. The under-expression of the master osteoblastic transcription factor suggested initial changes in the femur of the obese, hyperglycaemic and hyperinsulinemic NOD·B10 mouse.

CELL ADHESION MOLECULES- Other

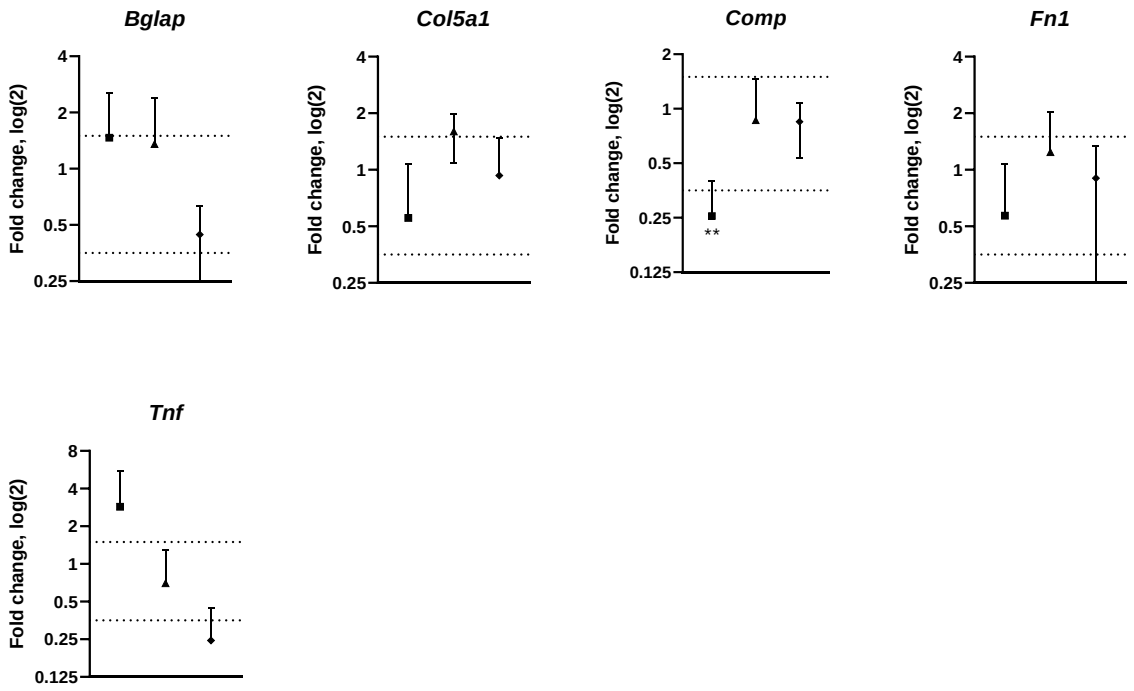

Figure 32 Other Cell Adhesion Molecule Gene *Comp* Was Under-expressed by Female HF-WT Mice at 13 Weeks of Age

RT-qPCR array data expressed as fold change relative to chow-WT control ($2^{-\Delta\Delta}$CT) ■ HF-WT, ▲chow-*foz/foz*, ◆HF-*foz/foz (n=3-4/group)*, performed in unicate. Data presented as mean and 95% confidence interval (error bars). 2-tailed t-tests, reported from Qiagen© Gene globe data analysis software. All data normalised by β-glucoronidase *(Gusb).* Cut-off 1.5-fold absolute threshold depicted by dotted lines. Significance *'*' (p<0.05) '**'(p<0.01).*

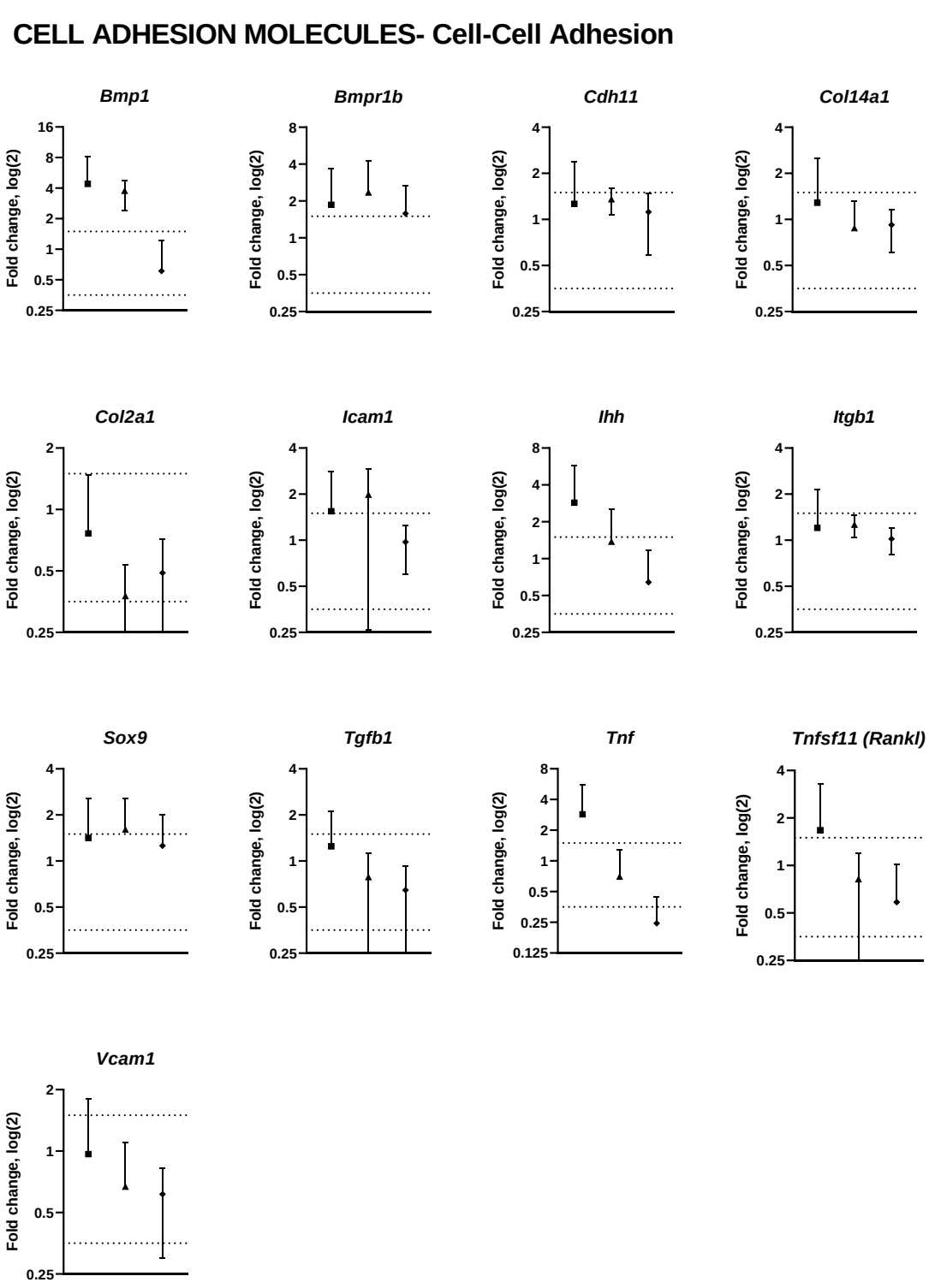

Figure 33 Cell-Cell Adhesion Genes Were Invariantly Expressed by Female NOD·B10 Mice at 13 Weeks of Age

RT-qPCR array data expressed as fold change relative to chow-WT control ($2^{-\Delta\Delta}$CT) ■ HF-WT, ▲chow-*foz/foz*, ◆HF-*foz/foz (n=3-4/group)*, performed in unicate. Data presented as mean and 95% confidence interval (error bars). 2-tailed t-tests, reported from Qiagen© Gene globe data analysis software. All data normalised by β-glucoronidase (*Gusb*). Cut-off 1.5-fold absolute threshold depicted by dotted lines. No significance.

CELL ADHESION MOLECULES- Cell-ECM Adhesion

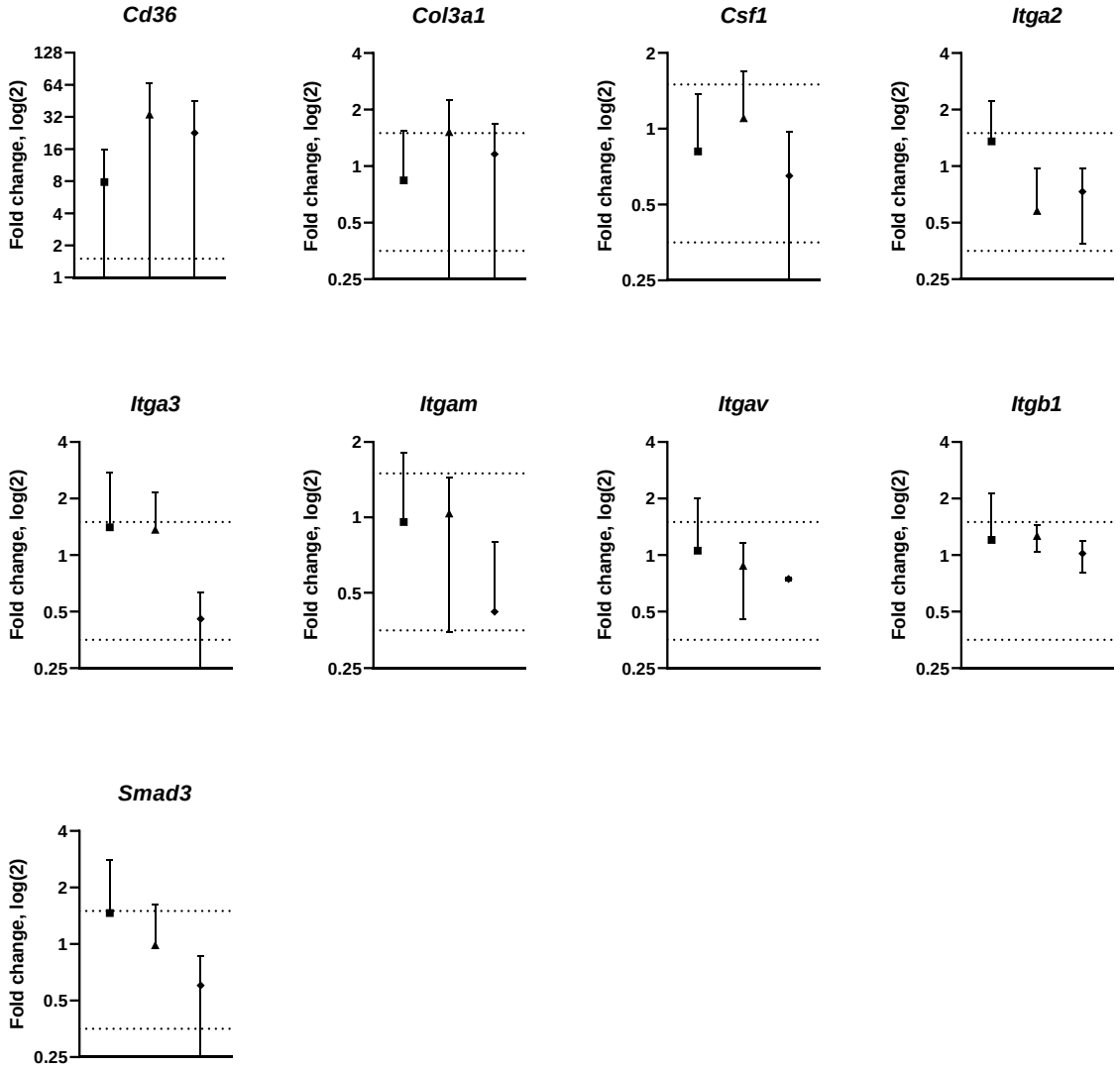

Figure 34 Cell-ECM Adhesion Genes Were Invariantly Expressed by Female NOD·B10 Mice at 13 Weeks of Age

RT-qPCR array data expressed as fold change realtive to chow-WT control ($2^{-\Delta\Delta}$CT) ■ HF-WT, ▲chow-*foz/foz*, ◆HF-*foz/foz (n=3-4/group)*, performed in unicate. Data presented as mean and 95% confidence interval (error bars). 2-tailed t-tests, reported from Qiagen© Gene globe data analysis software. All data normalised by β-glucoronidase (*Gusb*). Cut-off 1.5-fold absolute threshold depicted by dotted lines. Significance *'*' (p<0.05) '**'(p<0.01).*

GROWTH FACTORS

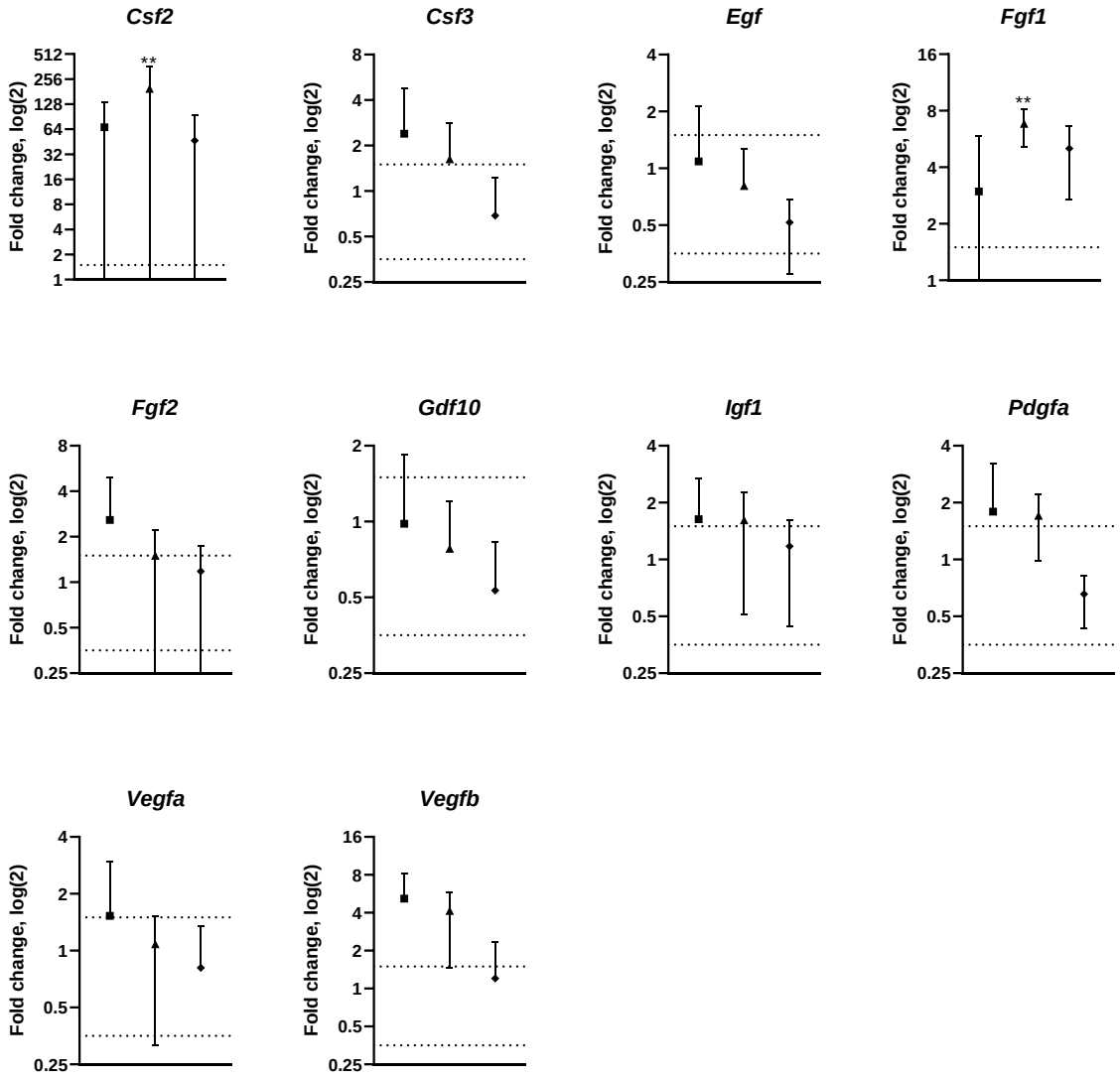

Figure 35 Growth Factor Gene *Fgf1* Was Over-expressed in Female Chow-*foz/foz* Mice at 13 Weeks of Age

RT-qPCR array data expressed as fold change relative to WT-chow control ($2^{-\Delta\Delta}$CT) ■ HF-WT, ▲chow-*foz/foz*, ◆HF-*foz/foz* (*n=3-4/group*), performed in unicate. *Csf2* is statistically detected however biologically insignificant. Data presented as mean and 95% confidence interval (error bars). 2-tailed t-tests, reported from Qiagen© Gene globe data analysis software. All data normalised by β-glucoronidase (*Gusb*). Cut-off 1.5-fold absolute threshold depicted by dotted lines. Significance *'*' (p<0.05) '**'(p<0.01).*

TRANSCRIPTION FACTORS

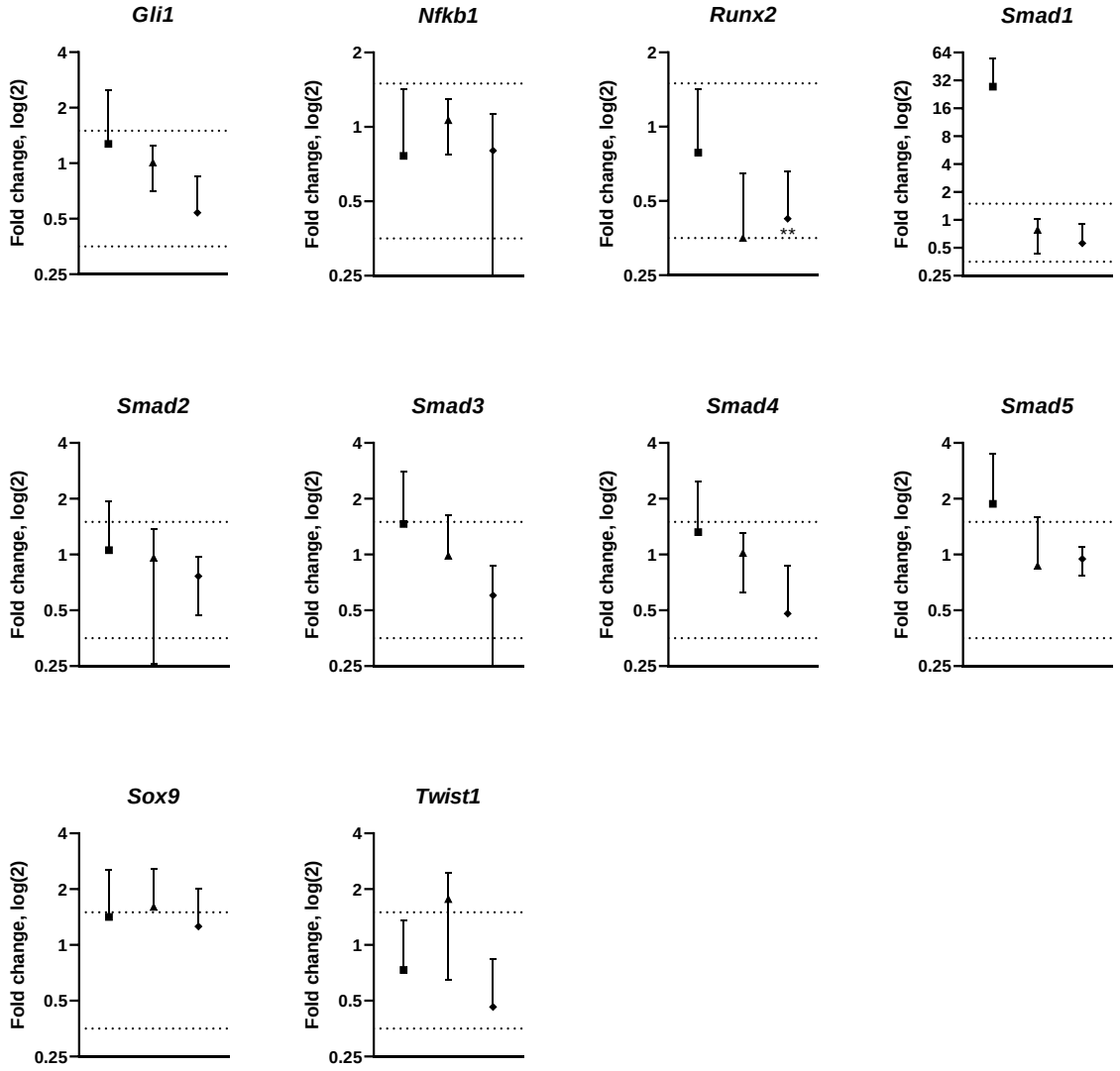

Figure 36 Transcription Factor Gene *Runx2* Was Under-expressed in Female HF-*foz/foz* Mice at 13 Weeks of Age

RT-qPCR array data expressed as fold change relative to chow-WT control ($2^{-\Delta\Delta}$CT) ■ HF-WT, ▲chow-*foz/foz*, ◆HF-*foz/foz (n=3-4/group),* performed in unicate. Data presented as mean and 95% confidence interval (error bars). 2-tailed t-tests, reported from Qiagen© Gene globe data analysis software. All data normalised by β-glucoronidase *(Gusb).* Cut-off 1.5-fold absolute threshold depicted by dotted lines. Significance *'*' (p<0.05) '**'(p<0.01).*

7.3 FGF1 Levels Were Putatively Elevated in HF-*foz/foz* Mice by ELISA Result

ELISA was performed on NOD·B10 serum samples obtained at sacrifice to detect circulating protein levels. The selected FGF1 was metabolically implicated for systemic changes in circulation, supported by the femoral distinction between *Fgf1* mRNA levels of *foz/foz* mutants.

Neat samples were not determined by assay therefore not presented. Both 1:2 and 1:4 dilution results are presented from performance of 4 mice per group (Figure 37). Statistical analyses were contraindicated by the lack of determined results by each group. Aside from the HF-WT group for which 1:2 results were not obtained, the final concentrations of 1:2 and 1:4 dilutions (from the same animal) were in agreement.

These preliminary data suggested the magnitude of FGF1 protein in circulation was much higher amongst HF-*foz/foz* NOD·B10 mice. The conceptual discrepancy between femoral *Fgf1* levels and peripheral FGF1 added to the broader dialogue of using indirect serum markers to infer bone metabolism.

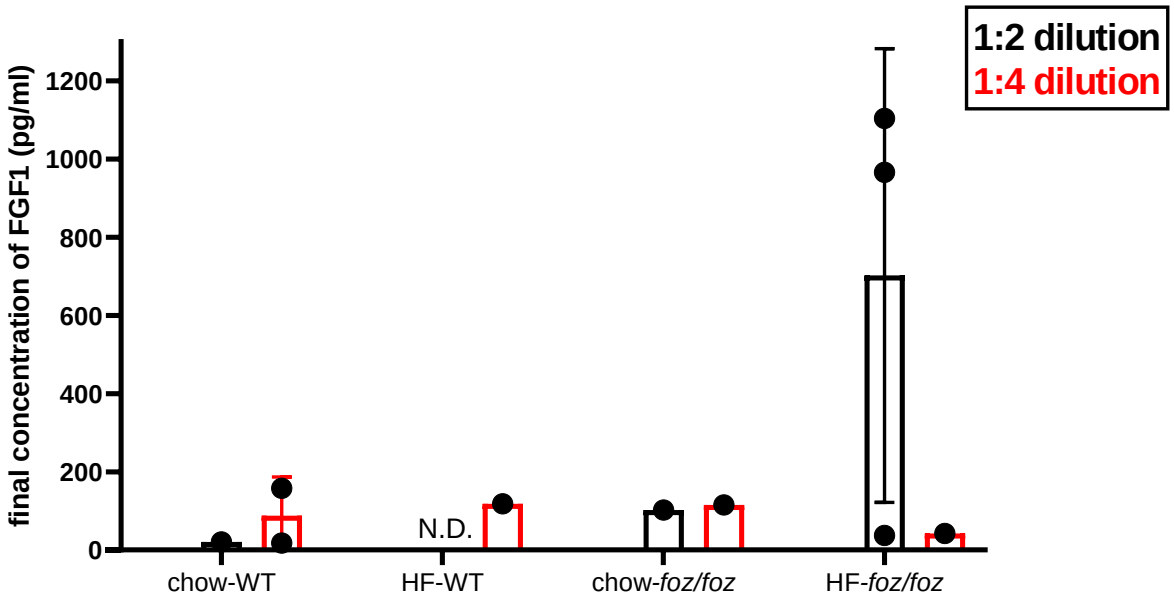

Figure 37 Interpolated Concentration of FGF1 from Serum of Female NOD·B10 Mice

ELISA data presented as points with standard deviation (where obtained) represented by error bars. 'N.D.' no result determined for the group. Black bars represent results obtained from 1:2 serum dilution. Red bars represent results obtained from 1:4 dilution. All results obtained in duplicate *(n=4/group*). Data could not be statistically analysed due to inadequate result determination.

7.4 Discussion of Osteogenesis Profiling

7.4.1 Diabetic Mice Exhibited a Quiescent Femoral Transcript

The most profound result of the obese diabetic group was the under-expression of *Runx2* mRNA. The master transcription factor is combinatorial in elaborate signalling sequences permitting osteogenesis. *Runx2* is essential for osteoprogenitor differentiation from the MSC pool. Levels rise with early induction of osteoblastogenesis, and then fall as osteoblasts mature permitting osteocyte differentiation.

Fgfr2 expression is specific to intensive endochondral growth and subsides with physeal senescence. This spatial and temporal correlation of FGFR2 is clearly defined in rats and humans with growth plate closure [405]. This is plausible yet less definitive in mice as the physes remain open and growth attenuates over time. By 13 weeks of age, endochondral ossification may have peaked for the diabetic NOD·B10 group, consistent with *Runx2* modulation of *Fgfr2* expression. Only the diabetic group reported significant under-expression of either gene supporting a pathological change to the femoral transcript.

Fgfr2 reciprocally modulates *Runx2*, and whilst the expression order cannot be determined by PCR, common under-expression substantiated a quiescent profile unlike the non-diabetic groups. *Fgfr2IIIc*$^{-/-}$ null mice exhibited an exaggerated phenotype of impaired ossification and low bone mass with failure to express sufficient *Runx2* to recruit bone matrix protein genes [406]. These downstream targets were not under-expressed at significance amongst the NOD·B10 cohort, despite a trend of lower relative expression amongst the diabetic group. This premise suggests a lower potential for osteoblast differentiation from MSC progeny due to the common under-expression of reciprocally inductive *Runx2* and *Fgfr2* genes.

Igf1r triggers *Runx2* transcription, under-expressed in the obese, diabetic mice strengthening the case for osteoprogenitor repression. The IGF1 axis is critical to mechanotransduction, stimulating osteoblast differentiation and survival by *Runx2* promotion. Fluid shear stress models of bone cell cultures revealed IGF1R blunting to the ligand under static incubation [407]. Whilst the *foz/foz* hypothalamic ciliopathy promotes physical underactivity, obesity mass likely negates the reduced mechanical loading and fluid flow from enhanced sedentarism. Supporting this conjecture, deliberately unloaded rats revealed under-expression of *Itgav* and *Itgb3* accompanying osteopenia, which was not observed amongst NOD·B10 mice [408].

In both mature and immature rodents, IGF1R is crucial to facilitate PTH stimulation of precursors and respond to anabolic cues [409, 410]. Young female mice showed profound trabecular deficits with loss of osteoblast-specific *Igf1r* that failed to gain mature mineralisation competency [411]. The critical loss of bone infrastructure with precocious skeletal impairments distinguishes earlier onset diabetes from later subversion of a normal bone mass in older age diabetes. Earlier reductions in *Igf1r* contributed to a static differentiation potential in tandem with *Runx2* and *Fgfr2* under-expression measured in 13 week old HF-*foz/foz* mice.

Adjunct to the ossification deficits implied by an inert osteogenic potential, matrix mineralisation gene *Phex* was also under-expressed by the obese, diabetic female mice. Expressed by osteoblastic cell types, PHEX responds to PTH to inhibit matrix mineralisation [412]. Rats receiving recombinant human IGF-1 therapy revealed concomitant increase in *Phex* and *Ocn* feedback to the upregulated system [413]. It is consistent with our findings that *Igf1r* reduction coincided with significant under-expression of *Phex.* It remains to be established whether diabetic cells are biochemically resistant to PTH, or indirectly suppressed by a loss of selection and priming from the MSC progeny.

In defiance of the under-expression findings, HF-*foz/foz* mice reported over-expression of *Bmp5* at 13 weeks of age in femoral bone. This gene was seemingly over-expressed by all of the experimental groups yet did not reach statistical distinction in single treatment profiles. Supplementary to the osteopotent Bmp genes, an endemic role for *Bmp5* is not clear. BMP5 expression in hypertrophic chondrocytes is promoted by insulin to trigger p38 MAPK differentiation of osteoblasts [414]. *Bmp5* over-expression at the growth plate is known to contribute to heterotopic ossification (HO), complicit with other aberrant *Bmp* genes [415].

Diabetic dysregulation of bone metabolism is known to contribute to ossification disorders such as diffuse idiopathic skeletal hyperostosis (DISH) [416]. DISH includes pathologically ossified tendons and ligaments, whilst a *Bmp5* mutation creates entheseal deficits [417]. The coincidence of seemingly deranged *Bmp5* signalling in the *foz/foz*-diabetes model is cause for interest in a future study. This unexpected finding is orthopedically relevant as DISH patients form osteophytes and develop undesired HO after THA [418].

Hyperglycaemia is known to reduce *Runx2* expression, which differentiated HF-*foz/foz* mice from chow-fed mutants [419]. By lowering the *Runx2* basal expression in the diabetic group, the potential threshold for successful osteoblast transcription is markedly impaired.

Contributions from *Fgfr2, Igf1r* and concomitant *Phex* indicated diversion of osteoprogenitors from MSC lineage. Without the pro-osteogenic buffer of *Runx2* sensitisation, precursor populations can be detoured to adipogenic fate commitment exacerbated by HFD [420]. Adaptive adipose hypertrophy in the bone marrow supports an accelerated medullary expansion and accelerated aging of the vulnerable trabecular tissue. These results offer some concurrence to the clinically observed maladaptive type 2 diabetic bone disorder.

Longstanding human diabetes patients exhibit pathological increases in PPAR-γ, TNF-α, SOST and RANKL signifying a corrupted bone microenvironment by lipotoxicity, rising inflammation and osteoclastic predominance [357]. Without multiple points testing, the staging of diabetes on bone adaptions is yet to be resolved. The multi-modality of *Runx2* complicates a consecutive mechanism at this time, however provides insight to early changes in bone integrity with compounding ramifications in due course. For example, aged *Runx2* heterozygous knock out mice cannot recover ablated trabecular deficits [421]. Earlier downplay of crucial osteoblast selection genes driven by younger onset diabetes pre-empts the intensifying downturn of longstanding disease.

Before hyperglycaemic suppression of *Runx2*, rising insulin levels likely promoted osteoanabolic growth, inferred from the abundance of trabeculae alike non-diabetic mice. The increased bone surface area requires more osteoblasts to maintain the bone surface, spatially regulated by mature osteocyte and BLC populations. Accelerated proliferation may have exhausted the pool of sensitised osteoprogenitors. Whilst supported under higher insulin conditions, ensuing hyperglycaemia and chronic inflammation reduce the osteoblastic differentiation potential as detected by PCR array, and favour adipogenic subversion of the MSC niche. Stagnation of the osteogenic pool would require alternative strategies to amplify the limited surface area to uphold trabecular homeostasis.

Lower fidelity *Runx2*-mediated transcription and under-expression of *Fgfr2, Igf1r* and *Phex* supported premature quiescence of osteogenesis in the femur. Aberrant *Bmp5* transcript suggested metabolic derangement without overt trabecular pathology. Even with lower mineralisation potential, greater trabecular surface area could permit a greater osteoblast cell density. The enhanced mineralisation surface supported the equivalent BMD to non-diabetic mice at 13 weeks of age. Broader disparities in the aftermath of compromised *Runx2* induction would likely emerge with longer duration of disease progress and mouse aging in this model. These findings present a reference point to orient longer investigations

to delineate the tipping point in bone homeostasis under diabetes which remains a critical gap in the orthopaedic discipline.

7.4.2 HF-WT Mice Exhibited Accessory Gene Aberrance

HF-WT NOD·B10 mice measured lower relative *Comp* expression levels than chow-WT littermates. COMP (Thrombospondin 5) is a cartilage-specific matrix protein, responding to growth-related mass increases promoting chondrocyte proliferation [422]. This project reported under-expression of femoral *Comp* despite equal mean body weight to WT-chow mice. These animals varied by diet only, as blood glucose and plasma insulin levels were equivocal at 13 weeks of age.

Chow-*foz/foz* mice also achieved similar body weight to HF-WT (but heavier than chow-WT mice) yet did not share the expression trend, convincingly defying the load bearing explanation of the *Comp* transcript result. Amongst WT mice, the possibility that HF-feeding curbed peak growth and corresponding lean mass gains was considered. Free fat mass gains driven by fuel surfeit hold less mass than equivalent muscle tissue likely masked by crude body weight measure. Coupled with HFD-induced sarcopenia, *Comp* may have been under-expressed to prevent unnecessary proliferation. Compliance of the remaining 83 osteogenic genes panelled in the array implied osteogenic homeostasis at the transcript level, relative to chow-WT NOD·B10 mice.

In patients with pathological COMP mutations, *COMP* mRNA was accumulated in trabecular osteoblasts [423]. Ossification defects from 3 weeks of age in mutant COMP mice also persisted in trabecular features to 4 months [424]. This suggested that the transcriptional underactivity of *Comp* amongst HF-WT mice was negligible to bone microstructure by the absence of pathology detected in the trabecular parameters. The inclination for consolidated femoral trabeculae did not sufficiently alter BMD nor BV/TV amongst 13 week old HF-fed WT mice.

7.4.3 Chow-*foz/foz* Mice Exhibited A Metabolically Active Transcript

Unlike HF-fed mice, the chow-*foz/foz* mice detected relative over-expression of *Fgf1* and *Anxa5* genes at statistical significance. Mitogenic FGF1 is expressed under stress conditions, a prototype ligand signalling through all FGF receptors inducing cell division. This trauma response was observed in inflammatory fracture conditions, with up-regulation of FGF1 that triggered osteogenic and angiogenic repair [425]. Intravenous *Fgf1* therapy

to ovariectomised and sham-operated rats promoted similar osteoanabolic corrections to iatrogenic bone loss [426].

Chow-*foz/foz* mice do not reflect an osteoanabolic state as explanation of the raised *Fgf1* expression, despite the tendency for thinner trabeculae. Without osteoblast induction nor osteoclast suppression detected by the array, the metabolic stress of the *foz/foz* mutation was considered. Overweight and hyperinsulinemia phenotype at 13 weeks of age distinguished the mutants from HF-WT mice, despite indifferent skeletal findings. Taken together, this suggested a mounting stress response in the bone implied by *Fgf1* over-expression was yet to drastically alter the skeletal microstructure of the femur.

Whilst chow-*foz/foz* mutants maintained an identical bone phenotype to chow-WT littermates, they were differentiated by over expression of *Anxa5* in the mutant group. *Anxa5* is a matrix vesicle protein gene, facilitating hydroxyapatite propagation on osteoid surfaces. As a calcium-dependent protein, ANXA5 is linked to FGF1-mediated intracellular calcium regulation [210, 427]. Phosphatidyl serine enables FGF1 export under cell stress conditions [428]. The acidic phospholipid is integral to matrix vesicle membranes, combining with amorphous calcium phosphate and ANXA5 to enhance nucleation [429]. This association was not clear in the NOD·B10 mice, as further work of *Anxa5* and *Fgf1* gene expression had not been published. However, in light of the available evidence, the endemic over expression of *Fgf1* and *Anxa5* in murine femur suggested a skeletal compensation for raised insulin levels and increased body mass invoked by *foz/foz* mutation.

7.5 HF-*foz/foz* Mice May Have Expressed Elevated Serum FGF1 with Diabetes Emergence

In an attempt to differentiate the profiles of NOD·B10 *foz/foz* mice by diet and corresponding disease state FGF1 was selected for protein analysis. Equivalent hyperinsulinemia yet differential blood glucose levels implicated metabolic differences between the insulin resistant chow-fed mice, and the obese diabetic HF-fed mice which warranted investigation of FGF1 expression.

FGF1 requires intact insulin signalling in target tissues such as bone. The suppressive transcript of the diabetic group femur revealed by PCR insinuated abolished insulin signalling, in accord with established hyperglycaemia. As NOD·B10 mice had not been previously characterised for osteogenic expression, clues to the metabolic strategy in bone were posited to lie in systemic changes present in serum.

The ELISA result of this project must be coarsely interpreted with limited detection of the antigen which prevented statistical analysis. In consult with the broader literature, the profound increase in serum FGF1 levels of the HF-*foz/foz* NOD·B10 mice was plausible.

FGF1 is the primer of pre-adipocytes to PPAR-γ, facilitating terminal differentiation. FGF1$^{-/-}$ mice are therefore insulin resistant with loss of PPAR-γ signal transduction, whereas WT mice are insulin receptive [430]. Recombinant FGF1 administration to FGFR1$^{-/-}$ mice corrected DIO and hyperglycaemia preventing weight gain, low bone mass and hepatic steatosis via the FGF1-PPAR-γ axis [431].

Raised circulating levels of FGF1 have emerged as a distinctive feature of the homeostatic attempt to regain insulin sensitisation. Amongst BMI-matched subjects, T2DM patients revealed higher serum FGF1 levels than non-diabetics [432]. This finding was also supported in non-diabetic obese children and adolescents with insulin resistance strongly correlated to raised serum FGF1 levels [433].

Both HF-DIO and *ob/ob* male C57/BL6 mice report increased *fgf1* mRNA expression and up-regulated epididymal PPAR-γ2, C/EBP-α and AP-2 pro-adipogenic strategy in response to nutritional stress [434]. Extrapolating from the literature, there appears a distinction between obesity and diabetes on the basis of insulin state irrevocably lost in obesity-borne T2DM. These studies suggest a clinical avenue for FGF1 in diabetes and the preceding insulin resistance in the human population.

In opposition, a study of T2DM patients, 7 week old and 20 week old *db/db* mice reported lower FGF1 levels than non-diabetic comparators [435]. This contrast is attributed to further progressed T2DM in longstanding and/or managed human patients, and the accentuated severity of *db/db* disease. No publications on advanced diabetes and the inverted parabola of insulin secretion pertaining to FGF1 levels were found. This limited comment on the range of values detected in this group.

We would expect chow-*foz/foz* mice to have raised FGF1 reflecting this insulin resistance with marked hyperinsulinemia and corpulence measured at 13 weeks of age. Whilst inconclusive, the serum assay amongst NOD·B10 mice favoured the association consistent with obesity-borne T2DM as the HF-*foz/foz* mice achieve markedly higher serum FGF1 levels with disease onset.

As FGF1 signalling is perturbed by insulin resistance, the elevated detection of FGF1 in obese diabetic mouse serum implicated a dysregulated adipose capacity. The likelihood of

adipose ciliopathy derived from *Alms1 (foz/foz)* mutation must be considered in the implied FGF1 stress response. Without prior investigation of the *foz/foz* influence, surrogate mouse models are discussed. MSC progeny including adipocytes, osteoblasts and osteocytes are adenylyl cyclase 3 (AC3) positive [436]. The $AC3^{-/-}$ null mutant is unable to convert ATP to c-AMP, compromising primary cilia protein associations resembling *foz/foz* mice phenotype and behaviour [437].

The *Alms1* gene trapped mouse sustains the concept of pre-adipocyte ciliopathy from impaired GLUT-4 translocation inhibiting adipose differentiation [370]. In concert with *Alms1* gene trapped mice, $AC3^{-/-}$ failure to traffic glucose and permit ciliary elongation prevents the terminal differentiation of adipocytes [438]. This finding has not been published in osteoblast cell types and requires further investigation for contributions to the altered bone phenotype of HF-*foz/foz* mice in this project. Without statistical power to compare experimental groups, no further contrasts of *foz/foz* versus WT can be made from the current data.

In light of the related adipose deregulatory mechanisms, it is plausible the *foz/foz* mutation permits adipose ciliopathy, most pronounced in the obese group with highest adipose tissue levels, and accentuated by dietary stress driving co-morbid T2DM. On the contrary, adipose restriction due to failed expansion was not detected by Dagpo at 12 weeks of age in diabetic, obese NOD·B10 nor non-diabetic, obese BALB/c under identical genetic and dietary stress [353]. It is therefore unclear whether a ciliopathy was established in NOD·B10 *foz/foz* population without further investigation. Even without ciliopathy, the evidence for adipose dysregulation from exceeding FGF1 levels is compelling. It remains to be resolved how ciliopathy contributes to metabolic inflammation by raising FGF1, or synergistically influencing the feedforward FGF1 response.

Given the discrepancy with successfully detected circulation and peripheral FGF1 therapy, it is unlikely that FGF1 is not endogenously expressed in serum. Troubleshooting the assay, serum FGF1 levels were notoriously undetected in other studies, unlike non-serum samples [439]. Serum FGF1 levels were minimally detected in a study of obese and non-obese patients, with successful measurement in only 5 of 37 samples [440]. A second study in a metabolically healthy cohort was also unable to detect serum FGF1 levels using an alternative branded kit [441]. This may speculatively support the low and undetectable levels amongst relatively healthier WT NOD·B10 mice, however cannot be confirmed without further validation. Together these findings underscore difficulties in serum detection of FGF1.

In this project, attempts to optimise the assay by neat plating of the sample groups (which were undetected at the recommended 1:2 dilution) were unsuccessful. Where 1:4 dilutions were available, the final concentration of FGF1 was acceptable to the 1:2 dilution result. However in most cases, only duplicate results at a single dilution were detected.

Interestingly, studies reporting detectable serum FGF1 levels measure in ng, rather than pg per ml. The selected assay should therefore have been sensitive to this range. On the basis of incomplete validation, the content or presence of FGF1 expression in NOD·B10 WT mice and chow-*foz/foz* mice was neither confirmed nor refuted. More work is required to resolve this assay, implicated by the preliminary finding of this project and the wider disciplinary interest.

8 Discussion and Future Directions of the Project

8.1 Overview of the Thesis

We found evidence of diabetic trabecular thinning and a tendency (albeit statistically insignificant) for a greater number of trabeculae despite equivalent BMD to non-diabetic mice. Osteoporosis was contraindicated at 13 weeks of age at the distal femur, which suggested an alternative adaptation under early diabetes. The gene expression data established precedent for osteoprogenitor dormancy and a secondary downturn of mineralisation. Together these results proposed an expansion of the available surface area of trabecular bone. This adaptation was not common with the obese diabetes-protected BALB/c mice, which endorsed a diabetes-specific bone response.

Bone strength is a consequence of bone status: the connectivity of the tissue, its relative age and composition. Dysregulation of homeostasis and repair leads to an inferior structure of compromised skeletal integrity and fracture susceptibility. T2DM is known in both humans and rodents to impair bone resilience; however the heterogeneity of findings leaves many details unresolved. The transition to chronic T2DM and temporal adaptations of bone require investigation.

To address the orthopaedic gap, genetic susceptibility and diet as catalysts for earlier onset disease were utilised to examine trabecular bone indices. Younger aged, non-mated female mice were employed in this study to establish evidence of earlier bone microstructural changes supported by molecular signalling. Without the confounders of conventional aging studies including substantial AGEs, cortical thinning, and collagen impedance this project sought to detect changes in murine femur.

Trabecular tissue is younger and less mineralised than enduring cortical bone. In this time, BMD is a coarse average of the two compartments: a limitation now articulated for fracture risk prediction tools. This prominence is apparent at trabecular sites with the divergence of diabetic hip and spinal fragility, even in cases of obesity. Endemic to the metabolic adaptations under pre- and diagnosed T2DM, trabecular bone is highly implicated and subject to adaptive compensation which we sought to detect in 13 week old mice.

This project advocates that the mode of mature skeletal acquisition and its continued maintenance which dictate bone integrity, rather than crude gain or loss of mass, bone features and cell populations. This is the true resolution of refining the BMD parameter with bone qualities in orthopaedic practice.

The baseline provided by this project serves as an insight to the initial diabetic-mediated changes which may be obscured in older cohort findings, masked by the inevitable remodelling process. This is especially implored by the emergence of younger onset diabetes prior to human middle age and more alarmingly, during time of peak bone growth. The subtleties of microarchitecture and accompanying osteogenic profile provided the extent of bone response to diet and mutation challenges in the diabetes susceptible and diabetes resistant mice which were not captured with conventional BMD measurement alone.

8.2 General Discussion

By the 9 week regime, mice achieved the predicted phenotypes of the *Alms1 (foz/foz)* model. The strain-specific susceptibility to insulin resistance was evident for NOD·B10 homozygous mutants. BALB/c *foz/foz* littermates achieved mildly raised plasma insulin levels in contrast, despite group-matched mean body weight across strains. Diet divided *foz/foz* mutants, as HF feeding promoted greater body weight increase than chow. Thus both strains under combined diet and genetic stress achieved obesity by 13 week end point.

Importantly, of the 8 experimental groups only NOD·B10 mice of combined challenge HFD and *foz/foz* mutation reported hyperglycaemia additive to marked hyperinsulinemia satisfying type 2 diabetic criteria. WT mice of both strains provided healthy controls, without phenotypic distinction by diet assignment. The *foz/foz* mutation drove metabolic consequences, stratified by strain into obese, diabetic NOD·B10 and obese BALB/c which delineate diabetic-specific bone qualities from obesity.

Across the spectrum of lean to obese BALB/c mice, no differences in trabecular microarchitecture were measured for the distal femur. BMD and cortical parameters were also uniform across the strain irrespective of diet nor genetic stress. Surprisingly, BALB/c mice exhibited strikingly different trabecular microarchitecture to NOD·B10 mice. This finding was unexpected as NOD·B10 microstructure had not been previously published. The inter-strain effect precluded comparisons across strains for matched treatments and BALB/c mice were not studied further in this project.

In contrast, NOD·B10 mice revealed some microarchitecture differences at the distal femur. Amongst the available group size, differences between HF-fed mice by genotype were detected by Mann-Whitney U test. The implication for thinner trabeculae amongst HF-*foz/foz* mice was statistically supported, with secondary tendency for more trabeculae than

HF-WT mice, albeit statistically insignificant. Chow-fed mice did not reveal trabecular alterations irrespective of genotype.

BMD and bone volume fraction were group-wise invariant, in support of the clinical T2DM paradox. As a composite measure, cortical parameters were also compared, without difference between groups which emphasised the trabecular contribution to bone adaptation at the distal femur in younger mice. Taken together, these findings underscored the inherent adaptation of trabeculae comparative to cortical bone compartment at 13 weeks of age.

As microstructure largely agreed amongst young mice, PCR array was performed to ascertain how osteogenic signalling in the femur may have been influenced under the hyperinsulinemia and hyperglycaemia of established T2DM amongst HF-*foz/foz* mice and single treatment groups. Profiling of the whole femur detected greatest differential signalling amongst the diabetic cohort.

Curiously diabetic mice over-expressed supplementary *Bmp5* with some inference to metabolic anomaly. Under-expression of osteoblast differentiation genes (*Igf1r*), overlapped with ossification (*Fgfr2*) and bone metabolic processes (*Phex*) emphasised the suppression of early osteoprogenitors commitment from the MSC lineage. Under-expression of the key orchestrator *Runx2* without significant under-expression of signature osteoblast genes suggested in the first instance progenitors were alternatively diverted. It is speculated from these results and broader literature that adipogenic subversion may have shifted the threshold for osteogenic selection.

HF-WT mice, whilst reporting thicker trabeculae measured significant under-expression of *Comp* in defiance of phenotypic resemblance to chow-WT littermates. Unlike HF-fed mice, the chow-*foz/foz* profile measured relative over-expression of calcium binding (*Anxa5*) and growth factor *(Fgf1*) genes. Chow-fed mutants were overweight and exhibited higher degree of hyperinsulinemia than obese BALB/c, but less than diabetic NOD·B10 mice, yet retained euglycaemia and indifferent femoral microarchitecture.

It is speculated that the pre-diabetic increase in insulin substrate may have driven growth proliferation and stimulated hydroxyapatite deposition promoting osteoanabolism. However, this project did not find other biochemical nor structural evidence to support this possibility. From these findings, *Fgf1* was implicated both locally and systemically in skeletal diabetes progress, indicated by the diet-differential *foz/foz* mutant responses.

FGF1 was selected for serum ELISA to quantify circulating protein levels indicating insulin dynamics between trabecular bone and the periphery. Despite the sensitivity of the assay to the reported literature, the majority of sample antigen content was not determined across multiple dilutions. As such, results were not statistically assessable. From the available data, FGF1 appeared profoundly increased in HF-*foz/foz* mouse circulation. The potential link between early diabetes onset and FGF1 compensation warrants further investigation, notwithstanding the possibility of a pre-adipocyte ciliopathy synergistic to the model's emphasis.

8.2.1 Limitations Identified in the Current Project

8.2.1.1 Statistical Power

The multi-variate design of this model proved difficult to interpret with less than ten mice per experimental group. The small sample size and complexity of a 2x2x2 (strain x genotype x diet effects) analysis was not robust to ANOVA assumptions in some cases. Despite log transformation to approximately normalise the distribution, some residuals were still in violation of the Shapiro-Wilk normality test, constraining some findings to Mann-Whitney U test. Using this test, groups of 7 or fewer subjects incur a high p-value by default, which plausibly masked the significance of some findings as false errors. We do report statistical significance for Mann-Whitney test with sample size of 7, supporting the notion of valid differences between groups on some parameters however Type 2 error may be present in this design.

By this logic, BALB/c mice were excluded from osteogenic gene expression profiling which may be of interest to further study. Furthermore, the unexpected minimal detection of serum FGF1 by ELISA prohibited statistical analyses with inadequate results to power hypothesis tests. Amongst the diabetic group, several sub-groups may exist, stratified by range of plasma insulin and blood glucose levels, which require more replicates to power discrimination. This is alike humans and discourse on diabetic sub-groups within a population, given the polygenic aetiology of the disease.

8.2.1.2 End-Point Sampling

Use of single sampling point at 13 weeks of age was necessary for the preliminary characterisation of bone outcomes of each strain. Whilst the obesity-borne diabetes phenotype is well-supported by literature, the absence of bone features previously reported in NOD·B10 mice is harder to validate by this single outcome. This cross-sectional study

provides the temporal reference point for further investigations, raising several limitations in the broader bone metabolic literature.

Bone accrual as a function of adipose and muscle mass gains has been shown to determine trabecular and cortical parameters [442]. This warrants further investigation, especially when addressing the insulin resistance and pre-diabetic phases of earlier T2DM during human skeletal ontogeny. Whereas elderly populations gained peak bone mass during growth, childhood and adolescent disease interferes with peak bone acquisition. More work is required to ascertain achievement of peak bone mass as a function of strain, to expand upon the adapting bone geometry under diabetes. Other studies have included entry-point animals to represent initial bone structure, compared to older experimental groups and their age-matched controls, to enable multiple points testing regimes.

8.2.1.3 The *foz/foz* Mutation and Bone

It remains to be resolved how the *foz/foz* mutation may affect bone growth and maintenance. Downstream effects on osteoprogenitors and the MSC lineage are plausible considering *Alms1* pre-adipocyte ciliopathy. Without an overt mutation effect detected in this project, it is unclear if the NOD·B10 background may also contribute to differential skeletal architecture, without concurrence of BALB/c counterparts. More work is required to validate site-specific bone microstructure before inter-strain comparisons between NOD·B10 diabetes susceptible and other diabetes resistant strains can be made.

Longitudinal, comprehensive assessment would also allow for natural progression of the chow-*foz/foz* mice insulin resistant at 13 weeks of age to overt pre-diabetes with raised hyperglycaemia and inevitable diabetes captured over a longer study duration [340]. A model of frank diabetes, such as STZ administration to WT-like *foz*/+ heterozygotes under the same examination could assist in ascertaining NOD·B10 strain-specific growth acquisition impaired by insulin stress without obesity.

8.2.2 Suggestions for Improving Future Studies

8.2.2.1 Axial Site of Interest

The skeleton exerts site-endemic architecture dictated by the orientation of loading axis, and the extent of skeletal attachments enacting force. Studies report well-established differences between axial and appendicular bone features, with particular relevance to the typified diabetic risk of hip and spinal fractures. Aging non-diabetic mouse studies found delayed trabecular bone fraction in the spine compared to the femur [177, 443]. The slower

consolidation of the vertebrae uncomplicated by endochondral ossification of the femur warrants consideration in future study design.

Earlier compensation of the femur, pertinent to a growth-disease study should be contrasted with more inert bone features independent of this process. Certainly a study comparing calvaria reported distinct gene expression profiles for each bone, demonstrating the local spatial influence on individual bone regulation [444]. It is not known whether intensified vertebral architecture over longer study duration would capture metabolic adaptations in the tissue compared with the distal femur.

8.2.2.2 Sex-Specific Differences

Like humans, prior studies of bone structure and strength convincingly demonstrate sex-endemic differences of male and female mice [257]. Male mice are used to detect high turnover phenotypes, with excessive remodelling and destabilisation of immature, disorganised bone. Male NOD·B10 *foz/foz* mice are predisposed to rapid and severe onset disease compared to female mutants, with *ad-libitum* chow-induced obesity and subsequent diabetes [340]. More generally, male mice endure a longer growth span of open physes than females. This may contribute to the more profound and discriminative findings amongst growth studies conducted in male rodents.

Younger female mice may be buffered by an alternative trabecular mobilisation to accommodate pregnancy and lactation demands. Females have higher initial BV/TV compared to males, which diminishes below male counterparts over the lifetime [371]. Thus males may provide accentuated insight to precocious, or acute diabetes effects on bone, unlike subtle effects in female mice which become apparent over a chronic timeframe [445]. Undoubtedly, the elderly mouse bone phenotype strongly aligns with the advanced diabetic milieu by either sex.

8.2.2.3 Histological Additions

The differential trabecular thickness result for diabetic mice suggests a surface area compromise. Fluorescent AGE occupation was investigated by quinine assay in 17 week old TallyHo diabetic mice, however was insignificant [336]. Instead, detection of the ubiquitous and non-fluorescent CML would be more informative. It remains to be determined whether the surface is already occupied by AGEs and homocysteine collagen trapping, or inversely expanded with osteoblast inhibition.

Furthermore, the possibility of adipogenic fate commitment based on PCR results and consideration of the *Alms1* ciliopathy is an area for further investigation. Histology of critical adipogenic and osteogenic cell populations within the femur is warranted to ascertain the spatial dynamics which may be altered under diabetes within the long bone microenvironment. In accord with cell counts, it would be advantageous to detect relevant biomarkers of bone modelling and remodelling such as alkaline phosphatase, bone specific alkaline phosphatase, osteocalcin, procollagen 1 C- and N- terminal propeptides, and the C- and N- terminal telopeptides of type 1 collagen [446, 447].

8.2.2.4 Extending the Duration of the Regime

Longitudinal sampling from 5 months is suggested to build upon the findings of this initial study. Sampling beyond 120 days is expected to i) enable peak bone mass accrual known for BALB/c [374], and provide later characterisation of the unknown peak of NOD·B10 mass; ii) enable NOD·B10 chow-*foz/foz* mice to achieve diabetes [340]; iii) warrant vertebral sampling with later bone microarchitectural development than the femur [177].

8.3 Conclusion

Mice achieved the desired metabolic phenotypes in accord with the model previously described. On the basis of body weight, HF-fed female *foz/foz* mice all achieved obesity regardless of strain background at 13 weeks of age. Plasma insulin concentration and blood glucose concentration distinguished the mutant BALB/c group from hyperinsulinemic and hyperglycaemic NOD·B10 littermates, as the latter were diabetic by the 9 week high fat diet regime.

The evident differences in strain background were also apparent in bone microstructure, as BALB/c mice measured a higher BMD at the distal femur than NOD·B10 mice irrespective of diet or genotype assignment(s). Strain also influenced trabecular thickness, trabecular number, open and total porosity. Based on this inherent variation, inter-strain comparisons were not emphasised to avoid over-representation of diabetes in a single sub-group of the 8 experimental groups; nor under-representation of the strain effect across each background.

Trabecular insight to the NOD·B10 femur revealed emerging changes in microstructural composition despite a consistent BMD. Adaptations emerged by high fat feeding of WT mice, and further when combined with *foz/foz* genetic stress to induce accelerated diabetes in the susceptible NOD·B10 mice. This contrast between HF-fed mice supports the

disciplinary opinion that diabetes exerts differential effects on bone to obesity, even when both co-morbidities arise. Conformation of BMD, BV/TV and cortical features despite marked hyperinsulinemia and hyperglycaemia; osteogenic gene dormancy profile; and the possibility of raised peripheral FGF1 suggested the trabecular capacity for adaptation of the HF-*foz/foz* group.

The BALB/c strain, without the same endemic susceptibility did not reveal altered microstructure at 13 weeks of age, supporting a diabetic response in the dual-stressed NOD·B10. The extent of this adaptation, its long term effects and recovery potential with chronic diabetes and aging remain to be seen. Clinical T2DM research has recognised the over-representation of Caucasian background in a global disease. With further characterisation the obese, diabetic NOD·B10 model may serve to represent a particular sub-group of type 2 diabetics, expanding the diversity of current bone microstructural work.

Trabecular compensation detected in the obese, diabetic female mice was not represented in obese, non-diabetic yet similarly overweight mice, suggesting a diabetes-specific response. Bone quality alongside bone density is integral to better characterise structural and metabolic dysregulation specific to T2DM. This project utilised the previously unreported female NOD·B10 mouse model, with *foz/foz* genotype to detect changes in trabecular bone microstructure and biochemical signalling at 13 weeks of age.

This thesis argues the necessity of trabecular microstructural analysis in type 2 diabetes to assess true bone adaptation and fragility beyond paradoxical bone mineral density measures. The adaptive potential of trabecular bone, especially in younger onset T2DM demands greater consideration of short-term and ongoing changes to bone remodelling capacity and subsequent resilience.

Bibliography

1. Kenkre, J.S. and J.H.D. Bassett, *The bone remodelling cycle.* Annals of Clinical Biochemistry, 2018. **55**(3): p. 308-327.

2. Clarke, B., *Normal Bone Anatomy and Physiology.* Clinical Journal of the American Society of Nephrology, 2008. **3**(Supplement 3): p. S131.

3. Langdahl, B., S. Ferrari, and D.W. Dempster, *Bone modeling and remodeling: potential as therapeutic targets for the treatment of osteoporosis.* Therapeutic Advances in Musculoskeletal Disease, 2016. **8**(6): p. 225-235.

4. Owen, R. and G.C. Reilly, *In vitro Models of Bone Remodelling and Associated Disorders.* Frontiers in Bioengineering and Biotechnology, 2018. **6**: p. 134.

5. WHO, *Assessment of fracture risk and its application to screening for postmenopausal osteoporosis : report of a WHO study group [meeting held in Rome from 22 to 25 June 1992]*. 1994, World Health Organization: Geneva.

6. Gregson, C.L., et al., *'Sink or swim': an evaluation of the clinical characteristics of individuals with high bone mass.* Osteoporosis International, 2012. **23**(2): p. 643-654.

7. Tonna, E.A., *Periosteal osteoclasts, skeletal development and ageing.* Nature, 1960. **185**: p. 405-7.

8. Hodge, J.M., et al., *Osteoclastic potential of human CFU-GM: biphasic effect of GM-CSF.* Journal of Bone and Mineral Research, 2004. **19**(2): p. 190-9.

9. Arai, F., et al., *Commitment and differentiation of osteoclast precursor cells by the sequential expression of c-Fms and receptor activator of nuclear factor kappaB (RANK) receptors.* Journal of Experimental Medicine, 1999. **190**(12): p. 1741-54.

10. Kim, K., et al., *NFATc1 induces osteoclast fusion via up-regulation of Atp6v0d2 and the dendritic cell-specific transmembrane protein (DC-STAMP).* Molecular Endocrinology, 2008. **22**(1): p. 176-85.

11. Kukita, T., et al., *RANKL-induced DC-STAMP is essential for osteoclastogenesis.* Journal of Experimental Medicine, 2004. **200**(7): p. 941-6.

12. Teti, A., et al., *Osteoclast isolation: new developments and methods.* Journal of Bone and Mineral Research, 1999. **14**(7): p. 1251-2.

13. Manolagas, S.C., *Birth and Death of Bone Cells: Basic Regulatory Mechanisms and Implications for the Pathogenesis and Treatment of Osteoporosis.* Endocrine Reviews, 2000. **21**(2): p. 115-137.

14. Udagawa, N., et al., *Origin of osteoclasts: mature monocytes and macrophages are capable of differentiating into osteoclasts under a suitable microenvironment prepared by bone marrow-derived stromal cells.* Proceedings of the National Academy of Sciences of the United States of America, 1990. **87**(18): p. 7260-4.

15. Jaworowski, A., et al., *Roles of the mitogen-activated protein kinase family in macrophage responses to colony stimulating factor-1 addition and withdrawal.* Journal of Biological Chemistry, 1999. **274**(21): p. 15127-33.

16. Hu, R., et al., *Eos, MITF, and PU.1 recruit corepressors to osteoclast-specific genes in committed myeloid progenitors.* Molecular and Cellular Biology, 2007. **27**(11): p. 4018-27.

17. DeKoter, R.P., J.C. Walsh, and H. Singh, *PU.1 regulates both cytokine-dependent proliferation and differentiation of granulocyte/macrophage progenitors.* The EMBO Journal, 1998. **17**(15): p. 4456-68.

18. Kawaguchi, N. and M. Noda, *Mitf is expressed in osteoclast progenitors in vitro.* Experimental Cell Research, 2000. **260**(2): p. 284-91.

19. Lu, S.Y., M. Li, and Y.L. Lin, *Mitf induction by RANKL is critical for osteoclastogenesis.* Molecular Biology of the Cell, 2010. **21**(10): p. 1763-71.

20. Felix, R., et al., *Rapid publication: Impairment of macrophage colony-stimulating factor production and lack of resident bone marrow macrophages in the osteopetrotic op/op Mouse.* Journal of Bone and Mineral Research, 1990. **5**(7): p. 781-789.

21. Mellis, D.J., et al., *The skeleton: a multi-functional complex organ: the role of key signalling pathways in osteoclast differentiation and in bone resorption.* Journal of Endocrinology, 2011. **211**(2): p. 131-43.

22. Usui, M., et al., *Murine and chicken chondrocytes regulate osteoclastogenesis by producing RANKL in response to BMP2.* Journal of Bone and Mineral Research, 2008. **23**(3): p. 314-25.

23. Nakashima, T., et al., *Evidence for osteocyte regulation of bone homeostasis through RANKL expression.* Nature Medicine, 2011. **17**(10): p. 1231-4.

24. Xiong, J., et al., *Matrix-embedded cells control osteoclast formation.* Nature Medicine, 2011. **17**(10): p. 1235-41.

25. Ikeda, T., M. Utsuyama, and K. Hirokawa, *Expression profiles of receptor activator of nuclear factor kappaB ligand, receptor activator of nuclear factor kappaB, and osteoprotegerin messenger RNA in aged and ovariectomized rat bones.* Journal of Bone and Mineral Research, 2001. **16**(8): p. 1416-25.

26. Anderson, D.M., et al., *A homologue of the TNF receptor and its ligand enhance T-cell growth and dendritic-cell function.* Nature, 1997. **390**(6656): p. 175-9.

27. Simonet, W.S., et al., *Osteoprotegerin: a novel secreted protein involved in the regulation of bone density.* Cell, 1997. **89**(2): p. 309-19.

28. Wong, B.R., et al., *TRANCE is a novel ligand of the tumor necrosis factor receptor family that activates c-Jun N-terminal kinase in T cells.* Journal of Biological Chemistry, 1997. **272**(40): p. 25190-4.

29. Yasuda, H., et al., *Identity of osteoclastogenesis inhibitory factor (OCIF) and osteoprotegerin (OPG): a mechanism by which OPG/OCIF inhibits osteoclastogenesis in vitro.* Endocrinology, 1998. **139**(3): p. 1329-37.

30. Dougall, W.C., et al., *RANK is essential for osteoclast and lymph node development.* Genes & Development, 1999. **13**(18): p. 2412-24.

31. Pettit, A.R., et al., *TRANCE/RANKL knockout mice are protected from bone erosion in a serum transfer model of arthritis.* The American Journal of Pathology, 2001. **159**(5): p. 1689-99.

32. Rothe, M., et al., *TRAF2-mediated activation of NF-kappa B by TNF receptor 2 and CD40.* Science, 1995. **269**(5229): p. 1424-7.

33. Wong, B.R., et al., *The TRAF family of signal transducers mediates NF-kappaB activation by the TRANCE receptor.* Journal of Biological Chemistry, 1998. **273**(43): p. 28355-9.

34. Darnay, B.G., et al., *Activation of NF-kappaB by RANK requires tumor necrosis factor receptor-associated factor (TRAF) 6 and NF-kappaB-inducing kinase. Identification of a novel TRAF6 interaction motif.* Journal of Biological Chemistry, 1999. **274**(12): p. 7724-31.

35. Ghosh, S. and M. Karin, *Missing pieces in the NF-kappaB puzzle.* Cell, 2002. **109 Suppl**: p. S81-96.

36. Karin, M. and Y. Ben-Neriah, *Phosphorylation meets ubiquitination: the control of NF-KB activity.* Annual Reviews of Immunology, 2000. **18**: p. 621-63.

37. Boyce, B.F., et al., *NF-κB-Mediated Regulation of Osteoclastogenesis.* Endocrinology and Metabolism, 2015. **30**(1): p. 35-44.

38. Ruocco, M.G., et al., *I{kappa}B kinase (IKK), but not IKK{alpha}, is a critical mediator of osteoclast survival and is required for inflammation-induced bone loss.* Journal of Experimental Medicine, 2005. **201**(10): p. 1677-87.

39. Franzoso, G., et al., *Requirement for NF-kappaB in osteoclast and B-cell development.* Genes & Development, 1997. **11**(24): p. 3482-96.

40. Iotsova, V., et al., *Osteopetrosis in mice lacking NF-kappaB1 and NF-kappaB2.* Nature Medicine, 1997. **3**(11): p. 1285-9.

41. Takayanagi, H., et al., *Induction and activation of the transcription factor NFATc1 (NFAT2) integrate RANKL signaling in terminal differentiation of osteoclasts.* Developmental Cell, 2002. **3**(6): p. 889-901.

42. Zhou, B., et al., *Regulation of the murine Nfatc1 gene by NFATc2.* Journal of Biological Chemistry, 2002. **277**(12): p. 10704-11.

43. Crotti, T.N., et al., *NFATc1 directly induces the human beta3 integrin gene in osteoclast differentiation.* Journal of Musculoskeletal & Neuronal Interactions, 2005. **5**(4): p. 335-337.

44. Tomida, T., et al., *NFAT functions as a working memory of Ca2+ signals in decoding Ca2+ oscillation.* The EMBO Journal, 2003. **22**(15): p. 3825-32.

45. Izawa, N., et al., *Cooperation of PU.1 With IRF8 and NFATc1 Defines Chromatin Landscapes During RANKL-Induced Osteoclastogenesis.* Journal of Bone and Mineral Research, 2019. **34**(6): p. 1143-1154.

46. Nishikawa, K., et al., *Blimp1-mediated repression of negative regulators is required for osteoclast differentiation.* Proceedings of the National Academy of Sciences of the United States of America, 2010. **107**(7): p. 3117-22.

47. Miyauchi, Y., et al., *The Blimp1-Bcl6 axis is critical to regulate osteoclast differentiation and bone homeostasis.* Journal of Experimental Medicine, 2010. **207**(4): p. 751-62.

48. Koga, T., et al., *Costimulatory signals mediated by the ITAM motif cooperate with RANKL for bone homeostasis.* Nature, 2004. **428**(6984): p. 758-63.

49. Asagiri, M., et al., *Autoamplification of NFATc1 expression determines its essential role in bone homeostasis.* Journal of Experimental Medicine, 2005. **202**(9): p. 1261-9.

50. Matsumoto, M., et al., *Involvement of p38 mitogen-activated protein kinase signaling pathway in osteoclastogenesis mediated by receptor activator of NF-kappa B ligand (RANKL).* Journal of Biological Chemistry, 2000. **275**(40): p. 31155-61.

51. Bohm, C., et al., *The alpha-isoform of p38 MAPK specifically regulates arthritic bone loss.* Journal of Immunology, 2009. **183**(9): p. 5938-47.

52. Aubin, J.E., *Regulation of osteoblast formation and function.* Reviews in Endocrine and Metabolic Disorders, 2001. **2**(1): p. 81-94.

53. Keith, A., *Bone growth and bone repair Lecture II. REsearches made by syme and by goodsir regarding the growth and repair of bones.* British Journal of Surgery, 1918. **6**(21): p. 19-23.

54. Komori, T., *Regulation of bone development and extracellular matrix protein genes by RUNX2.* Cell and Tissue Research, 2010. **339**(1): p. 189-195.

55. Samee, N., et al., *Dlx5, a positive regulator of osteoblastogenesis, is essential for osteoblast-osteoclast coupling.* The American Journal of Pathology, 2008. **173**(3): p. 773-80.

56. Nakashima, K., et al., *The Novel Zinc Finger-Containing Transcription Factor Osterix Is Required for Osteoblast Differentiation and Bone Formation.* Cell, 2002. **108**(1): p. 17-29.

57. Otto, F., et al., *Cbfa1, a candidate gene for cleidocranial dysplasia syndrome, is essential for osteoblast differentiation and bone development.* Cell, 1997. **89**(5): p. 765-71.

58. Kawane, T., et al., *Runx2 is required for the proliferation of osteoblast progenitors and induces proliferation by regulating Fgfr2 and Fgfr3.* Scientific Reports, 2018. **8**(1): p. 13551.

59. Komori, T., *Regulation of Proliferation, Differentiation and Functions of Osteoblasts by Runx2.* International Journal of Molecular Sciences, 2019. **20**(7).

60. Jilka, R.L., et al., *Osteoblast programmed cell death (apoptosis): modulation by growth factors and cytokines.* Journal of Bone and Mineral Research, 1998. **13**(5): p. 793-802.

61. Park, D., et al., *Endogenous bone marrow MSCs are dynamic, fate-restricted participants in bone maintenance and regeneration.* Cell Stem Cell, 2012. **10**(3): p. 259-72.

62. Tao, J., S. Chen, and B. Lee, *Alteration of Notch signaling in skeletal development and disease.* Annals of the New York Academy of Sciences, 2010. **1192**: p. 257-68.

63. Pereira, R.M., et al., *Cortisol regulates the expression of Notch in osteoblasts.* Journal of Cell Biology, 2002. **85**(2): p. 252-8.

64. Dallas, D.J., et al., *Localization of ADAM10 and Notch receptors in bone.* Bone, 1999. **25**(1): p. 9-15.

65. Sato, T., et al., *Active gamma-secretase complexes contain only one of each component.* Journal of Biological Chemistry, 2007. **282**(47): p. 33985-93.

66. Schroeter, E.H., J.A. Kisslinger, and R. Kopan, *Notch-1 signalling requires ligand-induced proteolytic release of intracellular domain.* Nature, 1998. **393**(6683): p. 382-6.

67. Zamurovic, N., et al., *Coordinated activation of notch, Wnt, and transforming growth factor-beta signaling pathways in bone morphogenic protein 2-induced osteogenesis. Notch target gene Hey1 inhibits mineralization and Runx2 transcriptional activity.* Journal of Biological Chemistry, 2004. **279**(36): p. 37704-15.

68. Fei, C., et al., *Notch-Hes pathway mediates the impaired osteogenic differentiation of bone marrow mesenchymal stromal cells from myelodysplastic syndromes patients through the down-regulation of Runx2.* American Journal of Translational Research, 2015. **7**(10): p. 1939-51.

69. Kamalakar, A., et al., *A non-canonical JAGGED1 signal to JAK2 mediates osteoblast commitment in cranial neural crest cells.* Cellular Signalling, 2019. **54**: p. 130-138.

70. Canalis, E., et al., *Osteoblast lineage-specific effects of notch activation in the skeleton.* Endocrinology, 2013. **154**(2): p. 623-34.

71. Engin, F., et al., *Dimorphic effects of Notch signaling in bone homeostasis.* Nature Medicine, 2008. **14**(3): p. 299-305.

72. Hilton, M.J., et al., *Notch signaling maintains bone marrow mesenchymal progenitors by suppressing osteoblast differentiation.* Nature Medicine, 2008. **14**(3): p. 306-14.

73. Deregowski, V., et al., *Notch 1 overexpression inhibits osteoblastogenesis by suppressing Wnt/beta-catenin but not bone morphogenetic protein signaling.* Journal of Biological Chemistry, 2006. **281**(10): p. 6203-10.

74. Zanotti, S., et al., *Notch inhibits osteoblast differentiation and causes osteopenia.* Endocrinology, 2008. **149**(8): p. 3890-9.

75. Ren, D.N., et al., *LRP5/6 directly bind to Frizzled and prevent Frizzled-regulated tumour metastasis.* Nature Communications, 2015. **6**: p. 6906.

76. Reinhold, M.I. and M.C. Naski, *Direct interactions of Runx2 and canonical Wnt signaling induce FGF18.* Journal of Biological Chemistry, 2007. **282**(6): p. 3653-63.

77. Li, Z., et al., *Role of TCF/LEF Transcription Factors in Bone Development and Osteogenesis.* International Journal of Medical Sciences, 2018. **15**(12): p. 1415-1422.

78. Liu, C., et al., *Control of beta-catenin phosphorylation/degradation by a dual-kinase mechanism.* Cell, 2002. **108**(6): p. 837-47.

79. Mao, J., et al., *Low-density lipoprotein receptor-related protein-5 binds to Axin and regulates the canonical Wnt signaling pathway.* Molecular Cell, 2001. **7**(4): p. 801-9.

80. Houschyar, K.S., et al., *Wnt Pathway in Bone Repair and Regeneration - What Do We Know So Far.* Frontiers in Cell and Developmental Biology, 2018. **6**: p. 170.

81. Oishi, I., et al., *The receptor tyrosine kinase Ror2 is involved in non-canonical Wnt5a/JNK signalling pathway.* Genes to Cells, 2003. **8**(7): p. 645-54.

82. Takada, I., et al., *Suppression of PPAR transactivation switches cell fate of bone marrow stem cells from adipocytes into osteoblasts.* Annals of the New York Academy of Sciences, 2007. **1116**: p. 182-95.

83. Gong, Y., et al., *LDL receptor-related protein 5 (LRP5) affects bone accrual and eye development.* Cell, 2001. **107**(4): p. 513-23.

84. Kato, M., et al., *Cbfa1-independent decrease in osteoblast proliferation, osteopenia, and persistent embryonic eye vascularization in mice deficient in Lrp5, a Wnt coreceptor.* Journal of Cell Biology, 2002. **157**(2): p. 303-14.

85. Little, R.D., et al., *A mutation in the LDL receptor-related protein 5 gene results in the autosomal dominant high-bone-mass trait.* The American Journal of Human Genetics, 2002. **70**(1): p. 11-9.

86. Babij, P., et al., *High bone mass in mice expressing a mutant LRP5 gene.* Journal of Bone and Mineral Research, 2003. **18**(6): p. 960-74.

87. Riddle, R.C., et al., *Lrp5 and Lrp6 exert overlapping functions in osteoblasts during postnatal bone acquisition.* PLoS One, 2013. **8**(5): p. e63323.

88. Semenov, M., K. Tamai, and X. He, *SOST is a ligand for LRP5/LRP6 and a Wnt signaling inhibitor.* Journal of Biological Chemistry, 2005. **280**(29): p. 26770-5.

89. Wrana, J.L., et al., *TGF beta signals through a heteromeric protein kinase receptor complex.* Cell, 1992. **71**(6): p. 1003-14.

90. Heldin, C.H. and A. Moustakas, *Role of Smads in TGFbeta signaling.* Cell and Tissue Research, 2012. **347**(1): p. 21-36.

91. Koch, F.P., et al., *GDF-5 and BMP-2 regulate bone cell differentiation by gene expression of MSX1, MSX2, Dlx5, and Runx2 and influence OCN gene expression in vitro.* The International Journal of Periodontics and Restorative Dentistry, 2012. **32**(3): p. 285-93.

92. Nohe, A., et al., *The mode of bone morphogenetic protein (BMP) receptor oligomerization determines different BMP-2 signaling pathways.* Journal of Biological Chemistry, 2002. **277**(7): p. 5330-8.

93. Noel, D., et al., *Short-term BMP-2 expression is sufficient for in vivo osteochondral differentiation of mesenchymal stem cells.* Stem Cells, 2004. **22**(1): p. 74-85.

94. Zhang, L., et al., *Transcriptomic landscape regulated by the 14 types of bone morphogenetic proteins (BMPs) in lineage commitment and differentiation of mesenchymal stem cells (MSCs).* Genes & Diseases, 2019. **6**(3): p. 258-275.

95. Luu, H.H., et al., *Distinct roles of bone morphogenetic proteins in osteogenic differentiation of mesenchymal stem cells.* Journal of Orthopaedic Research, 2007. **25**(5): p. 665-77.

96. Daluiski, A., et al., *Bone morphogenetic protein-3 is a negative regulator of bone density.* Nature Genetics, 2001. **27**(1): p. 84-88.

97. Tsuji, K., et al., *BMP2 activity, although dispensable for bone formation, is required for the initiation of fracture healing.* Nature Genetics, 2006. **38**(12): p. 1424-9.

98. Tsuji, K., et al., *BMP4 is dispensable for skeletogenesis and fracture-healing in the limb.* Journal of Bone and Joint Surgery (American volume), 2008. **90 Suppl 1**: p. 14-8.

99. Tsuji, K., et al., *Conditional deletion of BMP7 from the limb skeleton does not affect bone formation or fracture repair.* Journal of Orthopaedic Research, 2010. **28**(3): p. 384-9.

100. Solloway, M.J., et al., *Mice lacking Bmp6 function.* Developmental Genetics, 1998. **22**(4): p. 321-39.

101. Bandyopadhyay, A., et al., *Genetic analysis of the roles of BMP2, BMP4, and BMP7 in limb patterning and skeletogenesis.* PLoS Genetics, 2006. **2**(12): p. e216.

102. Tang, Y., et al., *TGF-beta1-induced migration of bone mesenchymal stem cells couples bone resorption with formation.* Nature Medicine, 2009. **15**(7): p. 757-65.

103. Li, J., et al., *Smad2 overexpression enhances Smad4 gene expression and suppresses CBFA1 gene expression in osteoblastic osteosarcoma ROS17/2.8 cells and primary rat calvaria cells.* Journal of Biological Chemistry, 1998. **273**(47): p. 31009-15.

104. Kang, J.S., et al., *Repression of Runx2 function by TGF-beta through recruitment of class II histone deacetylases by Smad3.* The EMBO Journal, 2005. **24**(14): p. 2543-55.

105. Derynck, R. and Y.E. Zhang, *Smad-dependent and Smad-independent pathways in TGF-beta family signalling.* Nature, 2003. **425**(6958): p. 577-84.

106. Karsdal, M.A., et al., *Transforming growth factor-beta controls human osteoclastogenesis through the p38 MAPK and regulation of RANK expression.* Journal of Biological Chemistry, 2003. **278**(45): p. 44975-87.

107. Matsunobu, T., et al., *Critical roles of the TGF-beta type I receptor ALK5 in perichondrial formation and function, cartilage integrity, and osteoblast differentiation during growth plate development.* Developmental Biology, 2009. **332**(2): p. 325-38.

108. Crane, J.L., L. Xian, and X. Cao, *Role of TGF-beta Signaling in Coupling Bone Remodeling.* Methods in Molecular Biology, 2016. **1344**: p. 287-300.

109. Yasui, T., et al., *Regulation of RANKL-induced osteoclastogenesis by TGF-beta through molecular interaction between Smad3 and Traf6.* Journal of Bone and Mineral Research, 2011. **26**(7): p. 1447-56.

110. Chen, X., et al., *Processing and turnover of the Hedgehog protein in the endoplasmic reticulum.* Journal of Cell Biology, 2011. **192**(5): p. 825-38.

111. Marigo, V., et al., *Biochemical evidence that patched is the Hedgehog receptor.* Nature, 1996. **384**(6605): p. 176-9.

112. Stone, D.M., et al., *The tumour-suppressor gene patched encodes a candidate receptor for Sonic hedgehog.* Nature, 1996. **384**(6605): p. 129-34.

113. Kim, J., M. Kato, and P.A. Beachy, *Gli2 trafficking links Hedgehog-dependent activation of Smoothened in the primary cilium to transcriptional activation in the nucleus.* Proceedings of the National Academy of Sciences of the United States of America, 2009. **106**(51): p. 21666-71.

114. Sasaki, H., et al., *Regulation of Gli2 and Gli3 activities by an amino-terminal repression domain: implication of Gli2 and Gli3 as primary mediators of Shh signaling.* Development, 1999. **126**(17): p. 3915.

115. Park, H.L., et al., *Mouse Gli1 mutants are viable but have defects in SHH signaling in combination with a Gli2 mutation.* Development, 2000. **127**(8): p. 1593.

116. St-Jacques, B., M. Hammerschmidt, and A.P. McMahon, *Indian hedgehog signaling regulates proliferation and differentiation of chondrocytes and is essential for bone formation.* Genes & Development, 1999. **13**(16): p. 2072-86.

117. Hilton, M.J., et al., *Ihh controls cartilage development by antagonizing Gli3, but requires additional effectors to regulate osteoblast and vascular development.* Development, 2005. **132**(19): p. 4339-51.

118. Long, F., et al., *Ihh signaling is directly required for the osteoblast lineage in the endochondral skeleton.* Development, 2004.

119. Jemtland, R., et al., *Hedgehog promotes primary osteoblast differentiation and increases PTHrP mRNA expression and iPTHrP secretion.* Bone, 2003. **32**(6): p. 611-20.

120. Murakami, S., A. Nifuji, and M. Noda, *Expression of Indian hedgehog in osteoblasts and its posttranscriptional regulation by transforming growth factor-beta.* Endocrinology, 1997. **138**(5): p. 1972-8.

121. Deng, A., et al., *Knockdown of Indian hedgehog protein induces an inhibition of cell growth and differentiation in osteoblast MC3T3E1 cells.* Molecular Medicine Reports, 2017. **16**(6): p. 7987-7992.

122. Regard, J.B., et al., *Activation of Hedgehog signaling by loss of GNAS causes heterotopic ossification.* Nature Medicine, 2013. **19**(11): p. 1505-12.

123. Mak, K.K., et al., *Hedgehog signaling in mature osteoblasts regulates bone formation and resorption by controlling PTHrP and RANKL expression.* Developmental Cell, 2008. **14**(5): p. 674-88.

124. Rodan, G.A. and T.J. Martin, *Role of osteoblasts in hormonal control of bone resorption--a hypothesis.* Calcified Tissue International, 1981. **33**(4): p. 349-51.

125. Dudley, H.R. and D. Spiro, *The Fine Structure of Bone Cells.* Journal of Biophysical and Biochemical Cytology, 1961. **11**(3): p. 627-49.

126. Miller, S.C., et al., *Characterization of endosteal bone-lining cells from fatty marrow bone sites in adult beagles.* The Anatomical Record, 1980. **198**(2): p. 163-73.

127. Hauge, E.M., et al., *Cancellous bone remodeling occurs in specialized compartments lined by cells expressing osteoblastic markers.* Journal of Bone and Mineral Research, 2001. **16**(9): p. 1575-82.

128. Jones, S.J. and A. Boyde, *Morphological changes of osteoblasts in vitro.* Cell and Tissue Research, 1976. **166**(1): p. 101-7.

129. Pettit, A.R., et al., *Osteal macrophages: a new twist on coupling during bone dynamics.* Bone, 2008. **43**(6): p. 976-82.

130. Matic, I., et al., *Quiescent Bone Lining Cells Are a Major Source of Osteoblasts During Adulthood.* Stem Cells, 2016. **34**(12): p. 2930-2942.

131. Kim, S.W., et al., *Sclerostin Antibody Administration Converts Bone Lining Cells Into Active Osteoblasts.* Journal of Bone and Mineral Research, 2017. **32**(5): p. 892-901.

132. Dobnig, H. and R.T. Turner, *Evidence that intermittent treatment with parathyroid hormone increases bone formation in adult rats by activation of bone lining cells.* Endocrinology, 1995. **136**(8): p. 3632-8.

133. Leaffer, D., et al., *Modulation of osteogenic cell ultrastructure by RS-23581, an analog of human parathyroid hormone (PTH)-related peptide-(1-34), and bovine PTH-(1-34).* Endocrinology, 1995. **136**(8): p. 3624-31.

134. Boppart, M.D., et al., *Time course of osteoblast appearance after in vivo mechanical loading.* Bone, 1998. **23**(5): p. 409-15.

135. Power, R.A., et al., *Basic fibroblast growth factor has rapid bone anabolic effects in ovariectomized rats.* Osteoporos International, 2004. **15**(9): p. 716-23.

136. Turner, R.T., et al., *Acute exposure to high dose gamma-radiation results in transient activation of bone lining cells.* Bone, 2013. **57**(1): p. 164-73.

137. Nioi, P., et al., *Transcriptional Profiling of Laser Capture Microdissected Subpopulations of the Osteoblast Lineage Provides Insight Into the Early Response to Sclerostin Antibody in Rats.* Journal of Bone and Mineral Research, 2015. **30**(8): p. 1457-67.

138. Ominsky, M.S., et al., *Tissue-level mechanisms responsible for the increase in bone formation and bone volume by sclerostin antibody.* Journal of Bone and Mineral Research, 2014. **29**(6): p. 1424-30.

139. Everts, V., et al., *The bone lining cell: its role in cleaning Howship's lacunae and initiating bone formation.* Journal of Bone and Mineral Research, 2002. **17**(1): p. 77-90.

140. Capulli, M., R. Paone, and N. Rucci, *Osteoblast and osteocyte: games without frontiers.* Archives of Biochemistry and Biophysics, 2014. **561**: p. 3-12.

141. Tonna, E.A. and N.M. Lampen, *Electron microscopy of aging skeletal cells. I. Centrioles and solitary cilia.* Journal of Gerontology, 1972. **27**(3): p. 316-24.

142. Yellowley, C.E., et al., *Functional gap junctions between osteocytic and osteoblastic cells.* Journal of Bone and Mineral Research, 2000. **15**(2): p. 209-17.

143. Lu, Y., et al., *The biological function of DMP-1 in osteocyte maturation is mediated by its 57-kDa C-terminal fragment.* Journal of Bone and Mineral Research, 2011. **26**(2): p. 331-40.

144. Kalajzic, I., et al., *Dentin matrix protein 1 expression during osteoblastic differentiation, generation of an osteocyte GFP-transgene.* Bone, 2004. **35**(1): p. 74-82.

145. Poole, K.E., et al., *Sclerostin is a delayed secreted product of osteocytes that inhibits bone formation.* The FASEB Journal, 2005. **19**(13): p. 1842-4.

146. Macewen, W., *The growth of bone: observations on osteogenesis: an experimental inquiry into the development and reproduction of diaphyseal bone*. 1912: J. Maclehose.

147. Sawa, N., et al., *Alternating Differentiation and Dedifferentiation between Mature Osteoblasts and Osteocytes.* Scientific Reports, 2019. **9**(1): p. 13842.

148. Havers, C., *Osteologia nova, or, Some new observations of the bones, and the parts belonging to them, with the manner of their accretion, and nutrition, communicated to the Royal Society in several discourses [microform] : to which is added a fifth discourse of the cartilages*. Early English books, 1641-1700 ; 668:9., ed. S. Royal. 1691, London: Printed for Samuel Smith.

149. Hattner, R., B.N. Epker, and H.M. Frost, *Suggested Sequential Mode of Control of Changes in Cell Behaviour in Adult Bone Remodelling.* Nature, 1965. **206**(4983): p. 489-490.

150. Weinbaum, S., S.C. Cowin, and Y. Zeng, *A model for the excitation of osteocytes by mechanical loading-induced bone fluid shear stresses.* Journal of Biomechanics, 1994. **27**(3): p. 339-60.

151. Hoey, D.A., D.J. Kelly, and C.R. Jacobs, *A role for the primary cilium in paracrine signaling between mechanically stimulated osteocytes and mesenchymal stem cells.* Biochemical and Biophysical Research Communications, 2011. **412**(1): p. 182-7.

152. Klein-Nulend, J., et al., *Pulsating fluid flow increases nitric oxide (NO) synthesis by osteocytes but not periosteal fibroblasts--correlation with prostaglandin upregulation.* Biochemical and Biophysical Research Communications, 1995. **217**(2): p. 640-8.

153. Cherian, P.P., et al., *Effects of mechanical strain on the function of Gap junctions in osteocytes are mediated through the prostaglandin EP2 receptor.* Journal of Biological Chemistry, 2003. **278**(44): p. 43146-56.

154. Genetos, D.C., et al., *Oscillating fluid flow activation of gap junction hemichannels induces ATP release from MLO-Y4 osteocytes.* Journal of Cellular Physiology, 2007. **212**(1): p. 207-14.

155. Heino, T.J., T.A. Hentunen, and H.K. Vaananen, *Conditioned medium from osteocytes stimulates the proliferation of bone marrow mesenchymal stem cells and their differentiation into osteoblasts.* Experimental Cell Research, 2004. **294**(2): p. 458-68.

156. Feng, J.Q., et al., *Loss of DMP1 causes rickets and osteomalacia and identifies a role for osteocytes in mineral metabolism.* Nature Genetics, 2006. **38**(11): p. 1310-5.

157. Tatsumi, S., et al., *Targeted ablation of osteocytes induces osteoporosis with defective mechanotransduction.* Cell Metabolism, 2007. **5**(6): p. 464-75.

158. Verborgt, O., G.J. Gibson, and M.B. Schaffler, *Loss of osteocyte integrity in association with microdamage and bone remodeling after fatigue in vivo.* Journal of Bone and Mineral Research, 2000. **15**(1): p. 60-7.

159. Wu, A.C., et al., *MCP-1 expression is specifically regulated during activation of skeletal repair and remodeling.* Calcified Tissue International, 2013. **92**(6): p. 566-75.

160. Zhang, Y., et al., *Enhanced osteoclastic resorption and responsiveness to mechanical load in gap junction deficient bone.* PLoS One, 2011. **6**(8): p. e23516.

161. Kennedy, O.D., et al., *Activation of resorption in fatigue-loaded bone involves both apoptosis and active pro-osteoclastogenic signaling by distinct osteocyte populations.* Bone, 2012. **50**(5): p. 1115-22.

162. Noble, B.S., et al., *Identification of apoptotic changes in osteocytes in normal and pathological human bone.* Bone, 1997. **20**(3): p. 273-82.

163. Couly, G., et al., *Determination of the identity of the derivatives of the cephalic neural crest: incompatibility between Hox gene expression and lower jaw development.* Development, 1998. **125**(17): p. 3445.

164. Ducy, P., T. Schinke, and G. Karsenty, *The osteoblast: a sophisticated fibroblast under central surveillance.* Science, 2000. **289**(5484): p. 1501-4.

165. Olsen, B.R., A.M. Reginato, and W. Wang, *Bone development.* Annual Review of Cell and Developmental Biology, 2000. **16**: p. 191-220.

166. Opperman, L.A., *Cranial sutures as intramembranous bone growth sites.* Developmental Dynamics, 2000. **219**(4): p. 472-485.

167. Abzhanov, A., et al., *Regulation of skeletogenic differentiation in cranial dermal bone.* Development, 2007. **134**(17): p. 3133-44.

168. Sano, H., et al., *Evidence for Ongoing Modeling-Based Bone Formation in Human Femoral Head Trabeculae via Forming Minimodeling Structures: A Study in Patients with Fractures and Arthritis.* Frontiers in Endocrinology (Lausanne), 2018. **9**: p. 88.

169. Epker, B.N. and H.M. Frost, *Periosteal appositional bone growth from age two to age seventy in man. A tetracycline evaluation.* The Anatomical Record, 1966. **154**(3): p. 573-7.

170. Erben, R.G., *Trabecular and endocortical bone surfaces in the rat: modeling or remodeling?* The Anatomical Record, 1996. **246**(1): p. 39-46.

171. Pead, M.J., T.M. Skerry, and L.E. Lanyon, *Direct transformation from quiescence to bone formation in the adult periosteum following a single brief period of bone loading.* Journal of Bone and Mineral Research, 1988. **3**(6): p. 647-56.

172. Ruff, C.B. and W.C. Hayes, *Subperiosteal expansion and cortical remodeling of the human femur and tibia with aging.* Science, 1982. **217**(4563): p. 945.

173. Wolff, J.A., *The Law of Bone Remodelling*
1986, Berlin Heidelberg: B Springer

174. Erben, R.G., *Hypothesis: Coupling between Resorption and Formation in Cancellous bone Remodeling is a Mechanically Controlled Event.* Frontiers in Endocrinology (Lausanne), 2015. **6**: p. 82.

175. Bala, Y. and E. Seeman, *Bone's Material Constituents and their Contribution to Bone Strength in Health, Disease, and Treatment.* Calcified Tissue International, 2015. **97**(3): p. 308-326.

176. Fajardo, R.J., et al., *A review of rodent models of type 2 diabetic skeletal fragility.* Journal of Bone and Mineral Research, 2014. **29**(5): p. 1025-40.

177. Glatt, V., et al., *Age-related changes in trabecular architecture differ in female and male C57BL/6J mice.* Journal of Bone and Mineral Research, 2007. **22**(8): p. 1197-207.

178. Fernandez-Tresguerres-Hernandez-Gil, I., et al., *Physiological bases of bone regeneration II. The remodeling process.* Medicina Oral, Patologia Oral, Cirugia Bucal, 2006. **11**(2): p. E151-7.

179. Lindsay, R., et al., *Effects of a one-month treatment with PTH(1-34) on bone formation on cancellous, endocortical, and periosteal surfaces of the human ilium.* Journal of Bone and Mineral Research, 2007. **22**(4): p. 495-502.

180. Einhorn, T.A., *Bone strength: the bottom line.* Calcified Tissue International, 1992. **51**(5): p. 333-9.

181. Chambers, T.J. and K. Fuller, *Bone cells predispose bone surfaces to resorption by exposure of mineral to osteoclastic contact.* Journal of Cell Science, 1985. **76**: p. 155-65.

182. Tang, S.Y., et al., *Matrix metalloproteinase-13 is required for osteocytic perilacunar remodeling and maintains bone fracture resistance.* Journal of Bone and Mineral Research, 2012. **27**(9): p. 1936-50.

183. Matsuo, K. and N. Irie, *Osteoclast-osteoblast communication.* Archives of Biochemistry and Biophysics, 2008. **473**(2): p. 201-9.

184. Yagi, M., et al., *Induction of DC-STAMP by alternative activation and downstream signaling mechanisms.* Journal of Bone and Mineral Research, 2007. **22**(7): p. 992-1001.

185. Witwicka, H., et al., *Studies of OC-STAMP in Osteoclast Fusion: A New Knockout Mouse Model, Rescue of Cell Fusion, and Transmembrane Topology.* PLoS One, 2015. **10**(6): p. e0128275.

186. Marchisio, P.C., et al., *Cell-substratum interaction of cultured avian osteoclasts is mediated by specific adhesion structures.* Journal of Cell Biology, 1984. **99**(5): p. 1696-1705.

187. Lakkakorpi, P.T., et al., *Vitronectin receptor has a role in bone resorption but does not mediate tight sealing zone attachment of osteoclasts to the bone surface.* Journal of Cell Biology, 1991. **115**(4): p. 1179-86.

188. Chabadel, A., et al., *CD44 and β3 Integrin Organize Two Functionally Distinct Actin-based Domains in Osteoclasts.* Molecular Biology of the Cell, 2007. **18**(12): p. 4899-4910.

189. Feng, X. and J.M. McDonald, *Disorders of bone remodeling.* Annual Review of Pathology: Mechanisms of Disease, 2011. **6**: p. 121-45.

190. Von Euw, S., et al., *Bone mineral: new insights into its chemical composition.* Scientific Reports, 2019. **9**(1): p. 8456.

191. Blair, H.C., et al., *Osteoclastic bone resorption by a polarized vacuolar proton pump.* Science, 1989. **245**(4920): p. 855-7.

192. Kornak, U., et al., *Loss of the ClC-7 chloride channel leads to osteopetrosis in mice and man.* Cell, 2001. **104**(2): p. 205-15.

193. Lehenkari, P., et al., *Carbonic anhydrase II plays a major role in osteoclast differentiation and bone resorption by effecting the steady state intracellular pH and Ca2+.* Experimental Cell Research, 1998. **242**(1): p. 128-37.

194. Bernhardt, A., et al., *Relevance of osteoclast-specific enzyme activities in cell-based in vitro resorption assays.* European Cells and Materials, 2017. **33**: p. 28-42.

195. Christensen, J. and V.P. Shastri, *Matrix-metalloproteinase-9 is cleaved and activated by cathepsin K.* BMC Research Notes, 2015. **8**: p. 322.

196. Ek-Rylander, B., et al., *Dephosphorylation of osteopontin and bone sialoprotein by osteoclastic tartrate-resistant acid phosphatase. Modulation of osteoclast adhesion in vitro.* Journal of Biological Chemistry, 1994. **269**(21): p. 14853-6.

197. Vaaraniemi, J., et al., *Intracellular machinery for matrix degradation in bone-resorbing osteoclasts.* Journal of Bone and Mineral Research, 2004. **19**(9): p. 1432-40.

198. Arey, L.B., *The origin, growth and fate of osteoclasts and their relation to bone resorption.* American Journal of Anatomy, 1920. **26**(3): p. 314-345.

199. Lorget, F., et al., *High extracellular calcium concentrations directly stimulate osteoclast apoptosis.* Biochemical and Biophysical Research Communications, 2000. **268**(3): p. 899-903.

200. Liu, C.C. and G.A. Howard, *Bone-cell changes in estrogen-induced bone-mass increase in mice: dissociation of osteoclasts from bone surfaces.* The Anatomical Record, 1991. **229**(2): p. 240-50.

201. Nakamura, T., et al., *Estrogen prevents bone loss via estrogen receptor alpha and induction of Fas ligand in osteoclasts.* Cell, 2007. **130**(5): p. 811-23.

202. Sedger, L.M., et al., *Characterization of the in vivo function of TNF-α-related apoptosis-inducing ligand, TRAIL/Apo2L, using TRAIL/Apo2L gene-deficient mice.* European Journal of Immunology, 2002. **32**(8): p. 2246-2254.

203. Baron, R., R. Tross, and A. Vignery, *Evidence of sequential remodeling in rat trabecular bone: morphology, dynamic histomorphometry, and changes during skeletal maturation.* The Anatomical Record, 1984. **208**(1): p. 137-45.

204. Lassen, N.E., et al., *Coupling of Bone Resorption and Formation in Real Time: New Knowledge Gained From Human Haversian BMUs.* Journal of Bone and Mineral Research, 2017. **32**(7): p. 1395-1405.

205. Furuya, M., et al., *Direct cell-cell contact between mature osteoblasts and osteoclasts dynamically controls their functions in vivo.* Nature Communications, 2018. **9**(1): p. 300.

206. Pfeilschifter, J. and G.R. Mundy, *Modulation of type beta transforming growth factor activity in bone cultures by osteotropic hormones.* Proceedings of the National Academy of Sciences of the United States of America, 1987. **84**(7): p. 2024-8.

207. Johansen, J.S., et al., *Identification of proteins secreted by human osteoblastic cells in culture.* Journal of Bone and Mineral Research, 1992. **7**(5): p. 501-12.

208. Aghajanian, P. and S. Mohan, *The art of building bone: emerging role of chondrocyte-to-osteoblast transdifferentiation in endochondral ossification.* Bone Research, 2018. **6**: p. 19.

209. Zhou, X., et al., *Chondrocytes transdifferentiate into osteoblasts in endochondral bone during development, postnatal growth and fracture healing in mice.* PLoS Genetics, 2014. **10**(12): p. e1004820.

210. Anderson, H.C., *Molecular biology of matrix vesicles.* Clinical Orthopedics and Related Research, 1995(314): p. 266-80.

211. Wang, B., et al., *NHERF1 regulation of PTH-dependent bimodal Pi transport in osteoblasts.* Bone, 2013. **52**(1): p. 268-77.

212. Blair, H.C., et al., *Osteoblast Differentiation and Bone Matrix Formation In Vivo and In Vitro.* Tissue Engineering Part B: Reviews, 2017. **23**(3): p. 268-280.

213. Wang, L. and G.H. Nancollas, *Calcium orthophosphates: crystallization and dissolution.* Chemical Reviews, 2008. **108**(11): p. 4628-4669.

214. Baht, G.S., G.K. Hunter, and H.A. Goldberg, *Bone sialoprotein-collagen interaction promotes hydroxyapatite nucleation.* Matrix Biology, 2008. **27**(7): p. 600-8.

215. Florencio-Silva, R., et al., *Biology of Bone Tissue: Structure, Function, and Factors That Influence Bone Cells.* Biomedical Research International, 2015. **2015**: p. 421746.

216. Kim, J. and T. Adachi, *Cell-fate decision of mesenchymal stem cells toward osteocyte differentiation is committed by spheroid culture.* Scientific Reports, 2021. **11**(1): p. 13204.

217. Pederson, L., et al., *Regulation of bone formation by osteoclasts involves Wnt/BMP signaling and the chemokine sphingosine-1-phosphate.* Proceedings of the National Academy of Sciences of the United States of America, 2008. **105**(52): p. 20764-9.

218. Shiwaku, Y., et al., *The Crosstalk between Osteoclasts and Osteoblasts Is Dependent upon the Composition and Structure of Biphasic Calcium Phosphates.* PLoS One, 2015. **10**(7): p. e0132903.

219. Sims, N.A. and T.J. Martin, *Coupling the activities of bone formation and resorption: a multitude of signals within the basic multicellular unit.* BoneKEy Reports, 2014. **3**: p. 481.

220. Jimi, E., et al., *Osteoclast function is activated by osteoblastic cells through a mechanism involving cell-to-cell contact.* Endocrinology, 1996. **137**(5): p. 2187-90.

221. ADA, A.D.A., *Classification and diagnosis of diabetes*, in *Diabetes Care*. 2015. p. S8-S16.

222. WHO, W.H.O., *Classification of diabetes mellitus*. 2019, World Health Organisation: Geneva.

223. Cho, N., et al., *IDF Diabetes Atlas: Global estimates of diabetes prevalence for 2017 and projections for 2045.* Diabetes Research and Clinical Practice, 2018. **138**: p. 271-281.

224. CDC, C.f.D.C.a.P., *National diabetes statistics report 2020*. 2020, US Department of Health and Human Services: Atlanta.

225. AIHW and D.o.H.a.F. Services, *First Report on the National Health Priority Areas, full report*, D.o.H.a.F. Services, Editor. 1997, AIHW: Australia. p. 201.

226. AIHW, *Impact of Overweight and Obesity as a risk factor for chronic conditions*, A.I.o.H.a. Welfare, Editor. 2017, AIHW: Canberra. p. 68.

227. Nolan, C.J., P. Damm, and M. Prentki, *Type 2 diabetes across generations: from pathophysiology to prevention and management.* The Lancet, 2011. **378**(9786): p. 169-181.

228. Ma, R.C.W. and B.M. Popkin, *Intergenerational diabetes and obesity-A cycle to break?* PLoS Medicine, 2017. **14**(10): p. e1002415-e1002415.

229. Inacio, M.C.S., et al., *Increase in Total Joint Arthroplasty Projected from 2014 to 2046 in Australia: A Conservative Local Model With International Implications.* Clinical Orthopaedics and Related Research 2017. **475**(8): p. 2130-2137.

230. Culliford, D., et al., *Future projections of total hip and knee arthroplasty in the UK: results from the UK Clinical Practice Research Datalink.* Osteoarthritis and Cartilage, 2015. **23**(4): p. 594-600.

231. Heath, H., 3rd, L.J. Melton, 3rd, and C.P. Chu, *Diabetes mellitus and risk of skeletal fracture.* New England Journal of Medicine, 1980. **303**(10): p. 567-70.

232. Melton III, L.J., et al., *Fracture Risk in Type 2 Diabetes: Update of a Population-Based Study.* Journal of Bone and Mineral Research, 2008. **23**(8): p. 1334-1342.

233. Miyake, H., I. Kanazawa, and T. Sugimoto, *Association of Bone Mineral Density, Bone Turnover Markers, and Vertebral Fractures with All-Cause Mortality in Type 2 Diabetes Mellitus.* Calcified Tissue International, 2018. **102**(1): p. 1-13.

234. Leibson, C.L., et al., *Temporal trends in BMI among adults with diabetes.* Diabetes Care, 2001. **24**(9): p. 1584-9.

235. Park, H.Y., et al., *The risk of hip fractures in individuals over 50 years old with prediabetes and type 2 diabetes – A longitudinal nationwide population-based study.* Bone, 2021. **142**: p. 115691.

236. Louati, K., et al., *Association between diabetes mellitus and osteoarthritis: systematic literature review and meta-analysis.* RMD Open, 2015. **1**(1): p. e000077.

237. Martinez, S., et al., *The diabetic paradox: Bone mineral density and fracture in type 2 diabetes.* Endocrinology and Nutrition (Endocrinología y Nutrición, English Edition), 2016. **63**(9): p. 495-501.

238. Compston, J., *Type 2 diabetes mellitus and bone.* Journal of Internal Medicine, 2018. **283**(2): p. 140-153.

239. Martin, T.J., *Reflecting on Some Discoveries of 40 Years and Their Outcomes.* Journal of Bone and Mineral Research, 2017. **32**(10): p. 1971-1976.

240. Tsang, S.-T.J. and P. Gaston, *Adverse peri-operative outcomes following elective total hip replacement in diabetes mellitus.* The Bone & Joint Journal, 2013. **95-B**(11): p. 1474-1479.

241. Leitner, L., et al., *The Dark Side of Arthroplasty: Competing Risk Analysis of Failed Hip and Knee Arthroplasty With Periprosthetic Joint Infection.* Journal of Arthroplasty, 2020.

242. Na, A., L. Jansky, and Z. Gugala, *Clinical Characteristics of Patients with Type 2 Diabetes Mellitus Receiving a Primary Total Knee or Hip Arthroplasty.* Journal of Diabetes Research, 2019. **2019**: p. 9459206.

243. Levin, M.E., V.C. Boisseau, and L.V. Avioli, *Effects of diabetes mellitus on bone mass in juvenile and adult-onset diabetes.* New England Journal of Medicine, 1976. **294**(5): p. 241-5.

244. Capozzi, J.D., et al., *The prevalence of diabetes mellitus and routine hemoglobin A1c screening in elective total joint arthroplasty patients.* The Journal of Arthroplasty, 2017. **32**(1): p. 304-308.

245. Kanis, J.A., et al., *The diagnosis of osteoporosis.* Journal of Bone and Mineral Research, 1994. **9**(8): p. 1137-1141.

246. Albright, F. and E. Reifenstein Jr, *The Parathyroid Glands and Metabolic Bone Disease: Selected Studies. Baltimore, 1948*. 1948, Williams & Wilkins Co.

247. Krakauer, J.C., et al., *Bone Loss and Bone Turnover in Diabetes.* Diabetes, 1995. **44**(7): p. 775-782.

248. van Daele, P.L., et al., *Bone density in non-insulin-dependent diabetes mellitus. The Rotterdam Study.* Annals of Internal Medicine, 1995. **122**(6): p. 409-14.

249. Cummings, S.R., D. Bates, and D.M. Black, *Clinical Use of Bone Densitometry: Scientific Review.* JAMA, 2002. **288**(15): p. 1889-1897.

250. Oei, L., et al., *High bone mineral density and fracture risk in type 2 diabetes as skeletal complications of inadequate glucose control: the Rotterdam Study.* Diabetes Care, 2013. **36**(6): p. 1619-1628.

251. Meyer, H.E., A. Tverdal, and J.A. Falch, *Risk factors for hip fracture in middle-aged Norwegian women and men.* Americal Journal of Epidemiology, 1993. **137**(11): p. 1203-11.

252. Frederiksen, K.D., et al., *Bone Structural Changes and Estimated Strength After Gastric Bypass Surgery Evaluated by HR-pQCT.* Calcified Tissue International, 2016. **98**(3): p. 253-62.

253. Compston, J.E., et al., *Obesity is not protective against fracture in postmenopausal women: GLOW.* The American Journal of Medicine, 2011. **124**(11): p. 1043-50.

254. Maimoun, L., et al., *Impact of obesity on bone mass throughout adult life: Influence of gender and severity of obesity.* Bone, 2016. **90**: p. 23-30.

255. Nielson, C.M., P. Srikanth, and E.S. Orwoll, *Obesity and fracture in men and women: An epidemiologic perspective.* Journal of Bone and Mineral Research, 2012. **27**(1): p. 1-10.

256. Cole, Z.A., et al., *Increased fat mass is associated with increased bone size but reduced volumetric density in pre pubertal children.* Bone, 2012. **50**(2): p. 562-567.

257. Ingvorsen, C., N. Karp, and C. Lelliott, *The role of sex and body weight on the metabolic effects of high-fat diet in C57BL/6N mice.* Nutrition & Diabetes, 2017. **7**(4): p. e261.

258. Leibson, C.L., et al., *A Bone Structural Basis for Fracture Risk in Diabetes.* The Journal of Clinical Endocrinology & Metabolism, 2008. **93**(12): p. 4804-4809.

259. Heaney, R.P., et al., *Peak Bone Mass.* Osteoporosis International, 2000. **11**(12): p. 985-1009.

260. Bolotin, H.H., *DXA in vivo BMD methodology: An erroneous and misleading research and clinical gauge of bone mineral status, bone fragility, and bone remodelling.* Bone, 2007. **41**(1): p. 138-154.

261. Lundeen, G.A., et al., *The Contribution of Cortical and Cancellous Bone to Dual-Energy X-ray Absorptiometry Measurements in the Female Proximal Femur.* Osteoporosis International, 2001. **12**(3): p. 192-198.

262. Bergot, C., et al., *The degree and distribution of cortical bone mineralization in the human femoral shaft change with age and sex in a microradiographic study.* Bone, 2009. **45**(3): p. 435-442.

263. Ciarelli, T., et al., *Variations in three-dimensional cancellous bone architecture of the proximal femur in female hip fractures and in controls.* Journal of Bone and Mineral Research, 2000. **15**(1): p. 32-40.

264. Rollo, J., et al., *Assessment of trabecular bones microarchitectures and crystal structure of hydroxyapatite in bone osteoporosis with application of the Rietveld method.* Procedia Engineering, 2015. **110**: p. 8-14.

265. Phillips, K., *The Relationship of Sex, Age, and Physical Activity to Bone Maintenance and Loss: Implications for Bioarchaeological Research*, in *College of Arts and Social Sciences*. 2018, ANU: Canberra. p. 167.

266. Shahtaheri, S.M., et al., *Changes in trabecular bone architecture in women during pregnancy.* BJOG: An International Journal of Obstetrics & Gynaecology, 1999. **106**(5): p. 432-438.

267. Andrade, V.F.C., et al., *Bone Histomorphometry in Young Patients With Type 2 Diabetes is Affected by Disease Control and Chronic Complications.* The Journal of Clinical Endocrinology & Metabolism, 2019. **105**(2): p. 506-514.

268. Kanis, J.A., et al., *Interpretation and use of FRAX in clinical practice.* Osteoporosis International, 2011. **22**(9): p. 2395.

269. Poiana, C. and C. Capatina, *Fracture Risk Assessment in Patients With Diabetes Mellitus.* Journal of Clinical Densitometry, 2017. **20**(3): p. 432-443.

270. Valentini, A., et al., *FRAX tool in type 2 diabetic subjects: the use of HbA1c in estimating fracture risk.* Acta Diabetologica, 2018. **55**(10): p. 1043-1050.

271. Leslie, W.D., et al., *Comparison of Methods for Improving Fracture Risk Assessment in Diabetes: The Manitoba BMD Registry.* Journal of Bone and Mineral Research, 2018. **33**(11): p. 1923-1930.

272. Leib, E., et al., *Vertebral microarchitecture and fragility fracture in men: a TBS study.* Bone, 2014. **62**: p. 51-5.

273. Boutroy, S., et al., *Trabecular bone score improves fracture risk prediction in non-osteoporotic women: the OFELY study.* Osteoporosis International, 2013. **24**(1): p. 77-85.

274. Kim, J.H., et al., *Trabecular Bone Score as an Indicator for Skeletal Deterioration in Diabetes.* The Journal of Clinical Endocrinology & Metabolism, 2015. **100**(2): p. 475-482.

275. Leslie, W.D., et al., *TBS (trabecular bone score) and diabetes-related fracture risk.* Journal of Clinical Endocrinology & Metabolism, 2013. **98**(2): p. 602-9.

276. Kim, K., et al. *Difference in trabecular bone score according to spine-femur bone mineral density discordances in healthy postmenopausal women*. in *21st European Congress of Endocrinology*. 2019. BioScientifica.

277. White, R., et al., *An Exploratory Study of the Texture Research Investigational Platform (TRIP) to Evaluate Bone Texture Score of Distal Femur DXA Scans - A TBS-Based Approach.* Journal of Clinical Densitometry, 2019.

278. John, W.G. and E.J. Lamb, *The maillard or browning reaction in diabetes.* Eye, 1993. **7**(2): p. 230-237.

279. Brennan, M., *Changes in solubility, non-enzymatic glycation, and fluorescence of collagen in tail tendons from diabetic rats.* Journal of Biological Chemistry, 1989. **264**(35): p. 20947-52.

280. Andreassen, T.T., K. Seyer-Hansen, and A.J. Bailey, *Thermal stability, mechanical properties and reducible cross-links of rat tail tendon in experimental diabetes.* Biochimica et Biophysica Acta, 1981. **677**(2): p. 313-7.

281. Avery, N.C. and A.J. Bailey, *The effects of the Maillard reaction on the physical properties and cell interactions of collagen.* Pathologie Biologie, 2006. **54**(7): p. 387-95.

282. Hunt, H.B., et al., *Bone Tissue Collagen Maturity and Mineral Content Increase With Sustained Hyperglycemia in the KK-Ay Murine Model of Type 2 Diabetes.* Journal of Bone and Mineral Research, 2018. **33**(5): p. 921-929.

283. Wang, S.X., et al., *A crosslinked cofactor in lysyl oxidase: Redox function for amino acid side chains.* Science, 1996. **273**(5278): p. 1078.

284. Nyman, J.S. and A.J. Makowski, *The Contribution of the Extracellular Matrix to the Fracture Resistance of Bone.* Current Osteoporosis Reports, 2012. **10**(2): p. 169-177.

285. Saito, M., K. Fujii, and K. Marumo, *Degree of Mineralization-related Collagen Crosslinking in the Femoral Neck Cancellous Bone in Cases of Hip Fracture and Controls.* Calcified Tissue International, 2006. **79**(3): p. 160-168.

286. Burstein, A.H., et al., *Contribution of collagen and mineral to the elastic-plastic properties of bone.* Journal of Bone and Joint Surgery (American volume), 1975. **57**(7): p. 956-61.

287. Miranda, C., et al., *Influence of high glucose and advanced glycation end-products (ages) levels in human osteoblast-like cells gene expression.* BMC Musculoskeletal Disorders, 2016. **17**(1): p. 377.

288. Thomas, C.J., et al., *Accumulation of carboxymethyl-lysine (CML) in human cortical bone.* Bone, 2018. **110**: p. 128-133.

289. Fu, M.X., et al., *The advanced glycation end product, Nepsilon-(carboxymethyl)lysine, is a product of both lipid peroxidation and glycoxidation reactions.* Journal of Biological Chemistry, 1996. **271**(17): p. 9982-6.

290. Barzilay, J.I., et al., *Circulating levels of carboxy-methyl-lysine (CML) are associated with hip fracture risk: the Cardiovascular Health Study.* Journal of Bone and Mineral Research, 2014. **29**(5): p. 1061-6.

291. Reddy, S., et al., *N epsilon-(carboxymethyl)lysine is a dominant advanced glycation end product (AGE) antigen in tissue proteins.* Biochemistry, 1995. **34**(34): p. 10872-8.

292. Snelson, M. and M.T. Coughlan, *Dietary Advanced Glycation End Products: Digestion, Metabolism and Modulation of Gut Microbial Ecology.* Nutrients, 2019. **11**(2).

293. Sayej, W.N., et al., *Advanced Glycation End Products Induce Obesity and Hepatosteatosis in CD-1 Wild-Type Mice.* BioMed Research International, 2016. **2016**: p. 7867852.

294. Eckhardt, B.A., et al., *Accelerated osteocyte senescence and skeletal fragility in mice with type 2 diabetes.* JCI Insight, 2020. **5**(9).

295. Tanaka, H., et al., *Characteristics of bone strength and metabolism in type 2 diabetic model Tsumura, Suzuki, Obese Diabetes mice.* Bone Reports, 2018. **9**: p. 74-83.

296. ODETTI, P., et al., *Advanced Glycation End Products and Bone Loss during Aging.* Annals of the New York Academy of Sciences, 2005. **1043**(1): p. 710-717.

297. Karim, L., et al., *Differences in non-enzymatic glycation and collagen cross-links between human cortical and cancellous bone.* Osteoporosis International, 2013. **24**(9): p. 2441-2447.

298. Bornstein, P. and K.A. Piez, *The Nature of the Intramolecular Cross-Links in Collagen. The Separation and Characterization of Peptides from the Cross-Link Region of Rat Skin Collagen.* Biochemistry, 1966. **5**(11): p. 3460-3473.

299. Selye, H., *Lathyrism.* Revue Canadienne de Biologie, 1957. **16**(1): p. 1-82.

300. Gerstenfeld, L.C., et al., *Post-translational control of collagen fibrillogenesis in mineralizing cultures of chick osteoblasts.* Journal of Bone and Mineral Research, 1993. **8**(9): p. 1031-1043.

301. Atsawasuwan, P., et al., *Lysyl oxidase binds transforming growth factor-beta and regulates its signaling via amine oxidase activity.* Journal of Biological Chemistry, 2008. **283**(49): p. 34229-34240.

302. Pischon, N., et al., *Lysyl oxidase (lox) gene deficiency affects osteoblastic phenotype.* Calcified Tissue International, 2009. **85**(2): p. 119-126.

303. Pastel, E., et al., *Lysyl oxidase and adipose tissue dysfunction.* Metabolism, 2018. **78**: p. 118-127.

304. Khosravi, R., et al., *Collagen advanced glycation inhibits its Discoidin Domain Receptor 2 (DDR2)-mediated induction of lysyl oxidase in osteoblasts.* Bone, 2014. **58**: p. 33-41.

305. Bornstein, P., *The cross-linking of collagen and elastin and its inhibition in osteolathyrism. Is there a relation to the aging process?* American Journal of Medicine, 1970. **49**(4): p. 429-35.

306. Acevedo, C., et al., *Contributions of Material Properties and Structure to Increased Bone Fragility for a Given Bone Mass in the UCD-T2DM Rat Model of Type 2 Diabetes.* Journal of Bone and Mineral Research, 2018. **33**(6): p. 1066-1075.

307. Thaler, R., et al., *Homocysteine suppresses the expression of the collagen cross-linker lysyl oxidase involving IL-6, Fli1, and epigenetic DNA methylation.* Journal of Biological Chemistry, 2011. **286**(7): p. 5578-88.

308. Fujii, K., T. Kajiwara, and H. Kurosu, *Effect of vitamin B6 deficiency on the crosslink formation of collagen.* FEBS letters, 1979. **97**(1): p. 193-195.

309. Booth, A.A., et al., *In vitro kinetic studies of formation of antigenic advanced glycation end products (AGEs). Novel inhibition of post-Amadori glycation pathways.* Journal of Biological Chemistry, 1997. **272**(9): p. 5430-7.

310. Nakamura, S., et al., *Pyridoxal phosphate prevents progression of diabetic nephropathy.* Nephrology Dialysis Transplantation, 2007. **22**(8): p. 2165-74.

311. Merigliano, C., et al., *The Relationship Between Vitamin B6, Diabetes and Cancer.* Frontiers in Genetics, 2018. **9**: p. 388.

312. DeBey, H.J., E.E. Snell, and C.A. Baumann, *Studies on the Interrelationship between Methionine and Vitamin B6.* The Journal of Nutrition, 1952. **46**(2): p. 203-214.

313. Castano-Martinez, T., et al., *Methionine restriction prevents onset of type 2 diabetes in NZO mice.* FASEB Journal, 2019. **33**(6): p. 7092-7102.

314. Tessari, P., et al., *Effects of insulin on methionine and homocysteine kinetics in type 2 diabetes with nephropathy.* Diabetes, 2005. **54**(10): p. 2968-76.

315. Liu, G., K. Nellaiappan, and H.M. Kagan, *Irreversible inhibition of lysyl oxidase by homocysteine thiolactone and its selenium and oxygen analogues. Implications for homocystinuria.* Journal of Biological Chemistry, 1997. **272**(51): p. 32370-7.

316. Vijayan, V. and S. Gupta, *Role of osteocytes in mediating bone mineralization during hyperhomocysteinemia.* Journal of Endocrinology, 2017. **233**(3): p. 243-255.

317. Miyawaki, K., et al., *Glucose intolerance caused by a defect in the entero-insular axis: a study in gastric inhibitory polypeptide receptor knockout mice.* Proceedings of the National Academy of Sciences of the United States of America, 1999. **96**(26): p. 14843-7.

318. Bollag, R.J., et al., *Osteoblast-Derived Cells Express Functional Glucose-Dependent Insulinotropic Peptide Receptors.* Endocrinology, 2000. **141**(3): p. 1228-1235.

319. Pacheco-Pantoja, E.L., et al., *Receptors and effects of gut hormones in three osteoblastic cell lines.* BMC Physiology, 2011. **11**(1): p. 12.

320. Gaudin-Audrain, C., et al., *Glucose-dependent insulinotropic polypeptide receptor deficiency leads to modifications of trabecular bone volume and quality in mice.* Bone, 2013. **53**(1): p. 221-30.

321. Vilsbøll, T., et al., *Incretin secretion in relation to meal size and body weight in healthy subjects and people with type 1 and type 2 diabetes mellitus.* Journal of Clinical Endocrinology & Metabolism, 2003. **88**(6): p. 2706-13.

322. Nauck, M.A., et al., *Preserved incretin activity of glucagon-like peptide 1 [7-36 amide] but not of synthetic human gastric inhibitory polypeptide in patients with type-2 diabetes mellitus.* Journal of Clinical Investigation, 1993. **91**(1): p. 301-7.

323. Westberg-Rasmussen, S., et al., *Differential impact of glucose administered intravenously or orally on bone turnover markers in healthy male subjects.* Bone, 2017. **97**: p. 261-266.

324. Mieczkowska, A., et al., *Glucose-dependent insulinotropic polypeptide (GIP) directly affects collagen fibril diameter and collagen cross-linking in osteoblast cultures.* Bone, 2015. **74**: p. 29-36.

325. Daley, E.J., et al., *Impaired Gastric Hormone Regulation of Osteoblasts and Lysyl Oxidase Drives Bone Disease in Diabetes Mellitus.* JBMR Plus, 2019. **3**(10): p. e10212.

326. Ericksen, M.F., *Aging changes in the medullary cavity of the proximal femur in American Blacks and Whites.* American Journal of Physical Anthropology, 1979. **51**(4): p. 563-569.

327. Abrigo, J., et al., *High Fat Diet-Induced Skeletal Muscle Wasting Is Decreased by Mesenchymal Stem Cells Administration: Implications on Oxidative Stress, Ubiquitin Proteasome Pathway Activation, and Myonuclear Apoptosis.* Oxidative Medicine and Cellular Longevity, 2016. **2016**: p. 9047821.

328. Tencerova, M., et al., *Metabolic programming determines the lineage-differentiation fate of murine bone marrow stromal progenitor cells.* Bone Research, 2019. **7**(1): p. 35.

329. Brown, M.L., et al., *Delayed fracture healing and increased callus adiposity in a C57BL/6J Murine model of obesity-associated type 2 diabetes mellitus.* PLoS One, 2014. **9**(6): p. e99656.

330. Gutierrez, S., et al., *CCAAT/enhancer-binding proteins (C/EBP) beta and delta activate osteocalcin gene transcription and synergize with Runx2 at the C/EBP element to regulate bone-specific expression.* Journal of Biological Chemistry, 2002. **277**(2): p. 1316-23.

331. Pereira, R.C., A.M. Delany, and E. Canalis, *Effects of cortisol and bone morphogenetic protein-2 on stromal cell differentiation: correlation with CCAAT-enhancer binding protein expression.* Bone, 2002. **30**(5): p. 685-91.

332. Inzana, J.A., et al., *Immature mice are more susceptible to the detrimental effects of high fat diet on cancellous bone in the distal femur.* Bone, 2013. **57**(1): p. 174-83.

333. Doucette, C.R., et al., *A High Fat Diet Increases Bone Marrow Adipose Tissue (MAT) But Does Not Alter Trabecular or Cortical Bone Mass in C57BL/6J Mice.* Journal of Cellular Physiology, 2015. **230**(9): p. 2032-2037.

334. Cao, J.J., L. Sun, and H. Gao, *Diet-induced obesity alters bone remodeling leading to decreased femoral trabecular bone mass in mice.* Annals of the New York Academy of Sciences, 2010. **1192**(1): p. 292-297.

335. Patsch, J.M., et al., *Increased bone resorption and impaired bone microarchitecture in short-term and extended high-fat diet–induced obesity.* Metabolism, 2011. **60**(2): p. 243-249.

336. Devlin, M.J., et al., *Early-onset type 2 diabetes impairs skeletal acquisition in the male TALLYHO/JngJ mouse.* Endocrinology, 2014. **155**(10): p. 3806-16.

337. Semba, R.D., et al., *Fat mass is inversely associated with serum carboxymethyl-lysine, an advanced glycation end product, in adults.* Journal of Nutrition, 2011. **141**(9): p. 1726-30.

338. Strieder-Barboza, C., et al., *Advanced glycation end-products regulate extracellular matrix-adipocyte metabolic crosstalk in diabetes.* Scientific Reports, 2019. **9**(1): p. 19748.

339. Gaens, K.H.J., et al., *N-ε(Carboxymethyl)lysine-Receptor for Advanced Glycation End Product Axis Is a Key Modulator of Obesity-Induced Dysregulation of Adipokine Expression and Insulin Resistance.* Arteriosclerosis, Thrombosis, and Vascular Biology, 2014. **34**(6): p. 1199-1208.

340. Arsov, T., et al., *Fat Aussie—A New Alström Syndrome Mouse Showing a Critical Role for ALMS1 in Obesity, Diabetes, and Spermatogenesis.* Molecular Endocrinology, 2006. **20**(7): p. 1610-1622.

341. Sorokin, S., *Centrioles and the formation of rudimentary cilia by fibroblasts and smooth muscle cells.* Journal of Cell Biology, 1962. **15**: p. 363-77.

342. Marshall, J.D., et al., *Spectrum of ALMS1 variants and evaluation of genotype-phenotype correlations in Alstrom syndrome.* Human Mutation, 2007. **28**(11): p. 1114-23.

343. Hearn, T., et al., *Subcellular localization of ALMS1 supports involvement of centrosome and basal body dysfunction in the pathogenesis of obesity, insulin resistance, and type 2 diabetes.* Diabetes, 2005. **54**(5): p. 1581-7.

344. Alstrom, C.H., et al., *Retinal degeneration combined with obesity, diabetes mellitus and neurogenous deafness: a specific syndrome (not hitherto described) distinct from the Laurence-Moon-Bardet-Biedl syndrome: a clinical, endocrinological and genetic examination based on a large pedigree.* Acta Psychiatrica et Neurologica Scandinavica, Supplementum, 1959. **129**: p. 1-35.

345. Goldstein, J.L. and P.J. Fialkow, *Report of three cases with further delineation of the clinical, pathophysiological, and genetic aspects fo the disorder.* Medicine, 1973. **52**(1): p. 53.

346. Hearn, T., et al., *Mutation of ALMS1, a large gene with a tandem repeat encoding 47 amino acids, causes Alstrom syndrome.* Nature Genetics, 2002. **31**(1): p. 79-83.

347. Marshall, J.D., et al., *Alström syndrome: mutation spectrum of ALMS1.* Human Mutation, 2015. **36**(7): p. 660-668.

348. Han, J.C., et al., *Higher Leptin Concentrations in Patients With Alstrom Syndrome As Compared to BMI-Z Matched Controls Are Suggestive of Ciliopathy-Associated Leptin Resistance.* Obesity, 2011. **19**: p. S72-S72.

349. Heydet, D., et al., *A truncating mutation of Alms1 reduces the number of hypothalamic neuronal cilia in obese mice.* Developmental Neurobiology, 2013. **73**(1): p. 1-13.

350. Collin, G.B., et al., *Alms1-disrupted mice recapitulate human Alstrom syndrome.* Human Molecular Genetics, 2005. **14**(16): p. 2323-33.

351. Jaykumar, A.B., et al., *Role of Alstrom syndrome 1 in the regulation of blood pressure and renal function.* JCI Insight, 2018. **3**(21).

352. Tahani, N., et al., *Very high bone mineral density in a monogenic form of obesity-associated insulin resistance.* Bone, 2021. **143**: p. 115756.

353. Dagpo, T., *The role of adipose tissue in the pathogenesis of non-alcoholic steatohepatitis*, in *College of Health and Medicine*. 2015, ANU: Canberra. p. 216.

354. APF, A.P.F. *NOD.B10-Alms1foz/AnuApb*. 2014; Available from: https://pb.apf.edu.au/phenbank/strain.html?id=5386.

355. Yuan, R., et al., *Aging in inbred strains of mice: study design and interim report on median lifespans and circulating IGF1 levels.* Aging Cell, 2009. **8**(3): p. 277-87.

356. Montgomery, M.K., et al., *Mouse strain-dependent variation in obesity and glucose homeostasis in response to high-fat feeding.* Diabetologia, 2013. **56**(5): p. 1129-1139.

357. Picke, A.K., et al., *Update on the impact of type 2 diabetes mellitus on bone metabolism and material properties.* Endocrine Connections, 2019. **8**(3): p. R55-R70.

358. Osterhoff, G., et al., *Bone mechanical properties and changes with osteoporosis.* Injury, 2016. **47 Suppl 2**(Suppl 2): p. S11-S20.

359. Farrell, G.C., et al., *Strain dependence of diet-induced NASH and liver fibrosis in obese mice is linked to diabetes and inflammatory phenotype.* Liver International, 2014. **34**(7): p. 1084-1093.

360. Dooley, J., et al., *Genetic predisposition for beta cell fragility underlies type 1 and type 2 diabetes.* Nature Genetics, 2016. **48**(5): p. 519-527.

361. Brown, M.L., et al., *Delayed fracture healing and increased callus adiposity in a C57BL/6J murine model of obesity-associated type 2 diabetes mellitus.* PLoS One, 2014. **9**(6): p. e99656.

362. Campbell, G.M. and A. Sophocleous, *Quantitative analysis of bone and soft tissue by micro-computed tomography: applications to ex vivo and in vivo studies.* BoneKEy reports, 2014. **3**: p. 564-564.

363. Livak, K.J. and T.D. Schmittgen, *Analysis of relative gene expression data using real-time quantitative PCR and the 2(-Delta Delta C(T)) Method.* Methods, 2001. **25**(4): p. 402-8.

364. Price, C., et al., *Genetic variation in bone growth patterns defines adult mouse bone fragility.* Journal of Bone and Mineral Research, 2005. **20**(11): p. 1983-91.

365. Maynard, R.D. and C. Ackert-Bicknell, *Mouse models for functional analysis of osteoporosis genome wide association studies.* Frontiers in Endocrinology, 2019. **10**: p. 277.

366. Milanski, M., et al., *Saturated fatty acids produce an inflammatory response predominantly through the activation of TLR4 signaling in hypothalamus: implications for the pathogenesis of obesity.* Journal of Neuroscience, 2009. **29**(2): p. 359-70.

367. Zhang, X., et al., *Hypothalamic IKKbeta/NF-kappaB and ER stress link overnutrition to energy imbalance and obesity.* Cell, 2008. **135**(1): p. 61-73.

368. Jilka, R.L., *The relevance of mouse models for investigating age-related bone loss in humans.* Journals of Gerontology Series A: Biomedical Sciences and Medical Sciences, 2013. **68**(10): p. 1209-1217.

369. Poekes, L., et al., *Role of ciliary dysfunction in a new model of obesity and non-alcoholic steatohepatitis: the foz/foz mice.* Archives of Public Health, 2014. **72**(Suppl 1): p. O7-O7.

370. Favaretto, F., et al., *GLUT4 defects in adipose tissue are early signs of metabolic alterations in Alms1GT/GT, a mouse model for obesity and insulin resistance.* PLoS One, 2014. **9**(10): p. e109540.

371. Aslam, M.N., et al., *Bone structure and function in male C57BL/6 mice: Effects of a high-fat Western-style diet with or without trace minerals.* Bone Reports, 2016. **5**: p. 141-149.

372. Casazza, K., et al., *Diabetes-related impairment in bone strength is established early in the life course.* World Journal of Diabetes, 2013. **4**(4): p. 145-50.

373. Xiao, Z., et al., *Conditional deletion of Pkd1 in osteocytes disrupts skeletal mechanosensing in mice.* FASEB Journal, 2011. **25**(7): p. 2418-32.

374. Willinghamm, M.D., et al., *Age-related changes in bone structure and strength in female and male BALB/c mice.* Calcified Tissue International, 2010. **86**(6): p. 470-83.

375. Buie, H.R., C.P. Moore, and S.K. Boyd, *Postpubertal architectural developmental patterns differ between the L3 vertebra and proximal tibia in three inbred strains of mice.* Journal of Bone and Mineral Research, 2008. **23**(12): p. 2048-59.

376. Bloebaum, R.D., et al., *Age-Related mineralization heterogeneity changes in trabecular bone of the proximal femur.* The Anatomical Record Part A: Discoveries in Molecular, Cellular, and Evolutionary Biology, 2004. **281A**(2): p. 1296-1302.

377. Hemmatian, H., et al., *Age-related changes in female mouse cortical bone microporosity.* Bone, 2018. **113**: p. 1-8.

378. Bouxsein, M.L., et al., *Guidelines for assessment of bone microstructure in rodents using micro-computed tomography.* Journal of Bone and Mineral Research, 2010. **25**(7): p. 1468-86.

379. Feldkamp, L.A., L.C. Davis, and J.W. Kress, *Practical cone-beam algorithm.* Journal of the Optical Society of America A, 1984. **1**(6): p. 612-619.

380. Räth, C., et al., *Strength through structure: visualization and local assessment of the trabecular bone structure.* New Journal of Physics, 2008. **10**(12): p. 125010.

381. Parfitt, A.M., et al., *Relationships between surface, volume, and thickness of iliac trabecular bone in aging and in osteoporosis. Implications for the microanatomic and cellular mechanisms of bone loss.* The Journal of Clinical Investigation, 1983. **72**(4): p. 1396-1409.

382. Nordin, B.E., et al., *Bone formation and resorption as the determinants of trabecular bone volume in postmenopausal osteoporosis.* The Lancet, 1981. **2**(8241): p. 277-9.

383. Nishiyama, K.K., et al., *Postmenopausal women with osteopenia have higher cortical porosity and thinner cortices at the distal radius and tibia than women with normal aBMD: An in vivo HR-pQCT study.* Journal of Bone and Mineral Research, 2010. **25**(4): p. 882-890.

384. Patsch, J.M., et al., *Increased cortical porosity in type 2 diabetic postmenopausal women with fragility fractures.* Journal of Bone and Mineral Research, 2013. **28**(2): p. 313-324.

385. Bruker, *How to Generate Pore Size Distribution and Characterize Open Versus Closed Pore Networks*, in *Bruker Micro-CT Academy*. 2014: Belgium. p. 1-2.

386. Barak, M.M., D.E. Lieberman, and J.-J. Hublin, *Of mice, rats and men: Trabecular bone architecture in mammals scales to body mass with negative allometry.* Journal of Structural Biology, 2013. **183**(2): p. 123-131.

387. Miller, M.A., et al., *Intratrabecular tunneling increases trabecular number throughout the skeleton of ovariectomized rhesus monkeys treated with parathyroid hormone 1-84.* Bone, 2008. **42**(6): p. 1175-83.

388. Jerome, C.P., et al., *Treatment with human parathyroid hormone (1-34) for 18 months increases cancellous bone volume and improves trabecular architecture in ovariectomized cynomolgus monkeys (Macaca fascicularis).* Bone, 2001. **28**(2): p. 150-159.

389. Dempster, D.W., *The Contribution of Trabecular Architecture to Cancellous Bone Quality.* Journal of Bone and Mineral Research, 2000. **15**(1): p. 20-23.

390. Fox, J., et al., *Effects of Treatment of Ovariectomized Adult Rhesus Monkeys with Parathyroid Hormone 1-84 for 16 Months on Trabecular and Cortical Bone Structure and Biomechanical Properties of the Proximal Femur.* Calcified Tissue International, 2007. **81**(1): p. 53-63.

391. Burghardt, A.J., et al., *High-Resolution Peripheral Quantitative Computed Tomographic Imaging of Cortical and Trabecular Bone Microarchitecture in Patients with Type 2 Diabetes Mellitus.* The Journal of Clinical Endocrinology & Metabolism, 2010. **95**(11): p. 5045-5055.

392. Nyman, J.S., et al., *Increasing duration of type 1 diabetes perturbs the strength-structure relationship and increases brittleness of bone.* Bone, 2011. **48**(4): p. 733-40.

393. Rabelo, G.D., et al., *Multiscale bone quality analysis in osteoarthritic knee joints reveal a role of the mechanosensory osteocyte network in osteophytes.* Scientific Reports, 2020. **10**(1): p. 673.

394. Fu, C., et al., *High insulin levels in KK-Ay diabetic mice cause increased cortical bone mass and impaired trabecular micro-structure.* International Journal of Molecular Sciences, 2015. **16**(4): p. 8213-8226.

395. Kerckhofs, G., et al., *Changes in bone macro-and microstructure in diabetic obese mice revealed by high resolution microfocus X-ray computed tomography.* Scientific Reports, 2016. **6**(1): p. 35517.

396. Malvi, P., et al., *High fat diet promotes achievement of peak bone mass in young rats.* Biochemical and Biophysical Research Communications, 2014. **455**(1-2): p. 133-138.

397. Link, T.M., et al., *Imaging of trabecular bone structure in osteoporosis.* European Radiology, 1999. **9**(9): p. 1781-8.

398. Ionova-Martin, S.S., et al., *Reduced size-independent mechanical properties of cortical bone in high-fat diet-induced obesity.* Bone, 2010. **46**(1): p. 217-225.

399. Beamer, W.G., et al., *Genetic variability in adult bone density among inbred strains of mice.* Bone, 1996. **18**(5): p. 397-403.

400. Garrard, G., G.A. Harrison, and J.S. Weiner, *Genotypic differences in the ossification of 12 day old mice at 23 degrees C and 32 degrees C.* Journal of Anatomy, 1974. **117**(Pt 3): p. 531-9.

401. Lecka-Czernik, B., et al., *High bone mass in adult mice with diet-induced obesity results from a combination of initial increase in bone mass followed by attenuation in bone formation; implications for high bone mass and decreased bone quality in obesity.* Molecular and Cellular Endocrinology, 2015. **410**: p. 35-41.

402. Sheng, M.H.C., et al., *Regulation of bone volume is different in the metaphyses of the femur and vertebra of C3H/HeJ and C57BL/6J mice.* Bone, 2002. **30**(3): p. 486-491.

403. Rubin, M.A., J. Rubin, and I. Jasiuk, *SEM and TEM study of the hierarchical structure of C57BL/6J and C3H/HeJ mice trabecular bone.* Bone, 2004. **35**(1): p. 11-20.

404. Engvall, E. and P. Perlmann, *Enzyme-linked immunosorbent assay (ELISA) quantitative assay of immunoglobulin G.* Immunochemistry, 1971. **8**(9): p. 871-874.

405. Lazarus, J.E., et al., *Fibroblast growth factor expression in the postnatal growth plate.* Bone, 2007. **40**(3): p. 577-86.

406. Eswarakumar, V.P., et al., *A gain-of-function mutation of Fgfr2c demonstrates the roles of this receptor variant in osteogenesis.* Proceedings of the National Academy of Sciences of the United States of America, 2004. **101**(34): p. 12555.

407. Triplett, J.W., et al., *Mechanical Loading by Fluid Shear Stress Enhances IGF-1 Receptor Signaling in Osteoblasts in A PKC ζ-Dependent Manner.* Molecular & Cellular Biomechanics, 2007. **4**(1): p. 13.

408. Sakata, T., et al., *Skeletal Unloading Induces Resistance to Insulin-Like Growth Factor-I (IGF-I) by Inhibiting Activation of the IGF-I Signaling Pathways.* Journal of Bone and Mineral Research, 2004. **19**(3): p. 436-446.

409. Wang, Y., et al., *IGF-I receptor is required for the anabolic actions of parathyroid hormone on bone.* Journal of Bone and Mineral Research, 2007. **22**(9): p. 1329-37.

410. Kostenuik, P.J., et al., *Skeletal Unloading Causes Resistance of Osteoprogenitor Cells to Parathyroid Hormone and to Insulin-like Growth Factor-I.* Journal of Bone and Mineral Research, 1999. **14**(1): p. 21-31.

411. Zhang, M., et al., *Osteoblast-specific knockout of the insulin-like growth factor (IGF) receptor gene reveals an essential role of IGF signaling in bone matrix mineralization.* Journal of Biological Chemistry, 2002. **277**(46): p. 44005-12.

412. Alos, N. and B. Ecarot, *Downregulation of osteoblast Phex expression by PTH.* Bone, 2005. **37**(4): p. 589-98.

413. Zoidis, E., et al., *IGF-I and GH stimulate Phex mRNA expression in lungs and bones and 1,25-dihydroxyvitamin D(3) production in hypophysectomized rats.* European Journal of Endocrinology 2002. **146**(1): p. 97-105.

414. Snelling, S.J., P.A. Hulley, and J. Loughlin, *BMP5 activates multiple signaling pathways and promotes chondrogenic differentiation in the ATDC5 growth plate model.* Growth Factors, 2010. **28**(4): p. 268-79.

415. Feldman, G.J., et al., *Over-expression of BMP4 and BMP5 in a child with axial skeletal malformations and heterotopic ossification: a new syndrome.* American Journal of Medical Genetics Part A, 2007. **143a**(7): p. 699-706.

416. Mader, R. and I. Lavi, *Diabetes mellitus and hypertension as risk factors for early diffuse idiopathic skeletal hyperostosis (DISH).* Osteoarthritis and Cartilage, 2009. **17**(6): p. 825-8.

417. Ho, A.M., et al., *Dominant negative Bmp5 mutation reveals key role of BMPs in skeletal response to mechanical stimulation.* BMC Developmental Biology, 2008. **8**: p. 35.

418. Resnick, D., R.J. Linovitz, and M.L. Feingold, *Postoperative heterotopic ossification in patients with ankylosing hyperostosis on the spine (Forestier's disease).* The Journal of Rheumatology, 1976. **3**(3): p. 313-320.

419. Wu, X., et al., *High-fat and high-glucose microenvironment decreases Runx2 and TAZ expression and inhibits bone regeneration in the mouse.* Journal of Orthopaedic Surgery and Research, 2019. **14**(1): p. 55.

420. Enomoto, H., et al., *Runx2 deficiency in chondrocytes causes adipogenic changes in vitro.* Journal of Cell Science, 2004. **117**(Pt 3): p. 417-25.

421. Tsuji, K., T. Komori, and M. Noda, *Aged Mice Require Full Transcription Factor, Runx2/Cbfa1, Gene Dosage for Cancellous Bone Regeneration After Bone Marrow Ablation.* journal of Bone and Mineral Research, 2004. **19**(9): p. 1481-1489.

422. Di Cesare, P., et al., *Cartilage oligomeric matrix protein (COMP) is an abundant component of tendon.* FEBS Letters, 1994. **354**(2): p. 237-240.

423. Di Cesare, P.E., et al., *Expression of cartilage oligomeric matrix protein (COMP) by embryonic and adult osteoblasts.* Journal of Orthopaedic Research, 2000. **18**(5): p. 713-720.

424. Coustry, F., et al., *Mutant cartilage oligomeric matrix protein (COMP) compromises bone integrity, joint function and the balance between adipogenesis and osteogenesis.* Matrix Biology, 2018. **67**: p. 75-89.

425. Kelpke, S.S., et al., *Acidic fibroblast growth factor signaling inhibits peroxynitrite-induced death of osteoblasts and osteoblast precursors.* Journal of Bone and Mineral Research, 2001. **16**(10): p. 1917-25.

426. Dunstan, C.R., et al., *Systemic administration of acidic fibroblast growth factor (FGF-1) prevents bone loss and increases new bone formation in ovariectomized rats.* Journal of Bone and Mineral Research, 1999. **14**(6): p. 953-9.

427. Cuevas, P., et al., *Hypotensive activity of fibroblast growth factor.* Science, 1991. **254**(5035): p. 1208-10.

428. Prudovsky, I., et al., *Secretion without Golgi.* Journal of Cellular Biochemistry, 2008. **103**(5): p. 1327-43.

429. Genge, B.R., L.N. Wu, and R.E. Wuthier, *Kinetic analysis of mineral formation during in vitro modeling of matrix vesicle mineralization: effect of annexin A5, phosphatidylserine, and type II collagen.* Analytical Biochemistry, 2007. **367**(2): p. 159-66.

430. Jonker, J.W., et al., *A PPARgamma-FGF1 axis is required for adaptive adipose remodelling and metabolic homeostasis.* Nature, 2012. **485**(7398): p. 391-4.

431. Gasser, E., et al., *FGF1 - a new weapon to control type 2 diabetes mellitus.* Nature Reviews Endocrinology, 2017. **13**(10): p. 599-609.

432. Wang, S., et al., *Fibroblast growth factor 1 levels are elevated in newly diagnosed type 2 diabetes compared to normal glucose tolerance controls.* Endocrine Journal, 2016. **63**(4): p. 359-65.

433. Wang, A., et al., *Characterization of fibroblast growth factor 1 in obese children and adolescents.* Endocrine Connections, 2018. **7**(8): p. 932-940.

434. Choi, Y., et al., *Increased expression of FGF1-mediated signaling molecules in adipose tissue of obese mice.* Journal of Physiology and Biochemistry, 2016. **72**(2): p. 157-167.

435. Liang, G., et al., *Fibroblast growth factor 1 ameliorates diabetic nephropathy by an anti-inflammatory mechanism.* Kidney International, 2018. **93**(1): p. 95-109.

436. Antal, M.C., et al., *Adenylate Cyclase Type III Is Not a Ubiquitous Marker for All Primary Cilia during Development.* PLoS One, 2017. **12**(1): p. e0170756.

437. Tong, T., et al., *Adenylyl cyclase 3 haploinsufficiency confers susceptibility to diet-induced obesity and insulin resistance in mice.* Scientific Reports, 2016. **6**(1): p. 34179.

438. Dalbay, M.T., et al., *Adipogenic Differentiation of hMSCs is Mediated by Recruitment of IGF-1r Onto the Primary Cilium Associated With Cilia Elongation.* Stem Cells, 2015. **33**(6): p. 1952-1961.

439. Mashayekhi, F., et al., *Increased acidic fibroblast growth factor concentrations in the serum and cerebrospinal fluid of patients with Alzheimer's disease.* Journal of Clinical Neuroscience, 2010. **17**(3): p. 357-359.

440. Mejhert, N., et al., *Mapping of the Fibroblast Growth Factors in Human White Adipose Tissue.* The Journal of Clinical Endocrinology & Metabolism, 2010. **95**(5): p. 2451-2457.

441. Bradley, J.C., et al., *Serum growth factor analysis in dry eye syndrome.* Clinical & Experimental Ophthalmology, 2008. **36**(8): p. 717-720.

442. Papageorgiou, M., et al., *Age- and Strain-Related Differences in Bone Microstructure and Body Composition During Development in Inbred Male Mouse Strains.* Calcified Tissue International, 2020. **106**(4): p. 431-443.

443. Halloran, B.P., et al., *Changes in bone structure and mass with advancing age in the male C57BL/6J mouse.* journal of Bone and Mineral Research, 2002. **17**(6): p. 1044-50.

444. Al-Amer, O., *Bone marker gene expression in calvarial bones: different bone microenvironments.* Journal of Biological Research-Thessaloniki, 2017. **24**: p. 8.

445. Farnsworth, C.W., et al., *Obesity/type 2 diabetes increases inflammation, periosteal reactive bone formation, and osteolysis during Staphylococcus aureus implant-associated bone infection.* Journal of Orthopaedic Research, 2018. **36**(6): p. 1614-1623.

446. Napoli, N., et al., *Bone Turnover Markers Do Not Predict Fracture Risk in Type 2 Diabetes.* Journal of Bone and Mineral Research, 2020. **35**(12): p. 2363-2371.

447. Holloway-Kew, K.L., et al., *Bone Turnover Markers in Men and Women with Impaired Fasting Glucose and Diabetes.* Calcified Tissue International, 2019. **104**(6): p. 599-604.